Inaugural Dissertation zur Erlangung des
Doktorgrades der Naturwissenschaften
der Justus-Liebig-Universität Gießen
(Fachbereich Physik)

Experiments on multi-nucleon transfer reactions with the systems ^{58,64}Ni + ^{207}Pb at SHIP

vorgelegt von
Victor Fernandovich Comas Lijachev
geboren in Moskau (Russland)

2012, Gießen

Gutachter: Prof Dr. Hans Geissel
Prof Dr. Volker Metag

Acknowledgements

I would like to specially thank Dr. Sophia Heinz for all the fruitful discussions and effort during the PhD work.

The special gratitude to Prof. Sigurd Hofmann for all his support from the very beginning, and for the opportunity offered to work at GSI. Thanks for all the valuable consultations and help.

I would like to thank all the SHIP group members for the time spent in consultations.

My special gratitude to Prof. Dr. Hans Geissel for accepting to be my supervisor in the university of Giessen.

Special thanks to Prof. Dr. Christoph Sheidenberger for accepting me as a PhD student in the university of Giessen.

I am very grateful to Dr. Fernando Guzman and Dr. Oscar Rodriguez for all their support from the Cuban side to be able to study in Germany.

I want to thank to all my friends at GSI, specially Julio Heredia, for all his help since we departed together from Cuba.

Finally, I would like to thank my spouse Sandra Leon, my son Alejandro and my family in Cuba, for all their support and patience.

Contents

Zusammenfassung

Seit einigen Jahren werden tiefinelastische Transferreaktionen häufig als Möglichkeit diskutiert, neue neutronenreiche Isotope von schweren und superschweren Kernen zu produzieren, die in anderen Reaktionen nicht zugänglich sind. Diese Diskussion wurde besonders durch eine Reihe von neuen theoretischen Arbeiten initiiert, während es neuere experimentelle Daten dazu nicht gibt. Von besonderem Interesse sind dabei superschwere Kerne mit Z $>$ 100 und Kerne im Bereich der abgeschlossenen Neutronenschale N=126. Die erwarteten Wirkungsquerschnitte sind klein und erreichen typischerweise Werte unterhalb 10^{-9} barn. Deshalb sind für entsprechende Experimente effiziente Separationsmethoden erforderlich sowie ein Detektorsystem, welches den Nachweis und die Identifizierung einzelner Kerne erlaubt. Dedizierte Experimentaufbauten für sehr schwere Transferprodukte gibt es gegenwärtig nicht. Aber die Separations- und Nachweistechniken, welche für superschwere Fusionsprodukte verwendet werden, sind entsprechend empfindlich und erlauben prinzipiell auch das Studium von schweren Transferprodukten. Insbesondere die Separation nach Geschwindigkeiten führt zu einer sehr guten Trennung der verschiedenen Transferprodukte, welche etwa fünf Mal stärker ist, als die Trennung nach magnetischer Steifigkeit.

Der "Separator for Heavy Ion Reaction Products" (SHIP) bei GSI ist zurzeit das einzige Geschwindigkeitsfilter für die Synthese der schwersten Kerne, während alle anderen Experimente gasgefüllte Separatoren verwenden. SHIP hat einen Akzeptanzwinkel von (0 $\pm$ 2) Grad und erlaubt somit den Nachweis von Kernen, die in Vorwärtsrichtung emittiert werden. Bei den typischerweise verwendeten Stoßsystemen aus mittelschweren Projektilen und sehr schweren Targetkernen und Energien an der Coulombbarriere fallen zwischen 1% und 5% der targetähnlichen Transferprodukte in die Winkelakzeptanz von SHIP. Die Geschwindigkeiten dieser Transferprodukte sind etwa 1.7 bis 2-mal höher als die Geschwindigkeit der erwarteten Fusionsprodukte, abhängig vom Verlust an kinetischer Energie während der Reaktion. Durch schrittweise Variation der elektrischen und magnetischen Felder von SHIP können die

Geschwindigkeitsspektren der Reaktionsprodukte aufgenommen werden. Aus der Lage der Maxima in den Spektren kann der Reaktionskanal (Fusion, verschiedene Transferkanäle, etc.) zugeordnet werden. Die Identifizierung der erzeugten Isotope erfolgt durch deren radioaktive Zerfälle, insbesondere der Alphazerfälle, die in einem Implantationsdetektor am Ende des Separators nachgewiesen werden. Bei SHIP wird nur das targetähnliche Transferprodukt detektiert. Die Rekonstruktion der gesamten Kinematik und die Bestimmung des Verlustes an kinetischer Energie erfolgt über die ermittelte Geschwindigkeit des targetähnlichen Kerns unter Annahme einer binären Reaktion. Bei einem totalen Wirkungsquerschnitt von 10^{-9} barn für ein bestimmtes Transferprodukt können an SHIP ca. 10 Kerne pro Tag nachgewiesen werden.

In der vorliegenden Arbeit wurden tiefinelastische Transferreaktionen in den Systemen ^{64}Ni + ^{207}Pb und ^{58}Ni + ^{207}Pb bei Energien von 10% unterhalb bis ca. 20% oberhalb der Coulombbarriere untersucht. Die Verwendung von Blei als Targetmaterial führt zur Bevölkerung einer großen Region von Alphaemittern oberhalb des Targetkerns, was die eindeutige Identifizierung der Kerne über deren Alphazerfälle erlaubt. Außerdem sind die Transferwirkungsquerschnitte in diesem Bereich relativ hoch. Das erlaubt, die oben beschriebene Methode für Separation und Nachweis, sowie die Charakteristiken dieser Transferreaktionen mit guter Statistik zu studieren. Die wichtigsten Ergebnisse dieser Arbeit sind im Folgenden zusammen gefasst.

- Mit beiden Projektil-Target Kombinationen wurde ein großer Bereich an Alphaemittern mit $83 \leq Z \leq 89$ populiert, was einem Transfer von bis zu 7 Protonen vom Projektil zum Targetkern entspricht. Kerne mit $Z < 83$ konnten nicht identifiziert werden, weil sie keine Alphaemitter und/oder zu langlebig sind. Für Kerne mit $Z > 88$ wurde ein steiler Abfall im Wirkungsquerschnitt beobachtet. Mit ^{58}Ni wurden bei allen Strahlenergien etwa zehn Mal größere Wirkungsquerschnitte gemessen, aber die neutronenreichsten Isotope, mit bis zu 8 Neutronen mehr als der Targetkern, wurden in Reaktionen mit ^{64}Ni beobachtet.

- Alle Transferprodukte, mit Ausnahme von Polonium und Astat Isotopen aus ^{58}Ni Reaktionen, stammen aus tief inelastischen Reaktionen (Quasispaltung), wobei abhängig von der Strahlenergie ein Verlust an kinetischer Energie von 70 - 140 MeV beobachtet wurde. Die totale kinetische Energie im Ausgangskanal ist unabhängig von der Strahlenergie und entspricht der Energie, die man auch für die Spaltung eines Compoundkerns erwarten würde. Die Reaktionsprodukte trennen sich mit einer Energie, die deren Coulombbarriere entspricht, wobei die Kerne stark deformiert sind mit Qudrupoldeformationen von $\beta_2 \approx 0.4$.

- Die nachgewiesenen Transferprodukte sind Sekundärprodukte, die aus den direkt im Stoß erzeugten und noch angeregten Isotopen (Primärprodukte) nach Emission von hauptsächlich Neutronen entstehen. Ein starker Verlust an Primärprodukten resultiert aus deren Spaltung aus dem angeregten Zustand. Die Spaltwahrscheinlichkeit steigt mit der Protonenzahl der Transferprodukte, bedingt durch die abnehmenden Spaltbarrieren. Die größten Wirkungsquerschnitte für die neutronenreichsten Transferprodukte wurden bei Strahlenergien nahe der Coulombbarriere gemessen. Mit steigender Strahlenergie bzw. Anregungsenergie steigt die Spaltwahrscheinlichkeit der Primärprodukte bzw. die Zahl der abgedampften Neutronen.

- Die Verteilung der primären Transferprodukte kann in guter Näherung aus den Q-Werten der Transferreaktionen rekonstruiert werden, wobei die Q-Werte aus den Massen von Projektil und Targetkern sowie den Massen aus projektilähnlichem und targetähnlichem Transferprodukt berechnet werden. Bei fester Protonenzahl werden bevorzugt diejenigen Primärprodukte gebildet, für die der Q-Wert ein Maximum annimmt. Durch einen Vergleich der Neutronenzahlen von erwarteten Primärprodukten mit den gemessenen Isotopen kann man die mittlere Anzahl der abgedampften Neutronen und damit die Anregungsenergie der Primärprodukte bestimmen. Dabei zeigte sich, dass die Reaktionen mit ^{58}Ni zu deutlich kleineren Anregungsenergien der targetähnlichen Transferprodukte, von 10 MeV oder weniger führen, welche nahezu unabhängig von Isotop und Strahlenergie sind. Bei Reaktionen mit ^{64}Ni wurden Anregungsenergien von 10 - 50 MeV beobachtet, die eine deutliche Abhängigkeit von Isotop und Strahlenergie zeigen. Die Ergebnisse lassen sich interpretieren, wenn man den Einfluss von Schaleneffekten, insbesondere der N=126 Schale, auf den Verlauf der Transferreaktion berücksichtigt.

- Ein Vergleich der gemessenen Wirkungsquerschnitte mit Rechnungen im Zwei-Zentren Schalenmodell zeigt, dass die Wirkungsquerschnitte für die Transferprodukte von der Theorie um mindestens eine Größenordung unterschätzt werden.

- Ein Vergleich der Anregungsfunktionen für die Transferprodukte und für superschwere Fusionsprodukte aus Ni + Pb Reaktionen lässt auf eine nahe Verwandtschaft der beiden Reaktionen schließen. Die experimentellen Daten geben einen deutlichen Hinweis auf die Gültigkeit des Zwei-Zentren-Schalenmodells zur Beschreibung des Fusionsprozesses.

- Die Geschwindigkeitsspektren der meisten Transferprodukte zeigen zwei Maxima, was ein deutlicher Hinweis für die Existenz von relativ langlebigen Kernmolekülen

ist, die eine Rotation von mindestens 180 Grad durchlaufen, bevor sie aufbrechen. Der Austausch von Nukleonen findet während Lebensdauer des Kernmoleküls statt. Aus den gemessenen Intensitäten der beiden Maxima können die mittleren Lebensdauern der Kernmoleküle abgeschätzt werden. Aus den vorliegenden Daten wurden mittlere Lebensdauern um 10^{-20} s für das System Ni+Pb ermittelt. Die Lebensdauern zeigen eine systematische Abhängigkeit von der Protonenzahl der Transferprodukte und steigen mit zunehmender Zahl an transferierten Protonen bzw. Nukleonen.

Introduction

The expansion of the nuclear chart towards neutron rich and neutron deficient isotopes has been one of the major challenges in nuclear physics since its beginnings. In the light and medium heavy regions the quest has been mainly directed to reach exotic nuclei close to the neutron and proton drip-lines. These isotopes have been mainly produced using fragmentation reactions and through the fission of heavy nuclei.

For heavier nuclei, particularly superheavy nuclei with Z>100, the isotopes are usually produced in fusion-evaporation reactions. Superheavy nuclei have been of special interest for the nuclear physicists in the last 50 years where fundamental questions arose concerning the existence of an "island of stability". The location of the next closed shells has been differently predicted by theoretical models. In the work of Strutinsky and Smolanczuk [1, 2], Z=114 and N=184 were predicted to be the next closed shells while Hartree-Fock calculations predicted Z=126 and N=184.

Fusion reactions using stable isotopes produce mainly neutron deficient nuclei. In order to extend the present limits of the nuclear chart towards neutron rich heavy isotopes new reactions must be considered. One possibility which has been revitalized nowadays is the use of multi-nucleon transfer reactions. Several new theoretical studies have been done in the last years considering the production of new superheavy nuclei using multi-nucleon transfer reactions with a combination of heavy projectile plus heavy target nucleus [3] and medium heavy projectile plus heavy target nuclei [4].

Also neutron-rich nuclei in the vicinity of the closed shell N=126 have been predicted to be produced in multi-nucleon transfer reactions [5, 6] with larger yields than those expected in the usually applied fragmentation reactions. The N=126 region is of special interest for astrophysics, in particular for the production of heavy elements in stellar nucleosynthesis in the r-process. The possible last waiting point is expected at this closed shell. From the structure point of view it can contribute to the present discussion of the quenching of the nuclear shells for neutron-rich nuclei.

In general, the expected cross-sections for the production of new neutron rich heavy and superheavy nuclei are rather small (nanobarn to picobarn) like in the cases of fusion and fragmentation reactions. Therefore, efficient separation techniques are necessary before the detection of the reaction products. Also precise identification of the charge and neutron numbers of the reaction products is needed. An appropriate experimental setup to study such reactions does not exist presently. But already existing facilities for the synthesis of heavy elements in fusion reactions can also be used for the investigation of transfer reactions. The velocity filter SHIP offers the possibility to separate heavy target-like transfer products from projectiles and projectile-like reaction products before they reach the detection system where the identification is done through their decay characteristics. At SHIP a cross-section limit of 10 pb per day can be reached at usual beam intensities of 5×10^{12} particles per second.

The study of transfer reactions in heavy systems contributes to two main directions: (i) to investigate the optimum parameters for the production of neutron rich isotopes; (ii) to improve the knowledge about the first steps of fusion reactions which are reflected by the characteristics of the transfer products close to the target nucleus. In the present thesis work the reactions ^{58,64}Ni + ^{207}Pb were selected to populate a region of known α-emitters above the target nucleus with relatively high cross-sections. The well known α-decay characteristics of the produced isotopes facilitate their identification. The influence of the projectile neutron number on the cross-sections, isotopic distributions and excitation energies of the transfer products was studied. The experimental results can contribute considerably to the existing theoretical models for a better understanding of the reaction process itself.

Chapter 1

Deep Inelastic Reactions

Nuclear reactions involving light projectiles with medium and heavy targets can be generally divided into two groups; direct reactions and compound nucleus (CN) reactions. The classification is done according to the distribution of the reaction products in energy, mass, charge and angle. These two processes can also be distinguished from their time scales. Direct reactions are considered fast processes ($\sim 10^{-22}$ s) comparable to the transit of a nucleon with Fermi momentum through the nuclear diameter. Compound nucleus reactions are slow processes ($\sim 10^{-16}$ s - 10^{-19} s) where an intermediate system is formed which lives long enough to reach complete equilibrium. Its decay is independent of the properties of the entrance channel and only depends on the conserved quantities like total energy, angular momentum and mass.

In case of reactions involving more complex nuclei, heavier projectiles and heavy targets, more complex mechanisms start to appear. These mechanisms are related to the formation of an intermediate system called by Volkov et al., di-nuclear system (DNS) [7], by Plasil et al., composite system [8] and intermediate complex by Moretto et al. [9], which lives 10^{-21}s - 10^{-20}s. This time is only enough to reach partial equilibrium in the system. In the following the term DNS will be used to refer to this system which is the more used nowadays.

The DNS formation is a result of the high viscosity and low compressibility of the nuclear matter which leads to intense kinetic energy dissipation that is mainly transformed into excitation energy of the system. The low compressibility prevents the penetration of the nuclei into each other and a dumbbell-like system is formed. Within this strong overlap of the outer shells, nucleons and energy are interchanged and at the same time the nuclei conserve to some extent their individuality. The evolution

of the DNS can result in the separation of the reaction products after the interchange of nucleons or in a complete fusion of the two nuclei. The separation of the DNS before forming a fused system has been called in different ways: quasi-fission [10], deep inelastic transfer [11], strongly damped collisions [12] and relaxation phenomena [13].

In our present study we are particularly interested in the multi-nucleon transfer reactions in heavy collision systems like ^{58,64}Ni + ^{207}Pb. The multi-nucleon transfer reactions in such systems are mainly dominated by the deep inelastic component. In the following, the term Deep Inelastic Transfer Reactions (DITR) is going to be used for these kind of reactions involving multiple nucleon transfers and a high amount of dissipated energy.

A peculiarity of the DITR is the combination of the properties of both, direct and CN reactions. DITR are not symmetric with respect to 90° in the center of mass system like direct reactions, instead they present the characteristics of a fast direct peripheral collision where a large percentage of the products are emitted at forward angles. Nevertheless, some reaction products may present an orbiting-like behavior (emission at negative angles). The mass and charge distributions of the products are close to those of the parent nuclei. On the other hand, like CN reactions, the kinetic energy of the products is close to the exit channel Coulomb barrier and independent of the beam energy. The production cross-section of individual isotopes shows some regularities indicative of partial statistical equilibrium in the system.

In the following section more details of the general characteristics of the DITR will be provided for a better understanding of the process.

1.1 Experimental Methods to Study Deep Inelastic Transfer Reactions

From the experimental point of view it is important to stress that DITR are two-body processes which means that only two fragments are formed in the exit channel. In this sense it is in principle enough to measure the energy spectrum, angular distributions and cross-sections for only one fragment and obtain information on the other product considering the two-body break-up and the conservation laws. The proof of the two-body nature of the process has been obtained experimentally measuring the angular and energy distributions of the two conjugate reaction products. As an example, Fig 1.1 shows a pronounced peak at 180° in the center of mass system for the reaction ^{58}Ni

+ ^{40}Ar at 280 MeV [14] , which indicates that the products are emitted in opposite directions, a characteristic of two-body processes.

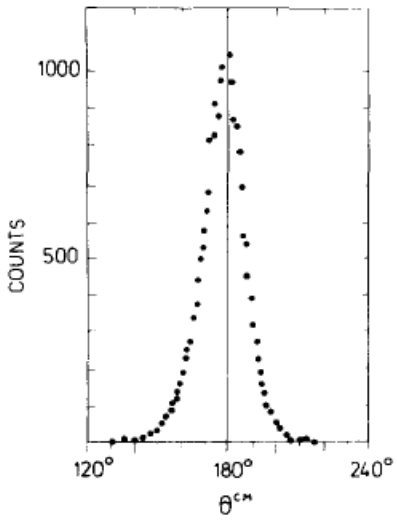

Figure 1.1: Number of deep inelastic events in the reaction ^{58}Ni + ^{40}Ar at the beam energy 280 MeV [14] as a function of the relative angles between the two conjugate reaction products in the center of mass system.

In-beam experimental techniques used to study these reactions are mainly based on the ΔE-E principle. This method uses a telescope consisting of a thin and thick semiconductor detector. The ΔE detector measures the energy loss in a known thickness and the second detector determines its residual energy. These two magnitudes can be used together with the stopping power (-dE/dx) and ranges to determine the mass number A and charge Z of the particle (details in [15]):

$$\Delta E = \int_{R(E_0,Z,A)-d}^{R(E_0,Z,A)} -\frac{dE}{dx}(E,Z,A)\,\mathrm{d}x \tag{1.1}$$

where,

ΔE is the energy loss in the ΔE detector.

$\mathbf{E_0}$ is the initial energy of the particle ΔE + E.

d is the thickness of the ΔE detector.

R(E_0,Z,A) is the range of the particle in the material of the ΔE detector.

-dE/dx(E,Z,A) is the rate of energy loss in the ΔE detector.

The energy loss rate is described by the non-relativistic Bethe-Bloch equation which can be written as:

$$-\frac{dE}{dx} = \frac{4\pi n Z^2}{m_e v^2}\left(\frac{e^2}{4\pi\varepsilon_0}\right)^2 \ln\frac{2m_e v^2}{I} \tag{1.2}$$

where v is the velocity of the particle, m_e is the rest mass of the electron, e is the charge of the electron, ε_0 is the vacuum permittivity, n and I are the electron density and the mean excitation potential of the material, respectively.

This technique is suitable to identify light particles and the resolution is not sufficient to unambiguously identify heavier ones. In this sense the studies are mainly based on the identification of the lighter products (examples in [11, 16–19]). Modern facilities generally integrate time of flight detectors to improve the particle identification. Relatively large reaction cross-sections are needed on the order of microbarns if no separation facility is used. A more recent example of the utilization of the method was the study of the reaction ^{58}Ni + ^{208}Pb in the Laboratori Nationali di Legnaro [20]. The light particles resulting from the reactions were detected using the time of flight spectrometer PISOLO and the heavy particles associated in the reaction were detected in kinematic coincidence using a transmission-type multiwire parallel-plate avalanche counter (MWPPAC). The mass and nuclear charge resolution of PISOLO are $\Delta A/A \simeq 1/100$ and $\Delta Z/Z \simeq 1/60$ which are similar to the resolutions achieved in similar set ups nowadays. Reaction products with Z>60 or A>100 can not be resolved with one unit accuracy.

On the other hand, experiments have been also performed where the identification of the reaction products is achieved by off-beam radiochemical methods [21–27]. Generally these methods are characterized by a precise determination of the mass and proton number. Cross-sections on the order of 10 nb have been measured. The main limitation comes from the relatively long times (t>10 s) required in the identification process.

1.2 Characteristics of Deep Inelastic Transfer Reactions

In the following the results of the study performed with the reaction ^{40}Ar + ^{238}Th [11] will be used as an example. In this experiment, the ΔE-E technique was used to identify the reaction products. The ^{40}Ar energy was 388 MeV in the laboratory frame

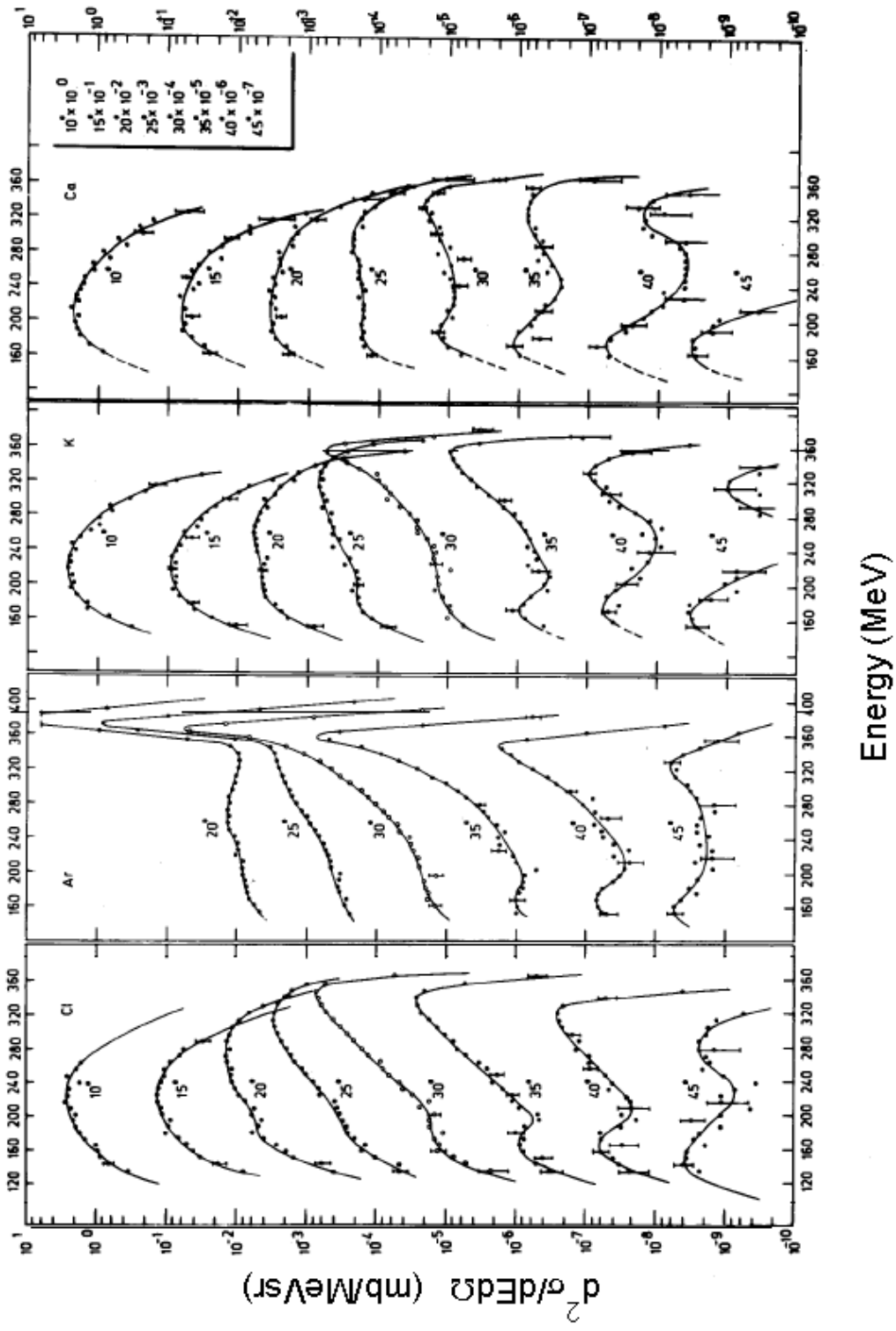

Figure 1.2: Laboratory energy spectra of the transfer products Cl, Ar, K, and Ca produced in the reaction ^{40}Ar + ^{238}Th at the beam energy 388 MeV at different angles taken from [11]. A multiplying factor is shown in the upper right corner used for a better visibility of the graphs.

which is about 170 MeV above the Coulomb barrier. The energy spectra of the DITR products are shown in the Fig 1.2. The spectra extend over more than 200 MeV. The full energy dissipation can occur even for one or two proton transfers and also for the inelastic scattering of the ^{40}Ar nuclei.

A sharp peak can be seen in the energy spectra of the Cl, Ar, K and Ca (ΔZ=-1,0,1,2) for relatively high energies and angles close to the grazing angle θ_{gr}=33°. These contributions come from stripping and pick-up reactions of one and two protons in quasi-elastic reactions. A different situation is observed for smaller and larger angles where the low energy part of the spectrum dominates. In resume, for few-nucleon transfer reactions at grazing angles quasi-elastic reactions dominate while at smaller and larger angles the highest contribution comes from deep inelastic reactions.

Fig 1.3 shows the energy spectra of elements from S to Al corresponding to the transfer of 2 to 5 protons, respectively, and approximately the same number of neutrons. When the number of transferred protons increases the high energy component is smaller and the energy spectra are more symmetric. The widths of the energy spectra generally decreases for increasing number of transferred protons. They also decrease for increasing angles. The energy of the maxima increases as the angle decreases. These maxima are in good agreement with the energy of the exit Coulomb barriers for these projectile-like and target-like combinations and they do not depend on the bombarding energy. It can be concluded that multi-nucleon transfer reactions occur with full dissipation of the initial kinetic energy in deep inelastic reactions.

An explanation for the double peak in the energy spectra can be found in Fig 1.4. The peaks result from the superposition of two different mechanisms: quasi-elastic and deep inelastic reactions. The case number 1 corresponds to small overlap of the nuclear surfaces, short contact times and small energy losses in near Coulomb trajectories. The case number 2 corresponds to strong overlap of the nuclear surfaces, longer contact times, full dissipation of the kinetic energy in the entrance channel and large energy losses. Fig 1.5 shows a convenient manner of presenting the experimental data which is called a Wilczynski diagram [28]. In this particular case the data come from the reaction ^{232}Th(^{40}Ar,K)Ac at 387 MeV. The abscissa shows the c.m energy of the K isotopes produced by the transfer of one proton. The contour lines connect points with the same differential cross-section. Two ridges can be observed in the plot which appear to meet near 0°. One is located close to the grazing angle and large energies of the K isotopes which descend towards smaller angles and energies. The second ridge is located at smaller energies and extends to negative angles. This behavior has

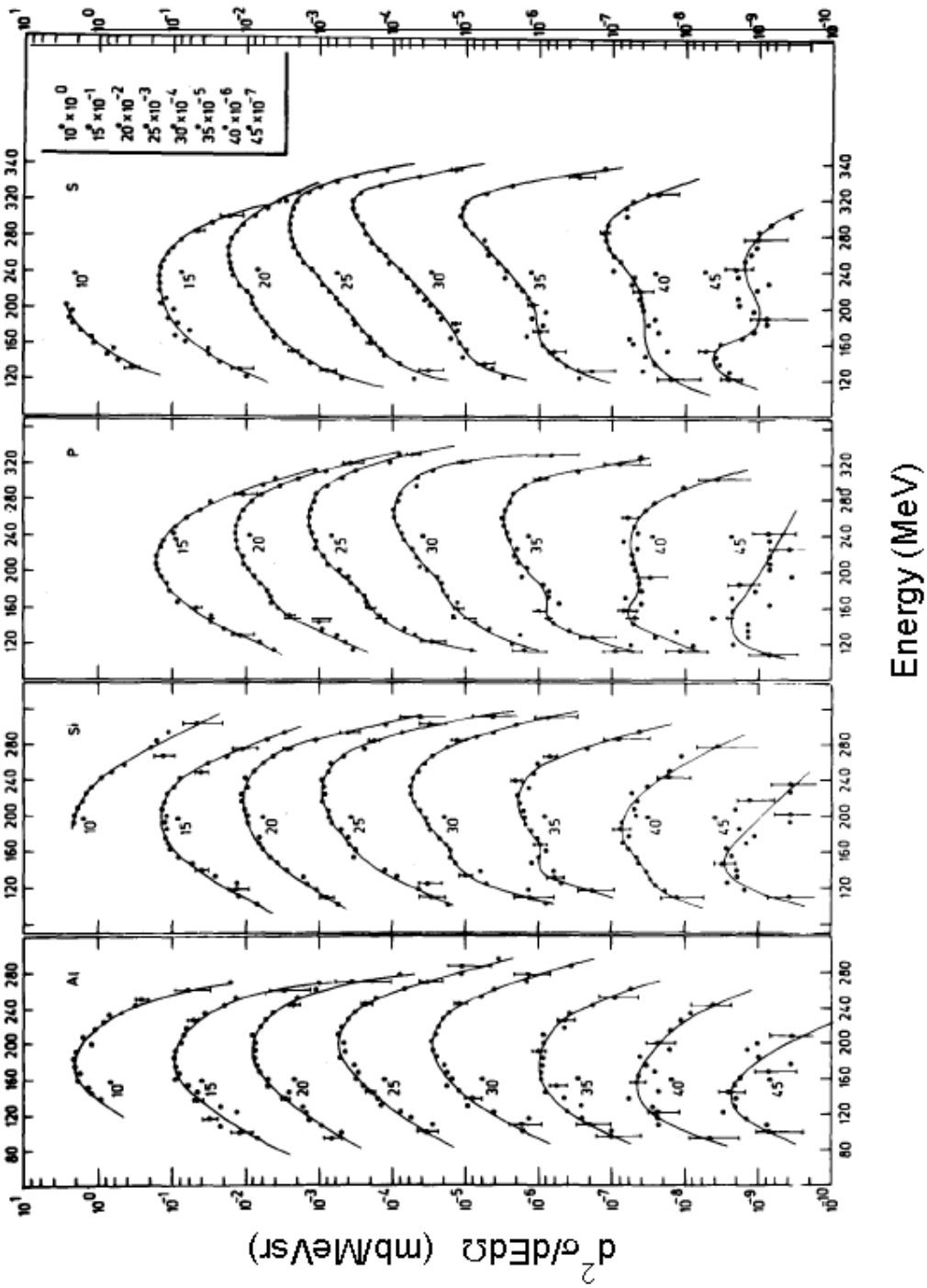

Figure 1.3: Laboratory energy spectra of the transfer products Al, Si, P, and S produced in the reaction ^{40}Ar + ^{238}Th at the beam energy 388 MeV at different angles taken from [11]. A multiplying factor is shown in the upper right corner used for a better visibility of the graphs.

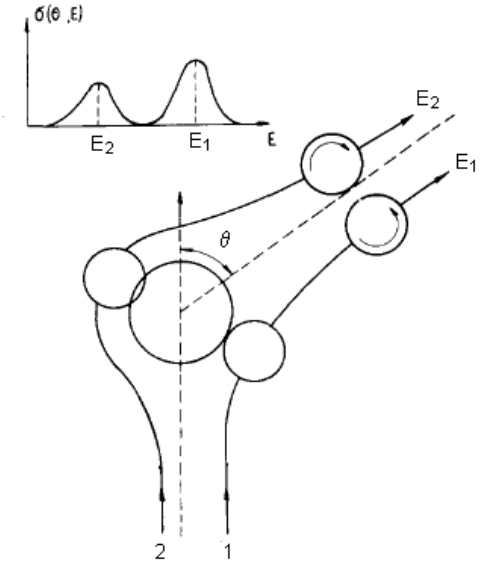

Figure 1.4: Two peak energy distributions, taken from [28], caused by different reaction mechanisms: 1) quasi-elastic, 2) deep inelastic.

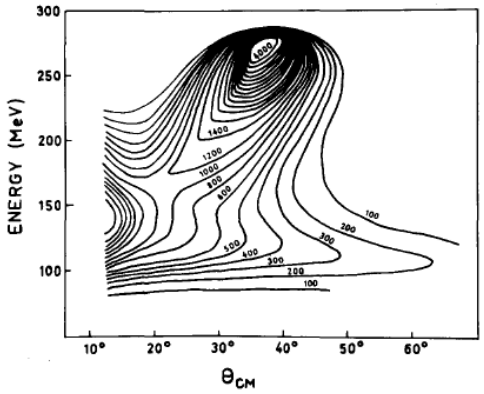

Figure 1.5: Contour diagram for the transfer reaction products in the reaction ^{238}Th(^{40}Ar, K) at 388 MeV, from [28]. The contour lines connect points with the same differential cross-sections $d^2\sigma/dEd\theta$ in units of (μb/MeV.rad). Energies are in the center of mass system.

been explained as a consequence of deflection induced by the nuclear forces from the grazing trajectory towards smaller angles and eventually to negative angles for angular momenta below the grazing angular momentum. The existence of an orbiting nuclear system was predicted in this study. For increasing rotation angles more kinetic energy is dissipated by the nuclear friction forces.

Fig 1.6 shows the angular distribution of the elements from Ne to Ca and from C to Ca for the same reaction at two different beam energies, 288 MeV and 379 MeV respectively. The shape of the distributions change for different number of transferred protons. For a small number of transferred nucleons a peak can be seen close to the grazing angle which corresponds to quasi-elastic transfers. As the number of transferred nucleons increases the maxima become broader with displacement towards small angles.

Angular distributions corresponding to different energy losses during the collision are shown in Fig 1.7 for Al, Cl and K where only few nucleons were transferred. The numbers to the left of the curves represent the energy losses and the inelasticity of the process. As can be seen for the most forward peaked angles, the main contribution comes from larger energy losses in the reaction.

The partial angular distributions for products with Z=53-55 in the reaction of the

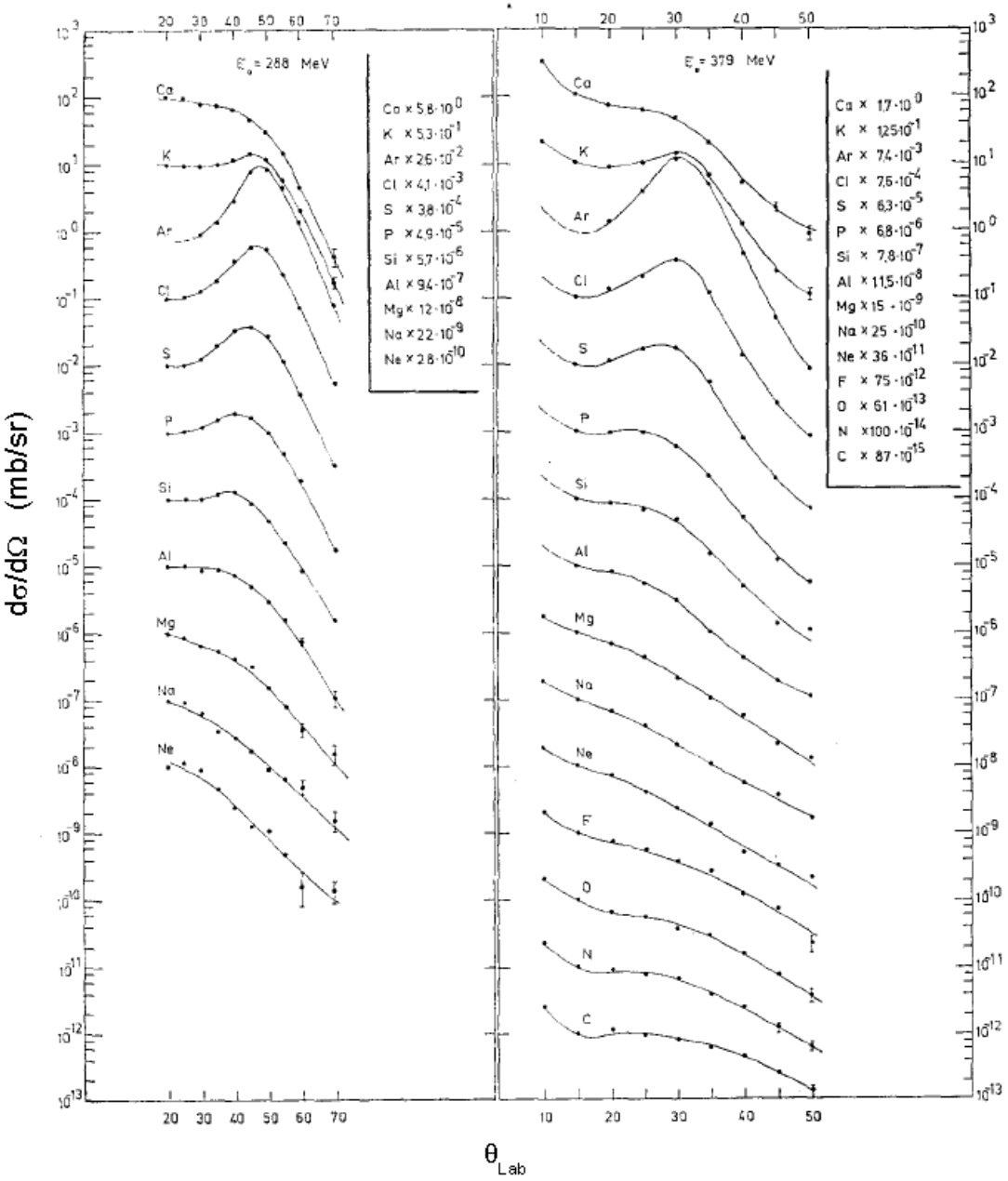

Figure 1.6: Angular distributions of the transfer products from C to Ca in the reaction ^{40}Ar + ^{238}Th at the bombarding energies 288 MeV (left) and 379 MeV (right), from [11]. Each curve has been multiplied by the factor shown in the right side of the graphs.

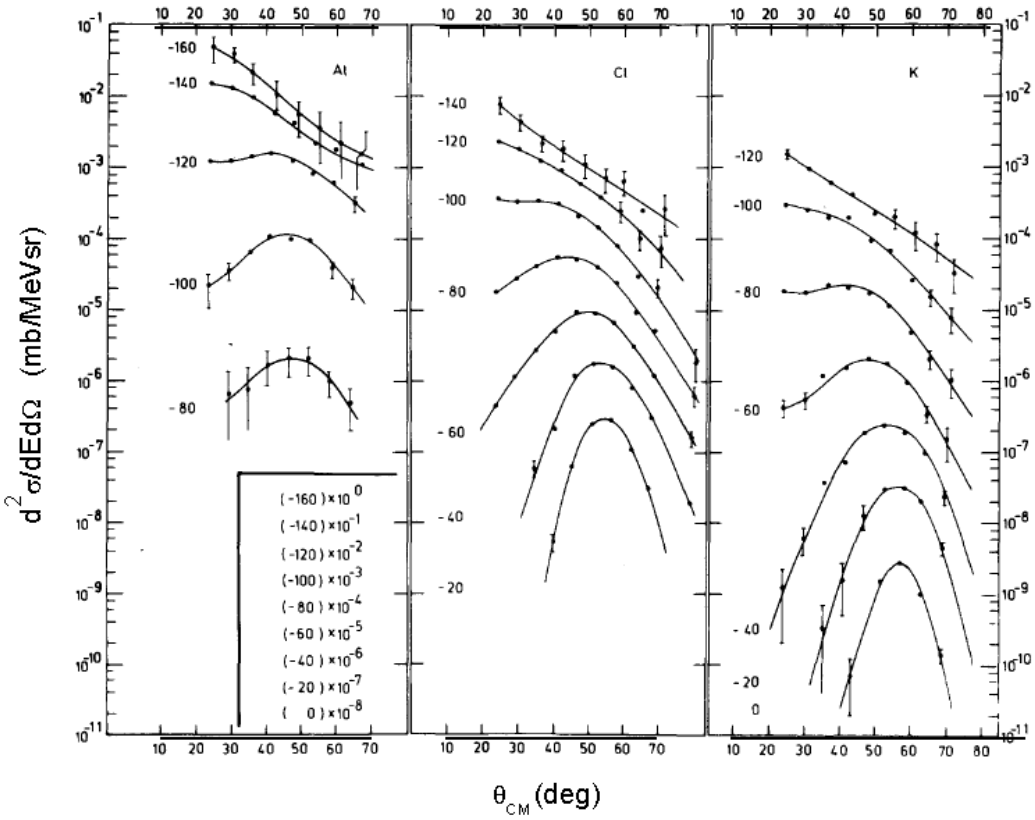

Figure 1.7: Angular distributions of the isotopes K, Cl and Al produced in the reaction ^{40}Ar + ^{238}Th for different kinetic energy losses (numbers near the curves in MeV) at the beam energy of 288 MeV, from [11]. The multiplying factor for each value of the energy loss are given in the table.

very heavy system ^{209}Bi + ^{136}Xe [29] at the beam energy 1160 MeV are shown in Fig 1.8. In this case no dramatic change in the shape of the distribution takes place with increasing energy loss. The curves are symmetric and the maxima are located at the same angle. Only a widening of the distributions can be observed when the inelasticity increases. Generally, the shape of the angular distributions in DITR depend on the Z and A of the colliding nuclei.

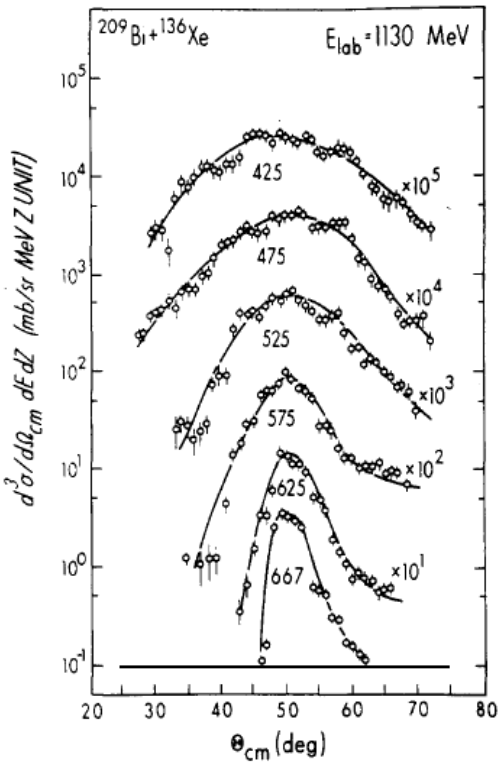

Figure 1.8: Angular distributions for produced isotopes in the range Z=53-55 (elements adjacent to Xe) [29] in the reaction ^{209}Bi + ^{136}Xe at the beam energy E_{lab}=1130 MeV for different total kinetic energies of the reaction products represented by the numbers below the plots in MeV.

1.3 Theoretical Models

Theoretically a large variety of concepts has been applied to these reactions which are related to classical and statistical mechanics, fluids, thermodynamics and the traditional methods of quantum nuclear theory. A common trend of the models is that at some

point the full quantum treatment of the complex many-body problem is substituted by performing some statistical averages over certain microscopic degrees of freedom and taking classically others.

Examples of applied models are the time-dependent Hartree Fock method developed by the Oak Ridge group [30–33], the statistical theory of transport phenomena by Nörenberg [34–36], the diffusion model of Moretto and Sventek [9, 37, 38], the one-body dissipation model of Swiatecki [39–42] and the two center shell model of Greiner and collaborators [43–45].

Generally, the existing models can be divided in dynamical models and statistical (diffusion) models. Macroscopic dynamical models are based on classical and macroscopic properties of the interactions between the heavy ions. The ions move on classical trajectories subject to conservative and dissipative forces. In microscopic dynamical models, the dissipation of energy is treated using collective excitations like surface vibrations, giant resonances and particle-hole excitations. The motion of the ions is also described in classical terms.

In the statistical models more weight is given to the process of energy and nucleon exchange between the nuclei and the evolution of the system in time. As it was first shown by Nörenberg these reactions can be properly described using the equations for non-equilibrium statistical processes like the Fokker-Planck equation. In this sense the energy and nucleon interchange can be considered as a diffusion process. In the one dimensional case this equation is:

$$\frac{\partial P(x,t)}{\partial t} = -\upsilon \frac{\partial P}{\partial x} + D\frac{\partial^2 P}{\partial x^2} \tag{1.3}$$

Where P(x,t) is the probability to find the system in the state x at the time t; υ and D are the drift velocity and the diffusion coefficient, respectively, which remain constant in the process. If the coefficients υ and D are constant the solution of the equation has a gaussian form:

$$P(x,t) = \frac{1}{\sqrt{4Dt\pi}} \exp -\frac{(x-vt)^2}{4Dt} \tag{1.4}$$

The maximum of this function <x> moves along the x coordinate with constant drift velocity v and the dispersion (the square of the full width half maximum (FWHM)) depends linearly on the time. Differences can still be found within the diffusion models as it will be described in more details in the next section.

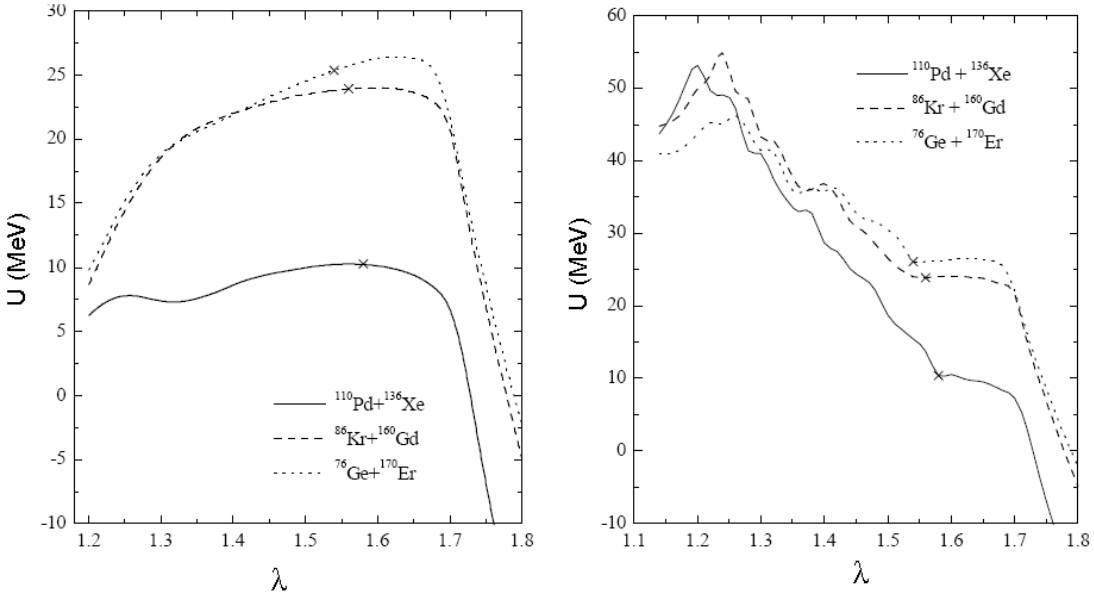

Figure 1.9: (Left) Adiabatic potential for different reactions leading to the nucleus ^{246}Fm as a function of the parameter λ which is directly related to the distance between the nuclear centers (see text). (Right) Dynamical diabatic potential for the same reactions. The crosses represent the contact configurations [46].

In the following, general characteristics of two models developed in Dubna by different groups will be presented. These two models are among the most used ones nowadays for describing the DITR and fusion reaction processes. The dynamics of the process can be generally described by the potential energy using the Strutinsky method. It can be written as a liquid drop like part and one describing the shell effects:

$$U = U_{liquiddrop} + \delta U_{shell} \tag{1.5}$$

The shell effects in the nucleus-nucleus collisions are well described using the two-center shell model of Maruhn and Greiner [47] together with adiabatic and diabatic potentials. Adiabatic potentials are built by minimizing the energy for a given set of collective variables. They allow the CN formation as a melting of the two partner nuclei moving in the relative distance coordinate R and in the mass asymmetry coordinate η=A_1-A_2/A_1+A_2. They have an outside barrier but generally no further barrier for smaller R. The potentials are relatively small for symmetric systems ($\eta\sim0$) which result in relatively large transfer and fusion cross-sections for reactions with $\eta\sim0$. In the case of very heavy and symmetric systems like U + U the models using this potential predict large interaction times and large cross-sections for deep inelastic transfer reactions.

Diabatic potentials take into account the relative motion of the nuclei and the influence of the Pauli principle obligating the nucleons to move in diabatic paths. They consider the transfer and fusion processes as a collective motion in the η coordinate maintaining the relative distance fixed. The potentials are strongly repulsive in the relative distance coordinate preventing the fusion in this coordinate. Fig 1.9 shows a comparison of the two different potentials for the same reactions leading to the CN ^{246}Fm [48] as a function of λ which is defined through the total length of the formed system as: total length = R_1+R_2+r = $2R_0\lambda$ (R_0 is the radius of the spherical CN, $R_{1,2}$ are the radii of the fragments and r the distance between the nuclear centers). As it can be seen there is an inner barrier of around 50 MeV in the case of diabatic potentials which is absent in the adiabatic ones.

Diabatic potentials also show an inner barrier in the η coordinate for asymmetric fragmentation and favor the separation in symmetric fragments. This potential depends strongly on the deformation as can be seen in the Fig 1.10 [49]. The inner barrier characteristics determine the probability of fusion compared to quasi-fission reactions. These models predict low transfer probabilities for very heavy and symmetric systems.

Especially, the two models predict different results for reactions with very heavy

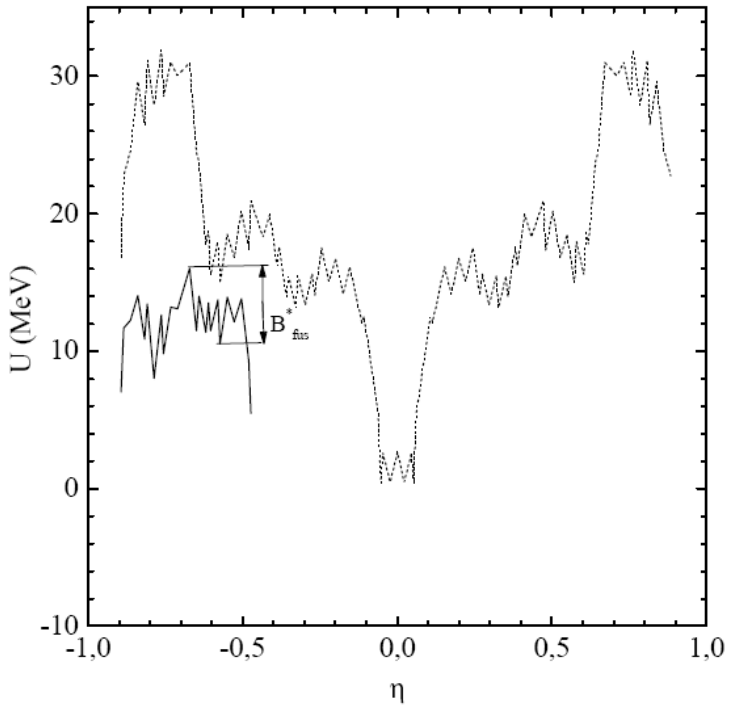

Figure 1.10: Potential energy of the di-nuclear system formed in the reaction ^{54}Cr + ^{208}Pb as a function of the mass asymmetry coordinate η. The dotted curve is calculated for spherical shapes of the nuclei and the solid curve includes deformation in pole-to-pole orientations [49].

ions like U+U, Th+Cf and U+Cm. In the adiabatic models, multi-nucleon transfer can occur in such reactions with relatively large cross-sections in contradiction with the predictions of the diabatic models, where only direct transfer reactions are expected. The differences can only be resolved by means of experimental studies and they are of extreme importance and necessity in order to better understand the transfer and fusion processes as a whole.

Chapter 2

Experimental Setup and Methods

In order to reach low cross-section levels experimentally on the order of nanobarns to picobarns, it is required to use efficient separation techniques and very sensitive identification methods. The most effective methods applied nowadays are the in-flight separation methods used for the production and study of superheavy nuclei. They use electric and magnetic fields to separate the different reaction products: fusion evaporation residues (ER) from elastically scattered target ions, projectiles, projectile-like and target-like transfer products. They can be divided into two groups: the Wien filters and the gas filled separators.

The Wien filters use the differences in the velocities of the reaction products for the separation process. Crossed electric and magnetic fields allow particles with the selected velocity to pass through the filter towards the detection system. Examples of Wien filters are the velocity filter SHIP [50] located at GSI, Darmstadt and VASSILISSA [51] at JINR, Dubna.

Gas-filled separators use the differences in the magnetic rigidities of the reaction products flying in a gas filled chamber (usually Helium) with a magnetic dipole field applied. The interactions of the reaction products with the gas atoms are used to achieve an average charge state of the ions improving the efficiency of the separator. Examples of such separators are the Dubna Gas Filled Recoil Separator (DGFRS) [52] in JINR, Russia; the GAs-filled RecoIl Separator (GARIS) [53] in Riken, Japan; the Berkeley Gas filled Separator (BGS) in LBNL, USA, the Recoil Ion Transport Unit (RITU) [54] in Jyväskulä, Finland and the TransActinide Separator and Chemistry Apparatus (TASCA) in Darmstadt, Germany [55].

The advantages of using in-flight separators are the relatively short separation times

on the order of microseconds and the strong background suppression which allows to measure reaction products produced with low cross-sections on the order of nanobarn to picobarn.

2.1 Velocity Filter SHIP

SHIP [50] is located at the beam line of UNILAC (UNIversal Linear ACcelerator) at GSI. The accelerator can deliver beams of any stable isotope up to uranium at relatively high intensity up to $\sim$ 1pμA (6.24×10^{12} particles/s) and energies up to 20$\times$A MeV. The beam is delivered in a pulsed structure consisting of 5 ms long pulses and 15 ms long beam-off periods.

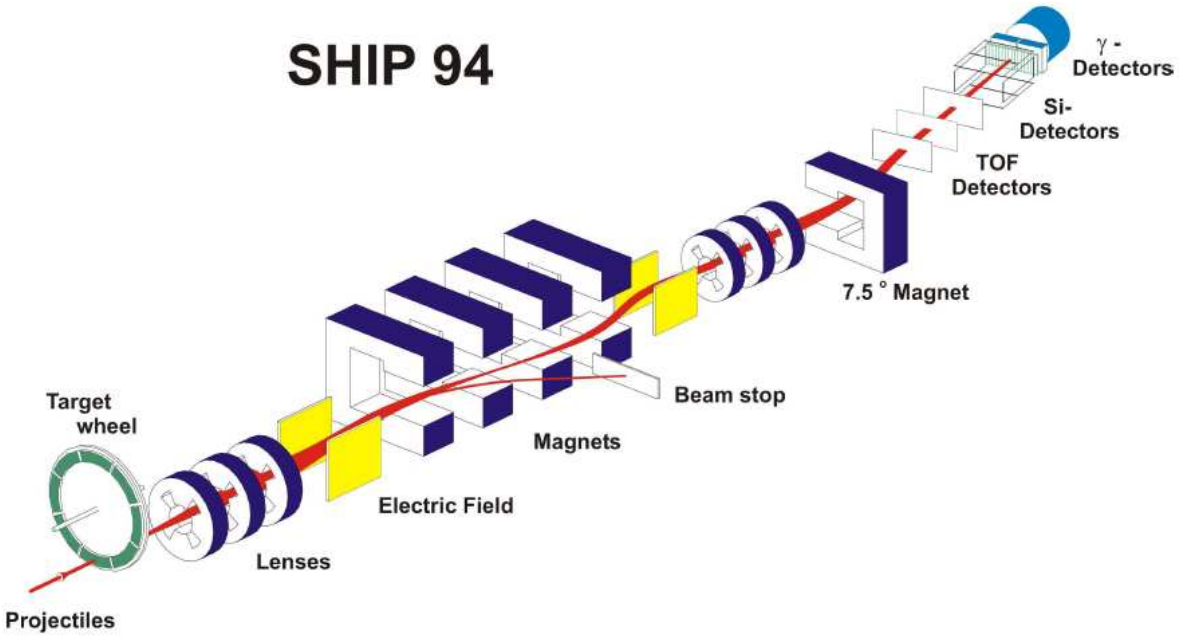

Figure 2.1: Schematic drawing of the velocity filter SHIP and its detection system [50]. The total length is 11 m.

SHIP, represented in the Fig. 2.1, is a Wien filter which has been designed to separate heavy evaporation residues from the beam particles, projectile-like and target-like transfer products based on the difference in their velocities. It consists of two stages of velocity separation with separated electric and magnetic fields. The first quadrupole triplet collects and focuses the reaction products created at the target

position. Then, a combination of magnetic and electric fields filters the beam and unwanted reaction products from the wanted ones. A second quadrupole triplet focuses the filtered products to the detection system. An additional dipole magnet is placed after the last quadrupole triplet and provides an additional deflection up to 7.5°. This last deflection reduces the background due to scattered projectiles with low charge state which reach the focal plane. The flight time of the reaction products through SHIP is $\sim$2 μs.

Reaction products leaving the target within a 2° cone with respect to the beam direction in the laboratory frame are accepted by SHIP. This characteristic makes it suitable for fusion and transfer reaction studies at relatively low energies close and even below the Coulomb barrier where mainly almost central collisions take place and the products are emitted in small angles relative to the beam direction.

Fixed targets can not withstand the long irradiation times and high beam currents delivered by the UNILAC. Therefore eight targets of 112×24 mm^2 are mounted on a 310 mm diameter rotating wheel. The rotation is synchronized with the beam macrostructure. In our experiments ^{207}PbS targets were used which have a relatively high melting point of 1118° . These targets are produced by evaporation of a ^{207}PbS layer, usually 350-450 μg/cm^2, onto a 40 μg/cm^2 heated carbon foil. Another thin carbon layer of 10 μg/cm^2 is then evaporated onto the PbS (for target preparation details see [56]).

The targets are cooled in vacuum by radiative cooling using two metal plates with a temperature of $\approx$ 245 K. The target thickness is controlled online by registration of scattered electrons of 20 keV [57].

A thin carbon foil of $\sim$40 μg/cm^2 is mounted behind the target to get an additional charge state equilibration of the reaction products before entering to SHIP. The charge state of the products can change after leaving the target by internal conversion and/or Auger electron emission from the decay of short living isomeric states.

2.2 Detectors

The detection system of SHIP consists of three time of flight (TOF) detectors, seven 16-strip silicon wafers and a 4-crystal germanium detector (Fig. 2.2). One of the seven 16-strip wafers is installed as stop detector and the others are used to form a box-like backward detector.

The active area of each silicon wafer is 35×80 mm^2. Each strip is 5 mm wide

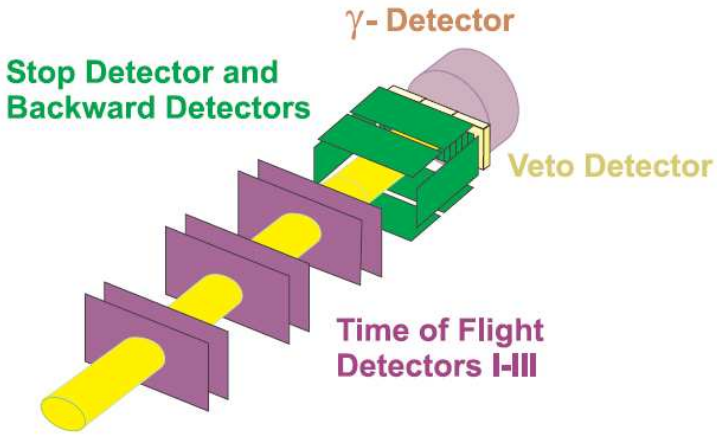

Figure 2.2: Schematic drawing of the detection system. It consists of three time-of-flight detectors, the position-sensitive silicon stop and backward detectors, the veto detector and the germanium γ-detectors.

and position sensitive in the vertical direction with a resolution of 150 μm FWHM for α-decays of implanted nuclei. The stop detector is the equivalent to 3700 single detectors each with an active area of 0.15×5 mm^2. The energy resolution is 14 keV for α-particles from a ^{241}Am external source or α decays of implanted nuclei. Six wafers are mounted in the backward hemisphere of the stop detector. They measure the escaped α-particles and fission products from the stop detector with a solid angle of 80% of 2π. In the backward detectors neighboring strips are connected galvanically forming 28 energy-sensitive segments. The direction of the escaping particle can be roughly retraced. The energy resolution for an escaped α-particle summing the energy signals of both, stop and backward detectors, is 40 keV. All silicon detectors are cooled to 263 K using alcohol.

The stop detector efficiency can be estimated approximately as the geometrical efficiency of the silicon detector (Fig 2.3). The efficiency depends on the reaction product's implantation depth and the particle range in silicon. As an example, the typical ranges are 5 μm for 30 MeV ^{238}U and d$_\alpha$=50 μm for α particles of 8 MeV. Using these values we can calculate:

$$\frac{d_{Re}}{d_\alpha} = \cos\varphi \Rightarrow \varphi = 84.3^\circ \tag{2.1}$$

The efficiency of the stop detector for α particles in the present example can be

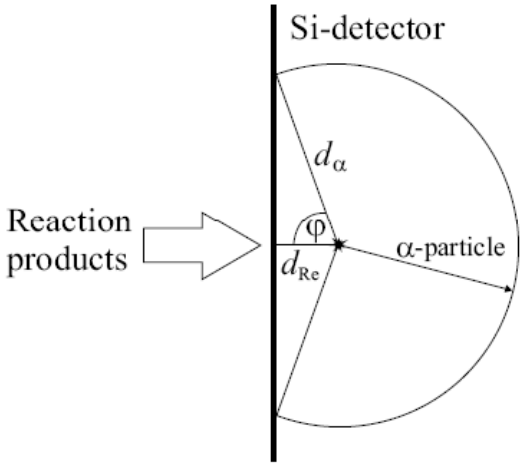

Figure 2.3: Schematic drawing of the implantation of the reaction products in the stop detector and the subsequent α-decay. d_{Re} and d_α are the ranges of the evaporation residue and α-particle in silicon. φ is the emission angle of the α-particle.

estimated as:

$$\frac{4\pi - 2\pi(1-\cos\varphi)}{4\pi} = 0.55 \Rightarrow 55\% \tag{2.2}$$

In general, for transfer reactions the energies of the target-like reaction products can cover a wide energy range up to 180 MeV in the Ni+Pb reactions and the beam energies included in the present study. Therefore, the implantation depth can vary from few micrometers up to ∼20 μm. The stop detector efficiency must be calculated for the different possible implantation depths.

The TOF detectors are schematically shown in Fig 2.4 [58]. They are three secondary electron foil detectors mounted at a distance of 150 mm apart from each other (Fig 2.4, (b)). Each detector is made of two foils of carbon of 30 μg/cm^2 thickness with nearly 100% transmission and a time resolution of ∼700 ps. Between the foils, an electric potential of ≈4 kV and a perpendicular magnetic field are applied in order to accelerate and bend, respectively, the emitted electrons when a heavy ion passes through the foils (Fig 2.4, (a)). The electrons are directed to a microchannel plate (MCP) for further amplification and detection.

An additional silicon detector, called Veto detector is located behind the stop detector. It is used to register particles which penetrate through the stop detector.

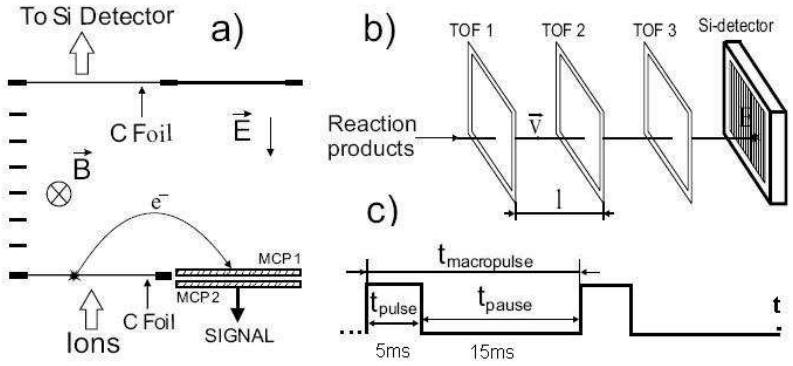

Figure 2.4: a) Schematic drawing of the working principle of the TOF detectors. b) Location of the three TOF detectors in front of the stop detector, l=150 mm. c) pulse structure of the beam.

The germanium CLOVER detector is installed behind the stop detector and it consists of four crystals which register the X-rays and γ-decays in coincidence with the decay of implanted reaction products within a time of 5 μs.

2.3 Isotope Identification

Fig 2.5 shows schematically the α-decay of an implanted reaction product in the detection system of SHIP. A reaction product usually generates a signal in the TOF detectors before it is implanted in the stop detector. This signal can be used to differentiate it from implanted product decays. From the measured time of flight and the energy, it is also possible to plot a TOF versus energy spectrum (Fig 2.6) which can be used to differentiate between the different reaction products. Different masses generate different branches in the spectrum and a mass resolution value of $\pm$ 10 units can be estimated. This resolution is sufficient to distinguish between projectile-like and target-like reaction products and fusion evaporation residues.

Additionally, the pulse structure of the beam can be used for background reduction. Fig 2.7 shows the energy spectra measured with the stop detector for the low energy interval 5500 - 9000 keV. The red spectrum includes all events measured during beam-on as well as in beam-pause while the black curve shows only the events measured during beam-pause. As one can see, a considerable background reduction is obtained using the beam-pause condition.

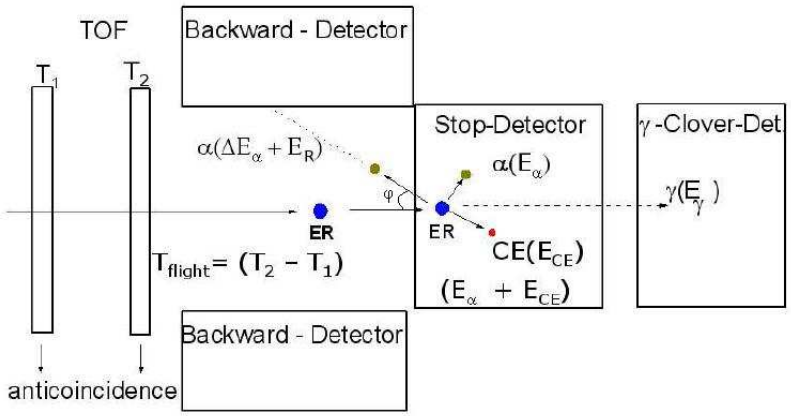

Figure 2.5: Schematic drawing of an evaporation residue implantation in the stop detector with it's subsequent α-decay. Conversion electrons (CE) are also detected. Gamma-rays emitted in the decay process are detected in the germanium detector.

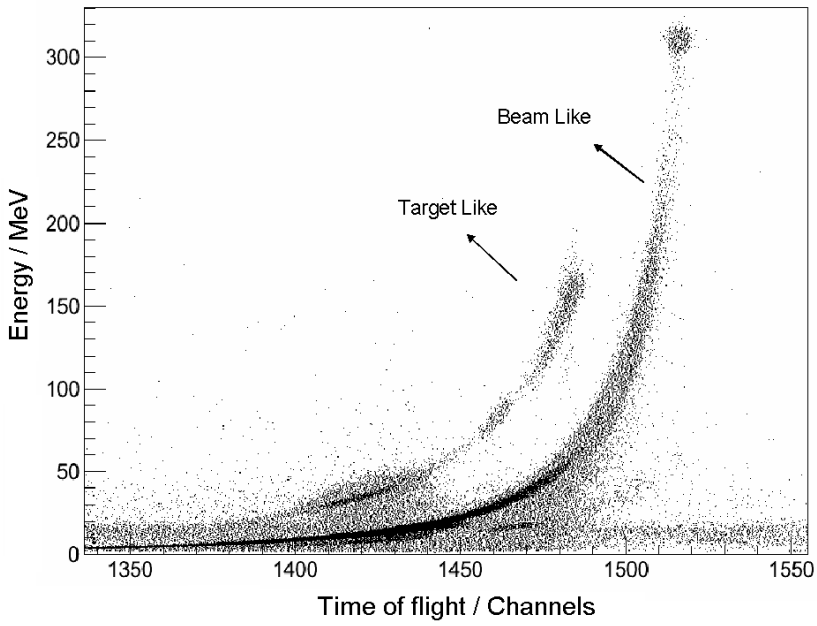

Figure 2.6: Measured TOF versus energy spectrum in the reaction ^{64}Ni + ^{208}Pb at the beam energy 5.0×A MeV. The x-axis represents the time of flight values in channels and the y-axis the energies in MeV. The up-right spot in the graph (E≃320 MeV) originates from projectiles with the original beam energy which reach the focal plane.

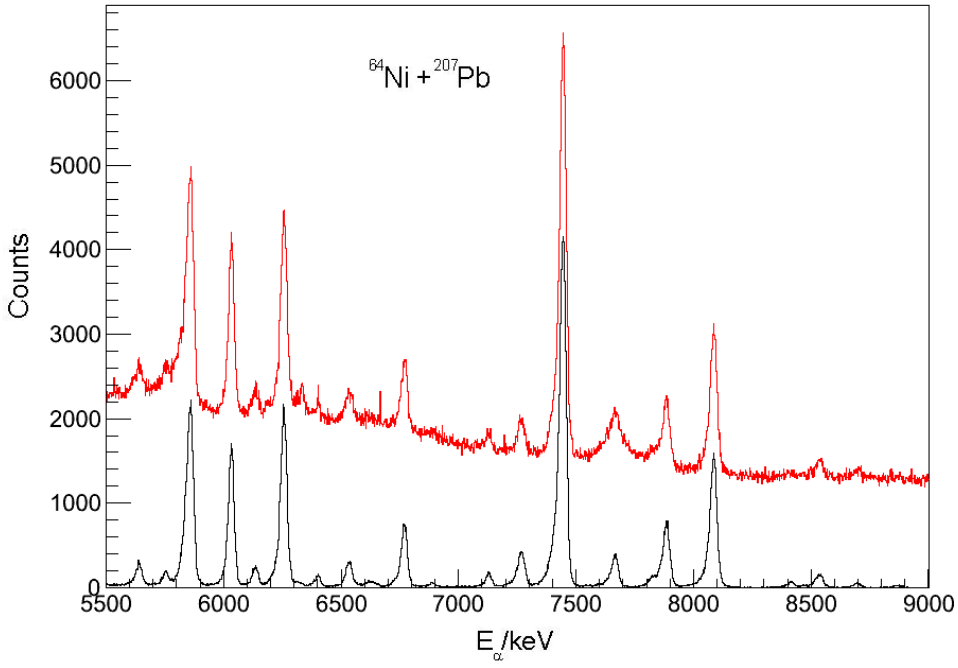

Figure 2.7: Alpha-spectra measured in the stop detector considering events in beam-on as well as in beam-pause (red) and the events only in beam pause (black) in the reaction ^{64}Ni + ^{207}Pb.

The isotope identification is done by measuring the decay properties of the reaction products after they are implanted in the stop detector. If the implanted nucleus is not stable one can follow the decay pattern and identify the isotope. In the present study, a region of mainly α-emitters is populated. In cases where two or more isotopes have close lying α-energies (compared to the detector resolution) and half-lives the following of the α-decay chains can help to distinguish between these isotopes. These methods can also be used to differentiate between nuclei produced directly in the reaction from those produced as a result of mother decay.

The position sensitive silicon strip detectors allow for a chain track analysis shown schematically in the Fig 2.8. It is possible to search for α-decay chains with the proper energy at the same position and in a time window properly adjusted to the reaction products and daughter half-lives.

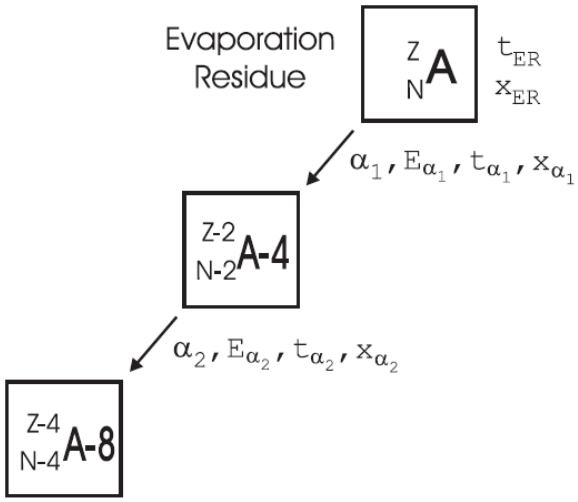

Figure 2.8: Schematic drawing of a ER-α-α correlation chain. Each signal includes the information on the time (t), energy (E), and location (x).

As an example, Fig 2.8 shows the case of a two-step decay chain. Starting from the time t_{ER}, position x_{ER} and energy signals of the implanted evaporation residue it is possible to proceed with its identification. Following the implantation, a search for subsequent α emissions with the specific characteristics of $E_{\alpha 1}$, $t_{\alpha 1}$, $x_{\alpha 1}$ and $E_{\alpha 2}$, $t_{\alpha 2}$, $x_{\alpha 2}$ is performed. The time differences and energies must match the half-lives and energies of the corresponding decay.

In our experiment we used the correlation method to identify mainly the most

neutron-rich nuclei produced in the reaction ^{64}Ni + ^{207}Pb. In these cases the production cross-sections were relatively low.

When a signal is detected a coincidence time of approximately 5 μs is triggered. Within this time all arriving signals are accepted and converted. After this, the readout is triggered and followed by a dead time of approximately 20 μs where all arriving signals are not accepted. The total readout cycle is $\sim$25 μs.

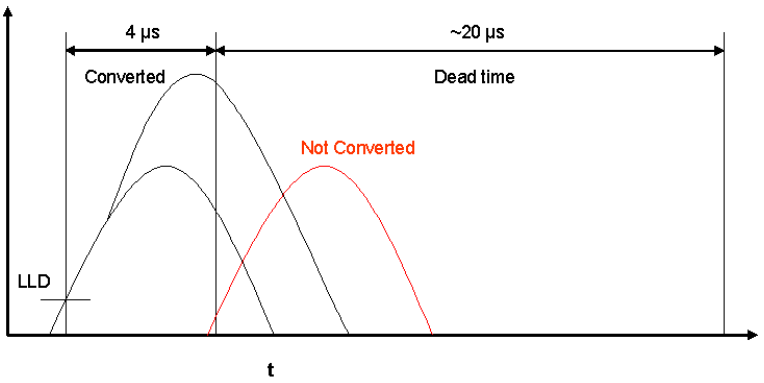

Figure 2.9: Examples of a converted pile-up signal (black) and a not converted signal (red). LLD states for the low level of discrimination of the ADCs.

When an event triggers the coincidence time and is followed by another event in a time shorter than 5 μs, pile-up of both events occurs. Fig 2.9 shows an example of a converted pile-up event and a non converted event (red color). In general the energy signal after a pile-up event will depend strongly on the time of the second event. If the second event comes close to the end of the coincidence time, only a part of the signal will be converted and added to the first event.

2.4 Velocity Distributions

SHIP gives the opportunity to vary the electric and magnetic fields determining at which velocity a particle can pass the filter. The velocity acceptance of SHIP at a certain setting is Δv/v=$\pm$5%. This characteristic can be used to identify the reaction mechanism by measuring the velocity distribution of the reaction products. The velocity spectrum is measured by varying the electric and magnetic fields of SHIP. Typical velocity spectra expected for different reaction mechanisms are shown qualitatively in Fig 2.10. The structure of the spectra is strongly influenced by the narrow acceptance

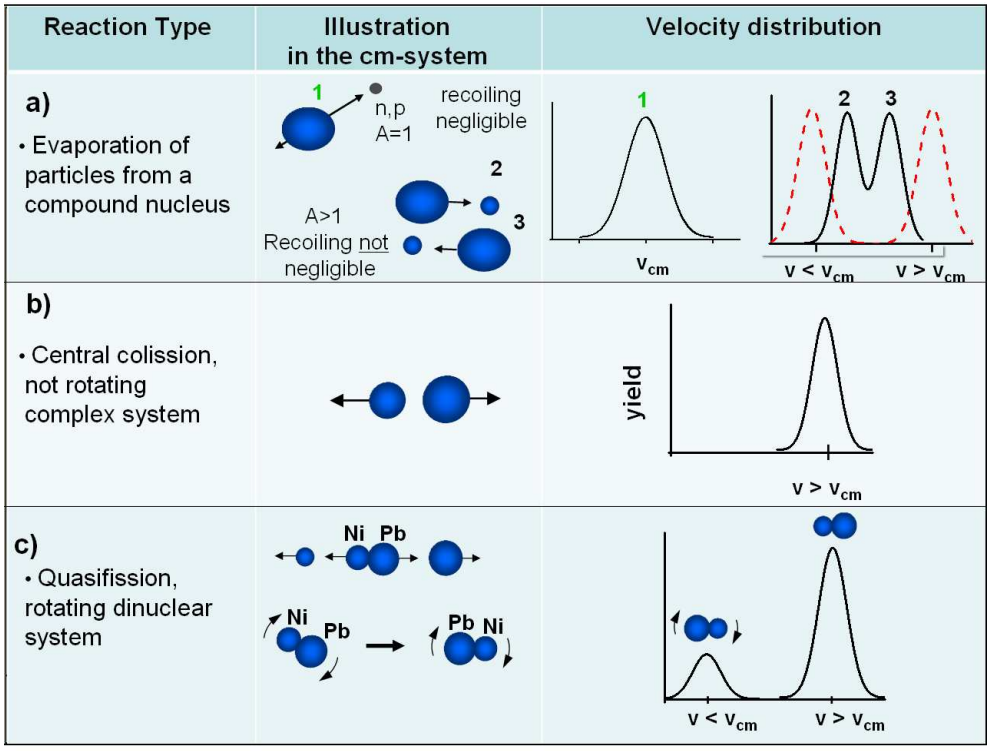

Figure 2.10: General characteristics of velocity distributions determined by the SHIP acceptance angle cone of 2° with respect to the beam direction a) Velocity distributions for reaction products resulting from CN formation with successive evaporation of nucleons or nucleon clusters. b) Velocity distribution from quasi-elastic and inelastic central collisions. c) Velocity distributions resulting from a rotating di-nuclear system.

angle of SHIP. The reaction products resulting from the formation of a CN that de-excites by isotropic evaporation of light particles like single neutrons and protons keep in good approximation the CN velocity v_{CN} (Fig 2.10 a, 1). The single particle evaporation process can not affect noticeably the velocity of the heavy reaction product and the change is smaller than the velocity resolution of SHIP. If heavy clusters are evaporated e.g α, Li, Be, B, C, N, O, etc, the effect on the heavy reaction product velocity is no longer negligible. In these cases only recoils resulting from the cluster emission parallel to the beam line, in forward (Fig 2.10 a, 2) or backward (Fig 2.10 a, 3) directions are accepted by SHIP. In this case the maxima appear at $v=v_{CN}+v_x$ (emission in the backward direction) and $v=v_{CN}-v_x$ (emission in the forward direction), v_x corresponds to the velocity change of the heavy product in the emission process due to recoil, taking the momentum conservation law into account.

Quasi-elastic and deep inelastic central collisions result in single-peaked velocity distributions with peak positions at $v\simeq(1.5\text{-}2.0)v_{CN}$ (Fig 2.10, b).

The velocity distribution of quasi-fission products resulting from a rotating DNS which separate parallel to the beam direction is shown in Fig 2.10 (c). The two velocity components result from the forward and backward emission of the light reaction product, with respect to the beam direction. The labels Ni and Pb in Fig 2.10 (c) are used as examples for a better understanding of the orientations of the nuclei.

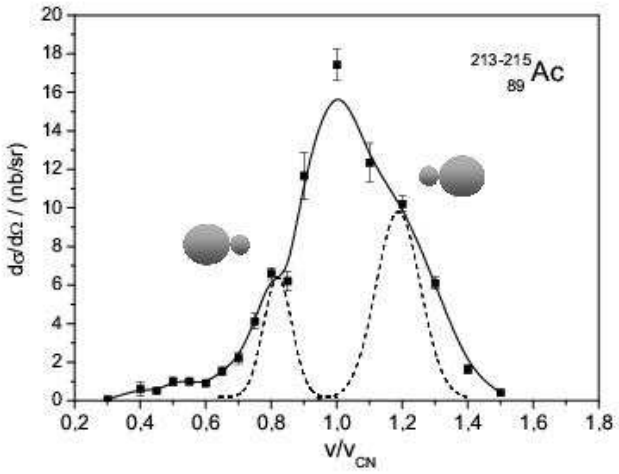

Figure 2.11: Velocity distributions of the isotopes $^{213-215}$Ac produced in the reaction ^{25}Mg + ^{206}Pb at 8.7×A MeV [59].

As an example of single nucleon and cluster evaporation from the CN, the velocity

distribution of $^{213-215}$Ac is shown in Fig 2.11 for the reaction ^{25}Mg + ^{206}Pb at 8.7×A MeV [59]. In this reaction the CN ^{231}Pu was produced. It can be noticed that besides the main peak at v/v_{CN}=1 two shoulders appear at v/v_{CN}=0.85 and 1.15. The main peak comes from the isotropic evaporation of five protons and eleven neutrons. The shoulders can be explained by the de-excitation of the CN via an α3p9n channel leading to velocities of $v=v_{CN}\pm0.15v_{CN}$ in the laboratory system. Schematic drawings of the orientation of the emission of the α-particle is shown in the figure. The difference in intensities of the two shoulders can be explained due scattering in the target.

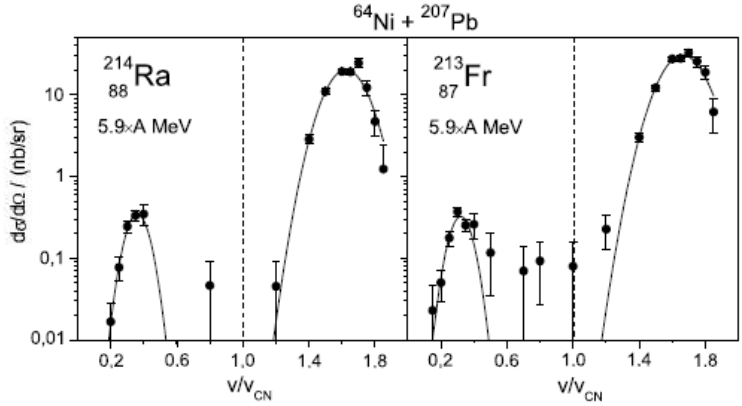

Figure 2.12: Measured velocity distributions of the isotopes ^{214}Ra (left) and ^{213}Fr (right) produced in the reactions ^{64}Ni + ^{207}Pb at the beam energy 5.9×A MeV.

Fig 2.12 shows the velocity distributions of ^{214}Ra and ^{213}Fr which were produced as transfer products in the reaction ^{64}Ni + ^{207}Pb at 5.92×A MeV. Two symmetric components with respect to the compound velocity can be seen. One with relatively high velocity v/v_{CN}=1.7 and the other with v/v_{CN}=0.3. The two components result from a two-body break up after a rotating DNS is formed with the two possible orientations of the nuclei as explained previously. The lifetimes of the di-nuclear system can be estimated from the velocity distributions considering the differences in the cross-sections of the two components as it will be discussed in more details in the Chapter 4.

2.5 Experiments

The reaction ^{58}Ni + ^{207}Pb was investigated in February/2009. Different beam energies were selected with the values 4.85, 5.0, 5.2, 5.4, 5.6 and 5.9×A MeV which correspond to (0.88-1.08) times the interaction barrier according to the Bass model [60] which can

Beam Energy (A MeV)	Velocities
4.85	1.7; 1.85
5.0	1.6; 1.7; 1.8; 1.9; 1.95
5.2	1.7; 1.85
5.4	1.7; 1.85
5.6	1.7
5.9	1.7

Table 2.1: Beam energies and the respective velocities covered in the reaction ^{58}Ni + ^{207}Pb. The velocities are in units of the compound nucleus velocity.

be calculated as:

$$B_{int} = \frac{Z_1 Z_2 e^2}{R_{12}} \left[\frac{R_{12}}{R_{12} + d_{int}} - \frac{1}{x} \frac{d}{R_{12}} exp\left(-\frac{d_{int}}{d} \right) \right] \tag{2.3}$$

where $R_{12} = r_0(A_1^{1/3} + A_2^{1/3})$ with r_0=1.07 fm, A_1 and A_2 are the mass numbers of the projectile and target. The parameters d and d_{int} can be obtained from fits to experimental interaction barriers which result in the values d=1.35 fm and d_{int}=2.7 fm. The parameter x is the relation between the Coulomb and nuclear potential terms, $x = v_{Coul}/v_{Nucl}$ where the nuclear potential is calculated within the nuclear liquid drop model as:

$$v_{Nucl} = -a_s A_1^{1/3} A_2^{1/3} \frac{d}{R_{12}} exp\left(-\frac{r - R_{12}}{d} \right) \tag{2.4}$$

where a_s=18.34 MeV and r is the distance between the nuclear centers. Substituting in eq 2.3 one obtains:

$$B_{int} = \frac{Z_1 Z_2 e^2}{R_{12} + 2.7} - 2.9 \frac{A_1^{1/3} A_2^{1/3}}{A_1^{1/3} + A_2^{1/3}} \tag{2.5}$$

For each beam energy the velocity settings of SHIP were varied and the velocity spectra for the detected isotopes were measured. Table 2.1 shows the velocities covered for each beam energy. Due to the limited beam time the full velocity spectra could not be scanned for every beam energy. In the respective cases, only those velocities were selected where the maxima of the production rates were expected.

The reaction ^{64}Ni + ^{207}Pb was studied in two blocks. One from 21-25/March/ 2008 with the beam energy of 5.92×A MeV. The second block from 15-20/October/

Beam Energy (A MeV)	Velocities
4.8	0.25; 1.4; 1.6; 1.7; 1.8
5.0	0.15; 0.25; 0.35; 1.0; 1.4; 1.5; 1.6; 1.7; 1.8; 1.85
5.2	1.2; 1.4; 1.5; 1.6; 1.7; 1.8
5.4	1.2; 1.4; 1.5; 1.6; 1.7; 1.8
5.53	0.15; 0.25; 0.35; 0.4; 0.5; 0.7; 0.9; 1.0; 1.1; 1.2; 1.4; 1.45; 1.5; 1.55; 1.6; 1.65; 1.7; 1.8
5.92	0.15; 0.2; 0.25; 0.3; 0.35; 0.4; 0.5; 0.7; 0.8; 1.0; 1.2; 1.4; 1.5; 1.6; 1.65; 1.7; 1.75; 1.8; 1.85

Table 2.2: Beam energies and the respective velocities covered in the reaction ^{64}Ni + ^{207}Pb. The velocities are in units of the compound nucleus velocity.

2008 covered beam energies of 4.8, 5.0, 5.2, 5.4 and 5.53×A MeV. The beam energies correspond to (0.95-1.17) times the Bass barrier. Table 2.2 shows the velocities scanned for each beam energy in this reaction using units of the compound nucleus velocity v_{CN}:

$$v_{CN} = \frac{m_p}{m_p + m_t} \times v_p \tag{2.6}$$

where m_p and m_t are the masses of the projectile and target nuclei, respectively, and v_p is the velocity of the projectiles in the laboratory system.

Chapter 3

Results and Discussion

3.1 Isotope Identification via α-decays

Fig 3.1 shows the α-spectra for the ^{64}Ni and ^{58}Ni reactions. The spectra were recorded in beam-off periods following the UNILAC pulses of the beam. In this case, a low background is obtained and many α-lines can be immediately identified. Nevertheless, contributions from different isotopes to the same α-line are possible and each of these cases must be carefully treated.

A region of α-emitters above Z=82 was populated in both reactions. Fig 3.2 shows the region of the nuclear chart populated in transfer reactions using ^{58}Ni beams. Fig 3.3 shows the region populated in the reactions with ^{64}Ni beams. It can be noticed that in general more neutron rich isotopes were produced with ^{64}Ni beams. The isotopes are secondary products which result after de-excitation of the primary products. Nuclei with Z>89 were not detected which might be due to the increasing fission probability for nuclei beyond Z=89 as considered in [20] for the similar reaction, ^{58}Ni + ^{208}Pb, at the beam energy 5.66×A MeV. Nuclei with Z≤82 could not be detected mainly because they are not α-emitters or have too long half-lives. In addition, it was not possible to identify isotopes in the region with N=128,129 due to extremely low half-lives of μs and below. Many of these isotopes decay before reaching the stop detector during the flight time through SHIP (2 μs).

Following the alpha spectra for both reactions (Fig 3.1) one can notice that the most intense α-lines belong to isotopes with neutron numbers up to N=127. Nevertheless, there are some isotopes with N≥130 which are populated with low yields and can be identified following their decay chains. In this sense, the isotopes ^{220}Ra, ^{221}Ra, ^{219}Fr,

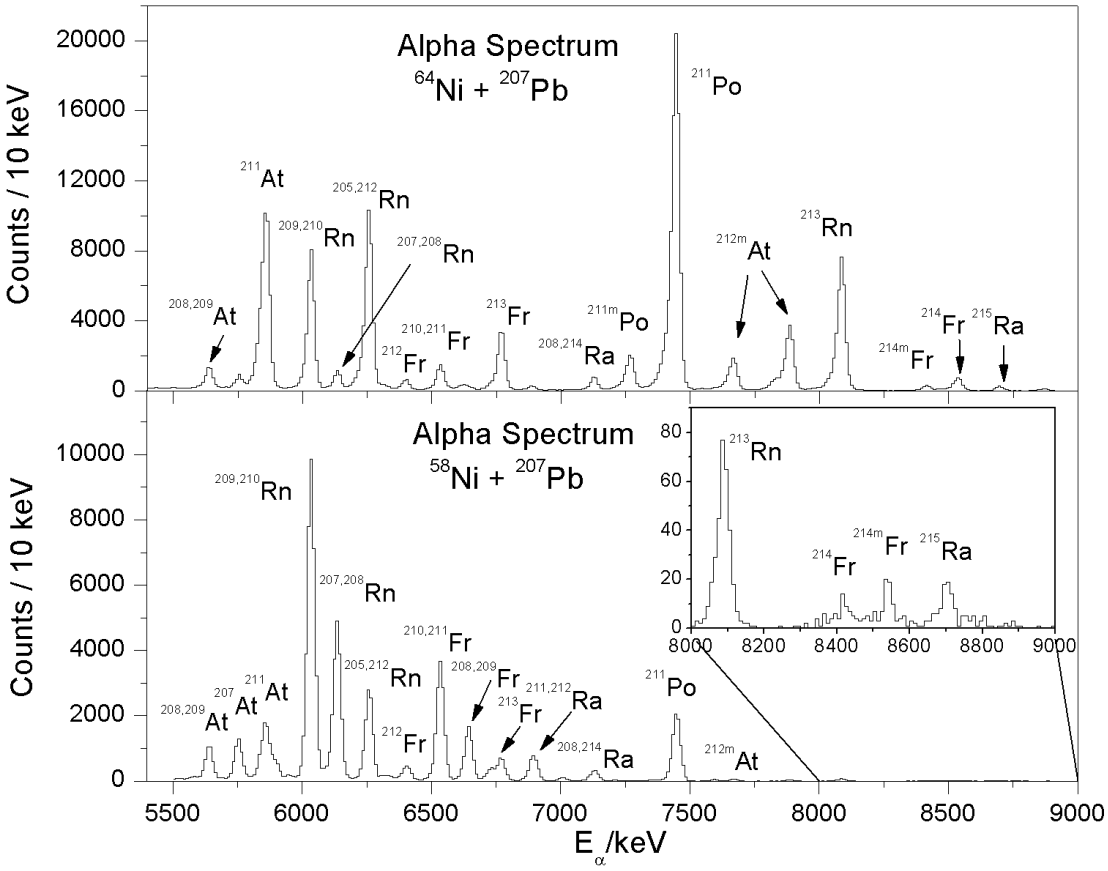

Figure 3.1: Measured α-spectra during beam off periods in the reactions ^{58,64}Ni + ^{207}Pb.

^{218}Fr and ^{216}Rn were identified using the correlation methods described in Chapter 2.

The α-decay chain in the case of the isotope ^{220}Ra is:

$$^{220}Ra(23\,ms, 7450\,keV) \rightarrow {}^{216}Rn(45\,\mu s, 8050\,keV) \rightarrow {}^{212}Po(0.3\,\mu s, 8785\,keV) \quad (3.1)$$

which can be followed in Fig 3.3. The half-lives and α-energies are included in brackets. After the α-decay of the mother nucleus, two consecutive α-decays take place which generate a pile-up event (details Chapter 2). In this case, the extremely low half-life of ^{212}Po compared to the coincidence time of 4 μs results in a full collection of the pile-up energy. In the correlation search, the first *alpha* of the chain is correlated with the pile-up energy of 16835 keV. Fig 3.4 shows for the ^{64}Ni reaction the number of pile-up events in the range of 14.3-18.3 MeV correlated with an α-energy of 7450 keV within a time of 0.225 ms which corresponds to five times the half-live of ^{216}Rn, where the majority of the decays take place ($\simeq$ 97%). Fig 3.4 shows a peak at the expected pile-up energy of 16.8 MeV with rather low statistics, indicating the small production cross-section of ^{220}Ra.

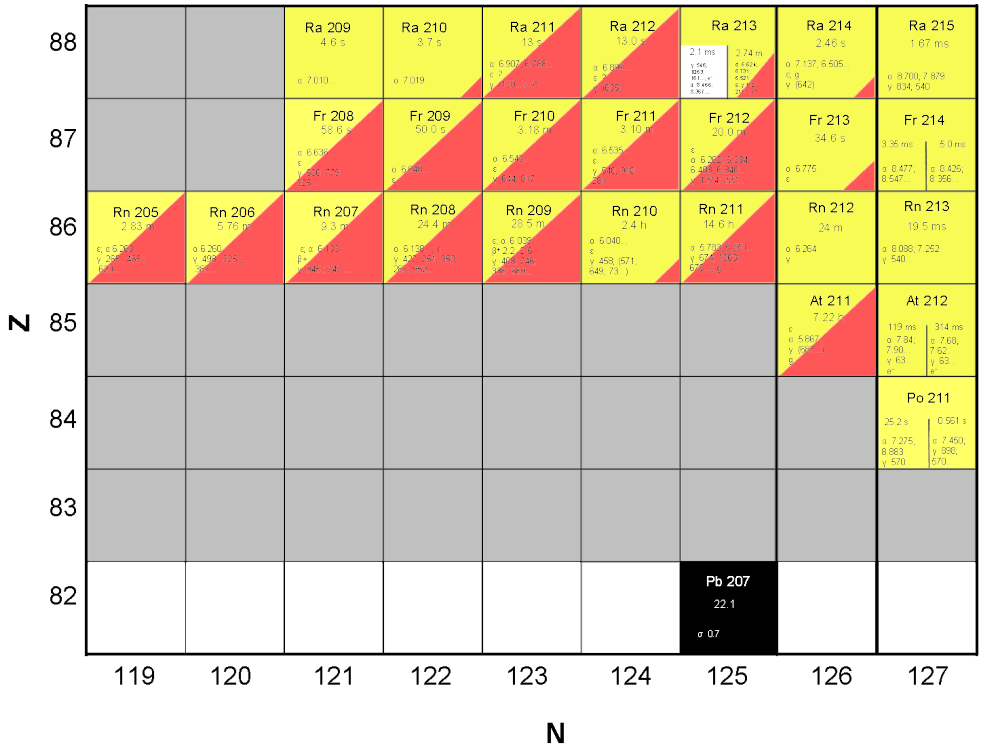

Figure 3.2: Region of the nuclear chart populated by transfers in ^{58}Ni + ^{207}Pb collisions.

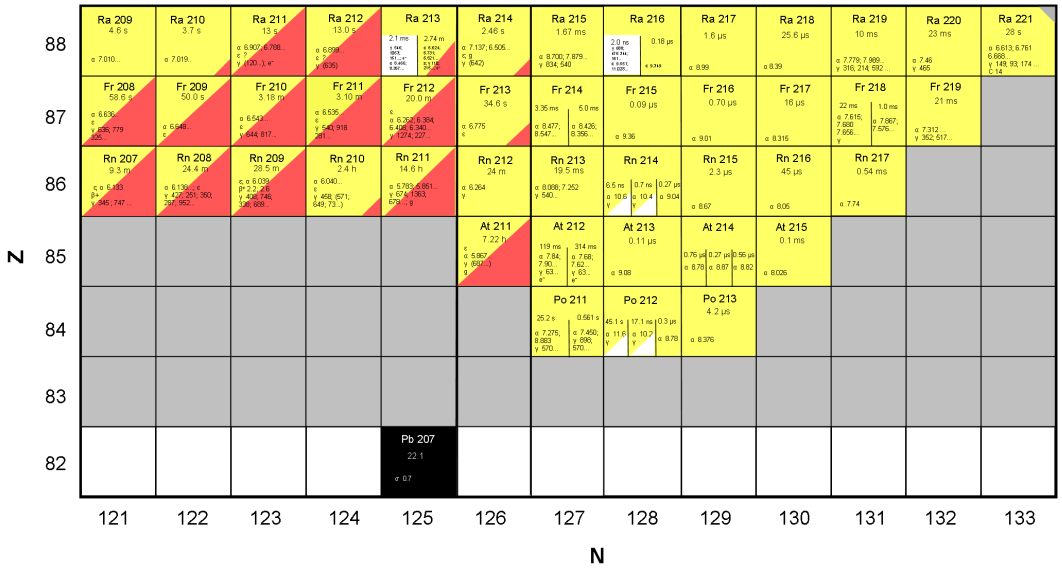

Figure 3.3: Region of the nuclear chart populated by transfers in ^{64}Ni + ^{207}Pb collisions.

^{221}Ra was also identified applying the α-α correlation method. In this case the decay chain is:

$$^{221}Ra(28\ s, 6581, 6591, 6613, 6668, 6761 keV) \rightarrow\ ^{217}Rn(0.54\ ms, 7741\ keV) \rightarrow\ ^{213}Po(4.2\ \mu s, 8376\ keV) \tag{3.2}$$

The α-decay granddaughter, ^{213}Po, has a half-life of 4.2 μs and approximately the half of the decays resulting from this activity will occur after the coincidence time and will not be recorded. In this sense one can search for α-α correlations with no pile-up occurring for the second *alpha*.

In the case of ^{219}Fr the decay chain is:

$$^{219}Fr(20\ ms, 7312\ keV) \rightarrow\ ^{215}At(0.1\ ms, 8026\ keV) \tag{3.3}$$

In this case, no pile-up occurs after the first α-decay. A clean α-α correlation spectrum is obtained. Fig 3.5 (a) shows the correlated events in the ^{64}Ni reactions, where the x-axis and y-axis represent the mother and daughter α-energies, respectively, for a correlation time of 0.5 ms corresponding to five times the half-live of ^{215}At. The one-dimensional spectrum of correlated *alpha*s is shown in Fig 3.5 (b) where the two peaks corresponding to ^{219}Fr and ^{215}At can be identified. Random correlations are very

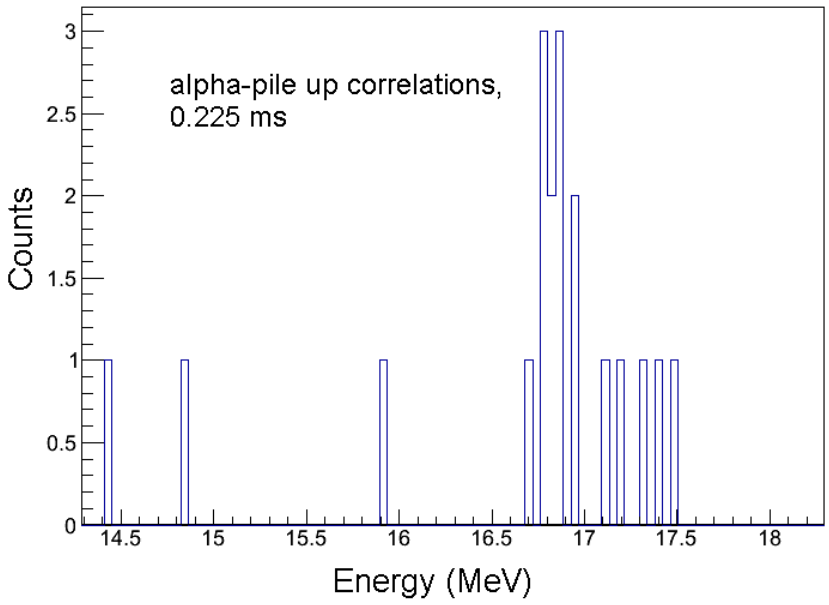

Figure 3.4: Measured number of correlations between an α-decay and a pile-up event within a time window of 0.225 ms from the decay chain of the isotope ^{220}Ra produced in the reaction ^{64}Ni + ^{207}Pb. The pile-up event results from the successive α-decays of ^{216}Rn and ^{212}Po. Details of the decay chain in 3.1.

unlikely to occur in such small correlation times. For example, a random correlation probability of P_{random}=7.6 10^{-6} can be estimated for α-α correlations of ^{219}Fr within 0.5 ms, and P_{random}=1 is obtained for correlation times of ∼1 min.

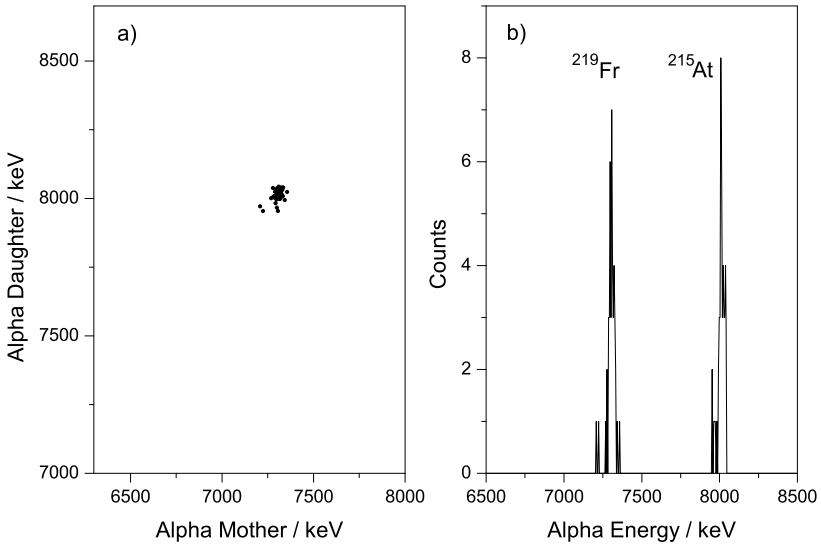

Figure 3.5: a)Measured number of α-α correlations from the decay chain of the isotope ^{219}Fr (decay chain 3.3) using ^{64}Ni beams. The x-axis represents the α-energy of the mother nucleus ^{219}Fr and the y-axis the ones of the daughter nucleus ^{215}At. b) Measured number of correlated alphas.

A search for recoil followed by α-α pile-ups was also performed to identify fast decaying isotopes like ^{218}Ra, ^{217}Fr, ^{216}Rn and ^{218}Fr. The decay chains are:

$$
\begin{aligned}
&Recoil \rightarrow {}^{218}Ra(25.6\ \mu s, 8390\ keV) \rightarrow {}^{214}Rn(0.27\ \mu s, 9037\ keV)\ \ E_{\alpha_1+\alpha_2} = 17.4\ MeV \\
&Recoil \rightarrow {}^{217}Fr(16\ \mu s, 8315\ keV) \rightarrow {}^{213}At(0.11\ \mu s, 9080\ keV)\ \ E_{\alpha_1+\alpha_2} = 17.4\ MeV \\
&Recoil \rightarrow {}^{216}Rn(45\ \mu s, 8050\ keV) \rightarrow {}^{212}Po(0.30\ \mu s, 8785\ keV)\ \ E_{\alpha_1+\alpha_2} = 16.8\ MeV \\
&Recoil \rightarrow {}^{218}Fr(1\ ms, 7866\ keV) \rightarrow {}^{214}At(0.56\ \mu s, 8819\ keV)\ \ E_{\alpha_1+\alpha_2} = 16.8\ MeV
\end{aligned}
\tag{3.4}
$$

After the implantation signal of the recoil, a pile-up event is generated in each of the four cases. Fig 3.6 shows the number of pile-ups in the energy range of 12-20 MeV correlated with a recoil signal within a correlation time of 0.125 ms for the complete ^{64}Ni run. Two peaks are visible at 16.7 MeV and 17.4 MeV. The 17.4 MeV peak

has contributions from pile-ups of ^{217}Fr + ^{213}At and ^{218}Ra + ^{214}Rn. The comparable half-lives of $T_{1/2}(^{217}\text{Fr})$=16 μs and $T_{1/2}(^{218}\text{Ra})$=25.6 μs make the separation of the different contributions impossible. The peak located at 16.7 MeV is produced from pile-ups of ^{216}Rn + ^{212}Po and ^{218}Fr + ^{214}At.

The difference in the half-lives of ^{216}Rn and ^{218}Fr can be used to distinguish the correlated events coming from these two isotopes. It is possible to search the correlated events with t_1 >0.225 ms ($5\times T_{1/2}(^{216}\text{Rn})$) where almost no contribution is expected to be produced from ^{216}Rn isotopes and the events can be attributed to ^{218}Fr. Then, correlation times of t_2 <0.225 ms can be considered, where the contribution of ^{218}Fr can be subtracted and the resulting events can be attributed to ^{216}Rn.

The same correlation searches were applied for the data from ^{58}Ni reactions but no decays of isotopes with N>127 were found.

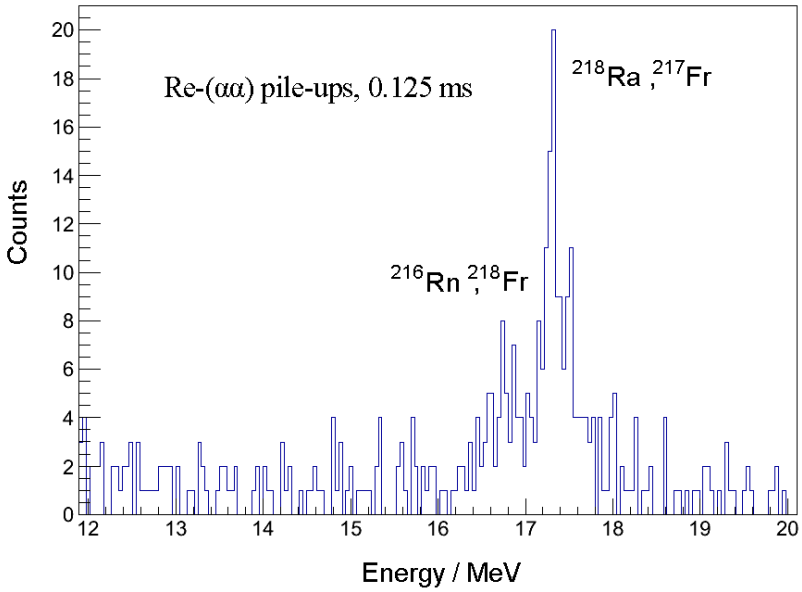

Figure 3.6: Number of Recoil-($\alpha\alpha$) pile-up correlations from the decay chain 3.4 measured in the reaction ^{64}Ni + ^{207}Pb.

We also explored if the region of Z>88 was populated in the reactions. Specifically the Ac isotopes which correspond to a transfer of seven protons from the projectile to the target. In the reactions with ^{58}Ni an α-line of 7600 keV was observed which was not present in the ^{64}Ni reactions. The line corresponds to the expected α-energy of ^{215}Ac but contributions can also come from α-decays of ^{212}At.

In the ^{64}Ni reactions, an indication of the decay of ^{221}Ac was found applying the α pile-up correlation method. Fig 3.7 shows the α-decays of the two most intense components of ^{221}Ac located at 7440 keV (20%) and 7646 keV (70%) correlated with a pile-up event of 17.3 MeV within 80 μs of correlation time. A third α-line of ^{221}Ac of 7375 keV (10%) is not visible in the spectrum and the reason is that the level which is populated in ^{217}Fr after the decay is highly converted. The electrons emitted in the conversion process add up with the α-energies resulting in approximately 7440 keV, overlapping with the corresponding α-line. Other neutron-rich Ac isotopes close to A=221 could not be properly separated mainly due to very small half-lives on the order of microbarns and nanobarns. More neutron-deficient Ac isotopes have α-lines which overlap with other α-decays and the correlation method can not be applied in these cases due to very long half-lives on the order of several minutes.

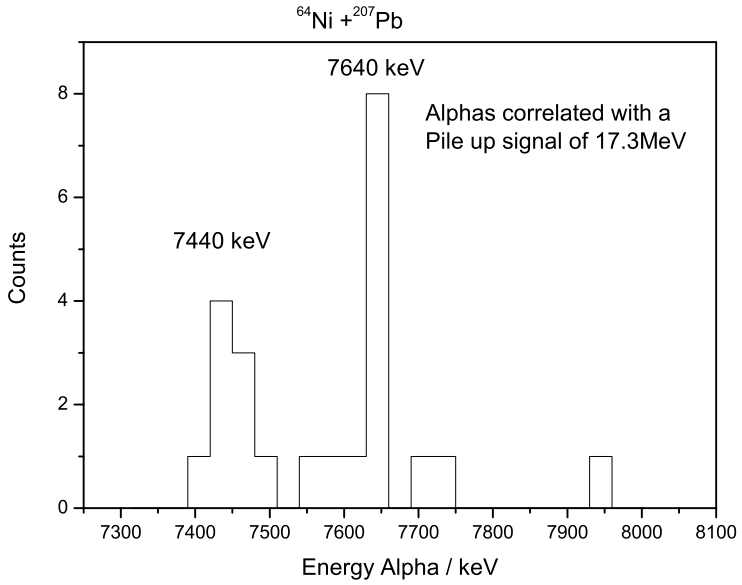

Figure 3.7: Measured number of α-decays from the isotope ^{221}Ac correlated with an α-α pile-up event of 17.3 MeV within 80 μs in the reaction ^{64}Ni + ^{207}Pb.

3.2 Velocity Distributions

Velocity distributions were measured for the different beam energies in the reaction ^{64}Ni + ^{207}Pb. As an example, Fig 3.8 shows the velocity distributions of the isotopes

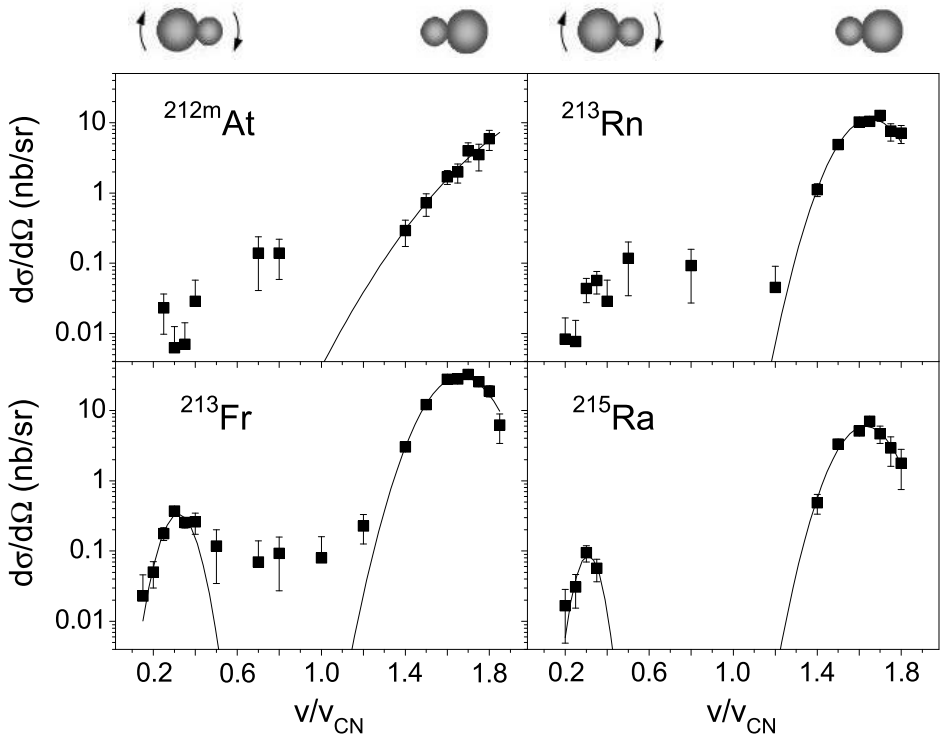

Figure 3.8: Measured velocity distributions of the isotopes ^{212m}At, ^{213}Rn, ^{213}Fr and ^{215}Ra produced in the reaction ^{64}Ni + ^{207}Pb at the beam energy 5.92×A MeV. The velocity acceptance of SHIP for each velocity setting is Δv/v=$\pm$5%. Gaussian fits are shown in every case.

Isotope	Velocity peak (^{58}Ni)	Velocity peak (^{64}Ni)
Po	1.95	1.85
At	1.89	1.78
Rn	–	1.65
Fr	1.75	1.67
Ra	1.73	1.63

Table 3.1: Position of the maxima of the high-velocity component for the isotopes Po, At, Rn, Fr and Ra for the two reactions with ^{58}Ni (5.0×A MeV) and ^{64}Ni (5.92×A MeV). The velocities are in units of v_{CN}.

^{212m}At, ^{213}Rn, ^{213}Fr and ^{215}Ra produced at the beam energy of 5.92×A MeV. For other beam energies, the velocity spectra presented the same general characteristics. The distributions show two symmetric components which were previously discussed in Chapter 2, Fig 2.12. The intensities of the high and low velocity peaks can be directly compared taking into account the differences in the angular distributions and particle losses mainly due to scattering in the target material. This effect has a larger impact on the particles with low velocities resulting in broader angular distributions and larger particle losses. After correction for these effects the peak intensities still differ by a factor of approximately 10 which indicates that the observed products are not produced in an isotropic process like the CN decay. The contribution of fusion-fission decays can be neglected which is going to be analyzed in more details in the Chapter 4. Therefore, the nuclei are produced in transfer reactions, where the high velocity components result from re-separations in central collisions and the low-velocity peaks from rotations of the DNS by approximately 180°. The positions of the maxima of the velocity distributions are shown (high velocity peak) in Table 3.1, third column. The positions do not depend on the neutron numbers of the produced isotopes. A shift to smaller values is seen for increasing proton number of the transfer product. The shifts can be explained as differences in the Coulomb barriers in the exit channel which increases for more symmetric reaction products. The low velocity component has smaller production cross-sections for less number of transferred protons. In general, the production cross-sections of the low velocity components decrease for decreasing beam energy mainly due to increasing dispersion inside the target.

A similar behavior was observed in the velocity distributions in the ^{58}Ni + ^{207}Pb reactions which were measured at 5.0×A MeV. For higher beam energies the velocity distributions were not fully scanned (Table 2.1). Fig 3.9 shows the velocity distributions of ^{212}At, ^{213}Rn, ^{213}Fr and ^{213}Ra. The arrows represent the measured one event cross-section limits. The positions of the maxima of the high velocity components of the

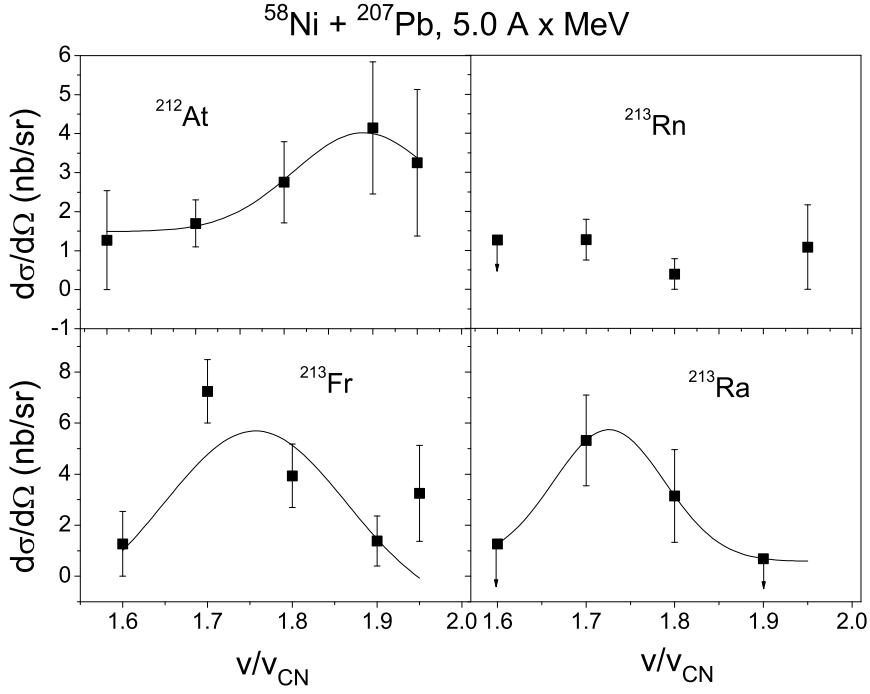

Figure 3.9: Velocity distributions of the isotopes ^{212m}At, ^{213}Rn, ^{213}Fr and ^{215}Ra produced in the reaction ^{58}Ni + ^{207}Pb at the beam energy 5.0×A MeV.

isotopes ^{213}Rn, ^{213}Fr, ^{213}Ra, ^{212}At and ^{211}Po are also dependent on the proton number of the transfer product as in the case of ^{64}Ni reactions (Table 3.1 (second column)). The Rn peak position was not included due to low statistics.

The localization of the maxima of the high velocity components in the velocity distributions was done for all beam energies. Table 3.1 gives as example, the position of the maxima in the cases of the beam energies discussed above. The same general trends were found for all beam energies.

3.3 Total Kinetic Energies

The velocity distributions can be used to estimate the total kinetic energies (TKE) in the center of mass system in the exit channel and, in this sense, obtain information on the energy dissipation in the reaction. Particularly, the locations of the maxima of the velocity spectra are used to estimate the kinetic energies of the target-like products. Considering the separation of the DNS as a two-body process, as it was discussed in Chapter 1.2, and the energy and momentum conservation laws, it is possible to reconstruct the kinetic energy of the respective projectile-like reaction partners in the center of mass system and the TKE.

$$TKE = E_3(CM) + E_4(CM) \tag{3.5}$$

where $E_3(CM)$ and $E_4(CM)$ are the kinetic energies of the two reaction products in the center of mass system.

Fig 3.10 shows the measured TKE values for the isotopes ^{211}Po, ^{212}At, ^{213}Rn and ^{215}Ra in the reactions with ^{58}Ni and ^{64}Ni beams at different beam energies. Particularly in the case of ^{58}Ni reactions, only the beam energy 5.0×A MeV was used in the TKE plot where the velocity distributions were fully measured. The TKE values expected from the fission decay of a completely equilibrated system have been calculated by applying the Viola systematic [61] (represented by crosses). The open circles correspond to the calculated TKE resulting from elastic reactions. In the case of ^{64}Ni (black open circles), the calculation was done for the beam energy 4.8×A MeV as a reference. The measured TKE values are independent of the beam energy. In general, the TKE values are close to the Viola systematics and considerable energy is lost in the reactions in the range of 60 to 100 MeV, indicating that the detected isotopes were produced in deep inelastic reactions with full kinetic energy dissipation.

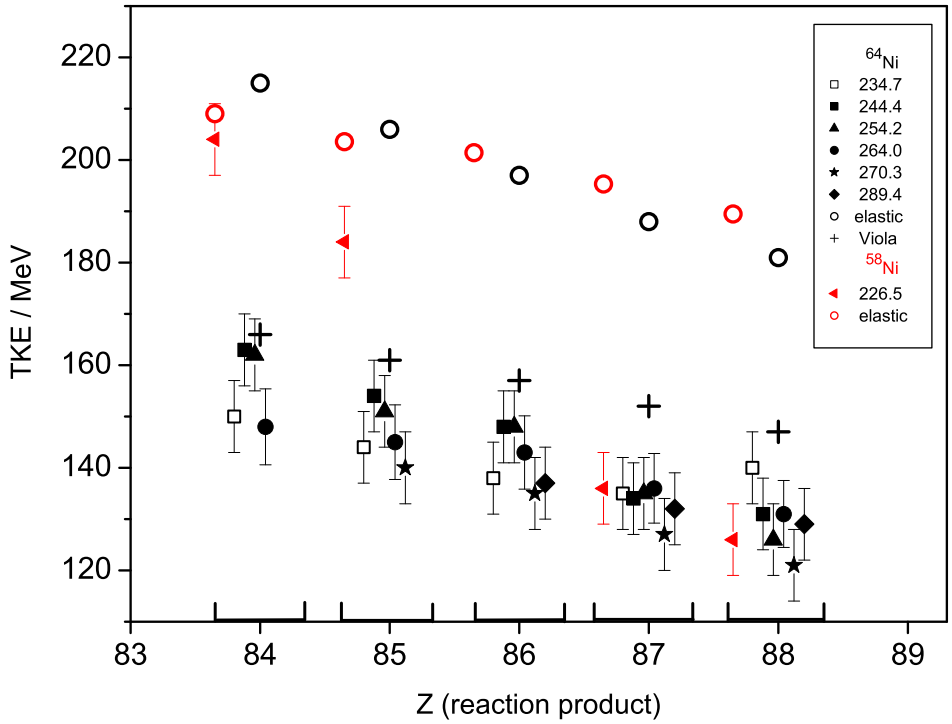

Figure 3.10: Measured TKE values as a function of the proton number Z of the produced isotopes in the reactions with ^{58}Ni beams represented by red symbols and ^{64}Ni beams (black symbols). The respective beam energies in the center of mass system are given in the inset. A small offset in the Z values has been introduced for better discrimination of the experimental points for the same Z. The crosses represent the Viola energies. As an example the open circles represent the TKE values expected from elastic kinematics at 5.0×A MeV for ^{58}Ni and 4.8×A MeV for ^{64}Ni.

A pronounced difference is visible between ^{58}Ni and ^{64}Ni reactions concerning the TKE values which correspond to the production of Po and At. In the case of ^{64}Ni reactions, they are produced in deep inelastic reactions with an energy dissipation of 50-60 MeV for the lowest beam energies. For ^{58}Ni reactions at 5.0×A MeV, the dissipated energy for Po and At are: <10 and 20 MeV, respectively, which correspond to a quasi-elastic process.

In general, the measured TKE values correspond to re-separations with the Coulomb barrier energy in the exit channel of a very elongated DNS. Separations of ∼20 fm of the nuclear centers can be estimated considering the Coulomb barrier of spherical nuclei in the exit channel. This points to strong deformations of the nuclei before re-separation. A quadrupole deformation of β_2=0.4 can be estimated for both, target-like and beam-like, nuclei before scission takes place considering that both fragments have the same quadrupole deformation.

For a direct comparison between ^{58}Ni and ^{64}Ni reactions, the cross-sections for different isotopes can be also plotted as a function of the overlap parameter d_0:

$$d_0 = R_{min}/(A_1^{1/3} + A_2^{1/3}) \tag{3.6}$$

where A_1 and A_2 are the mass numbers of the projectile and target nuclei and R_{min} is defined as:

$$R_{min} = \frac{Z_1 Z_2 e^2}{2E_{CM}} \left(1 + \frac{1}{sin(\theta/2)}\right) \tag{3.7}$$

where Z_1 and Z_2 are the proton numbers of the projectile and target nuclei, θ is the scattering angle in the center of mass system and E_{CM} is the beam energy in the center of mass system.

The d_0 parameter characterizes the overlap of the nuclear matter between the projectile and target. Quasi-elastic reactions take place mainly at relatively large values of the overlap parameter ($d_0 > 1.45$ fm) as it was discussed in [62] and deep inelastic reactions seem to be already influencing at values of d_0=1.45 fm. In our experiments, only scattering angles which are accepted by SHIP are considered (θ =180°). Having fixed the scattering angle, the overlap parameters are only a function of the beam energy.

Fig 3.11 shows the cross-sections for the isotopes ^{211}Po, ^{212}At, ^{213}Rn, ^{213}Fr and ^{213}Ra as a function of d_0. In general, the maxima of the production cross-sections are reached for higher d_0 values in ^{58}Ni reactions. The maxima of the distributions shift to larger overlap parameters for a smaller number of transferred protons. In Fig 3.11 (a) the production cross-sections of the isotopes ^{213}Fr and ^{213}Ra are plotted for the two

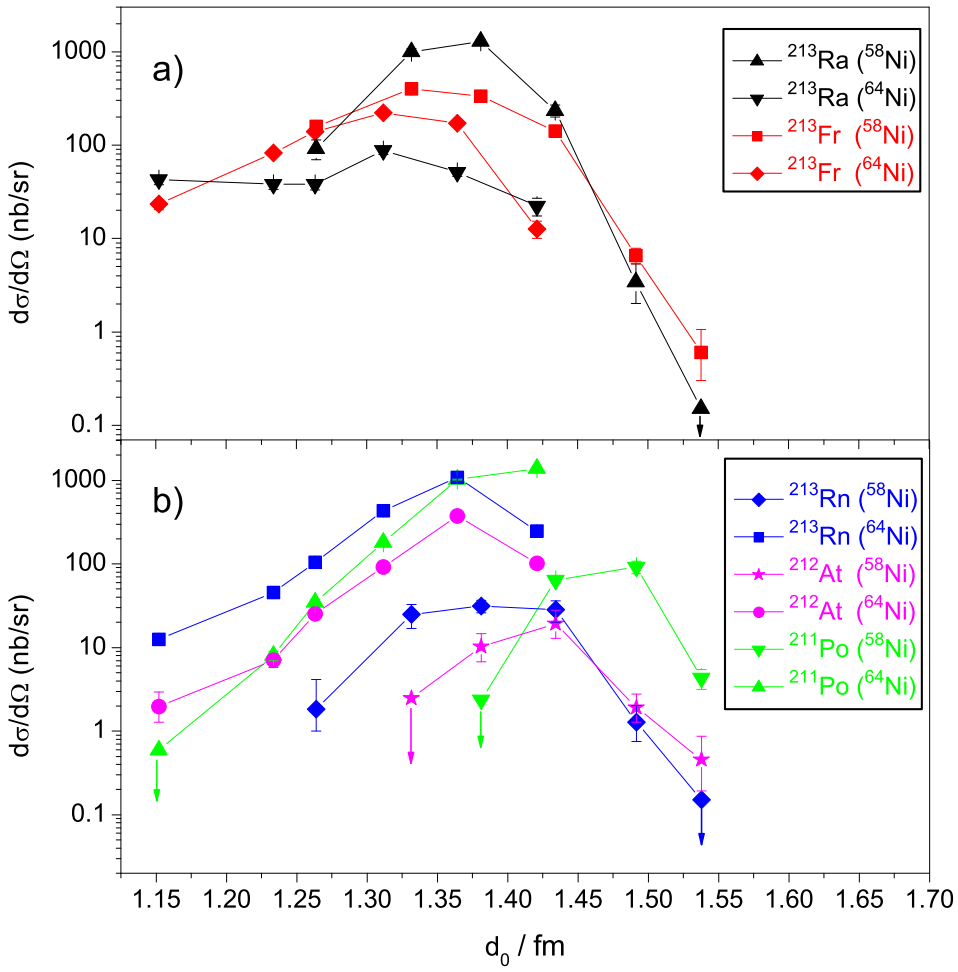

Figure 3.11: Measured production cross-sections of the isotopes ^{213}Fr, ^{213}Ra (a) and ^{211}Po, ^{212}At, ^{213}Rn (b) as a function of the overlap parameter d_0 (in fm) for both beams ^{58}Ni and ^{64}Ni.

different beams ^{58}Ni and ^{64}Ni. For both isotopes, the maximum of the cross-section is reached at relatively close values of d_0 ≈1.35 fm for the two different beams. These values correspond to strong overlap between the projectile and target nuclei and deep inelastic reaction components are predominant.

The same plots for the isotopes ^{211}Po (green), ^{212}At (magenta) and ^{213}Rn (blue) are shown in Fig 3.11 (b). Larger d_0 values are obtained for ^{212}At (∼1.43 fm) and ^{211}Po (∼1.47 fm) using ^{58}Ni beams compared to the ^{64}Ni reactions, where d_0 values of ∼1.36 fm (^{212}At) and ∼1.40 fm (^{211}Po) were measured. The d_0 values for ^{58}Ni beams correspond to the overlap region where the quasi-elastic reaction component is expected to appear.

One can conclude that the results of the d_0 analysis are in agreement with the measured TKE values of the produced isotopes. In general, stronger overlap between the projectile and target nuclei occurs in ^{64}Ni reactions.

3.4 Isotopic Distributions

In this section the characteristics of the isotopic distributions are presented for both reactions, their beam energy dependence and the excitation functions.

Fig 3.12 (a,b) shows the isotopic distributions of the isotopes of Rn, Fr and Ra for both reactions. The beam energies were selected close to the barrier, 5.4×A MeV (^{58}Ni) and 5.2×A MeV (^{64}Ni). It can be noticed that, in general, higher cross-sections were measured for the reactions using ^{58}Ni beams compared to the ^{64}Ni case. More neutron deficient isotopes were produced in the ^{58}Ni reactions with a steep drop at N≥127. In the case of the ^{64}Ni reactions, more neutron rich isotopes were produced reaching neutron numbers N=132,133. These general trends were also observed at the other beam energies. In Fig 3.12 (c), (d) the Q-values for the transfer reactions leading to different isotopes of Rn, Fr and Ra are shown. The Q-values are defined as:

$$Q = [(m_1 + m_2) - (m_3 + m_4)]\, c^2 \tag{3.8}$$

where m_1 and m_2 are the ground states masses of the projectile and target nuclei, m_3 and m_4 are the ground states masses of the projectile-like and target-like reaction products, c is the speed of light.

The Q-values are more negative (by 15-20 MeV) for the isotopes produced with ^{64}Ni beams compared to ^{58}Ni reactions. A decrease in the Q-value for ^{58}Ni beams occurs

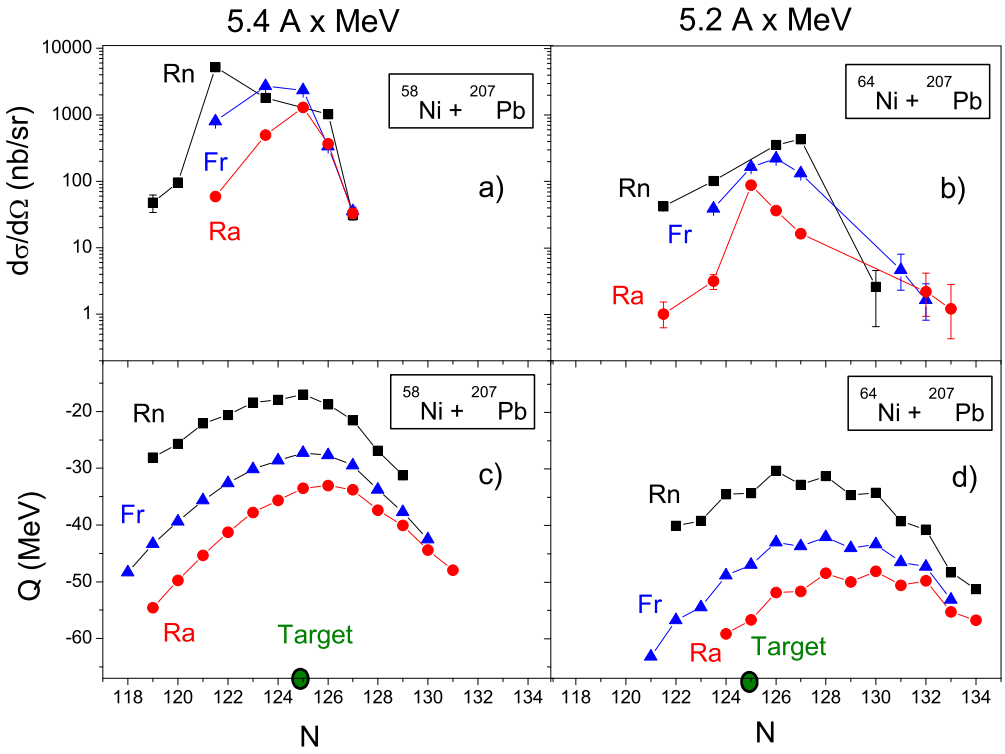

Figure 3.12: (a,b): Measured production cross-sections of the isotopes of Rn, Fr and Ra as a function of the neutron number N for the reactions with ^{58}Ni and ^{64}Ni beams at the beam energies 5.4×A MeV and 5.2×A MeV, respectively. Figure c) and d) show the Q-value distributions for both reactions calculated using the mass tables of Audi and Wapstra [63].

for N>126 while a flatter behavior as a function of N towards the neutron rich side can be seen for ^{64}Ni beams.

In general, one can expect that the primary distributions follow the Q-value distributions, the location of the maxima of the measured isotopic distributions reflects the characteristics of the evaporation process and the excitation energy of the primary isotopes produced in the reactions. For both beams the maxima of the measured isotopic distributions are shifted to lower neutron numbers with respect to the maxima of the Q-value distributions. In the case of ^{64}Ni reactions this difference, ΔN, is larger than for ^{58}Ni and ΔN increases with increasing proton number of the transfer products with values of ΔN=0,2,5 for Rn, Fr and Ra isotopes, respectively, which would correspond to excitation energies of the primary reaction products of approximately <10, 20 and 50 MeV. Nevertheless, in the isotopic distributions for each element, isotopes which correspond to evaporations of up to 7 neutrons (from the maxima of the Q-value distribution) were detected, indicating that excitation energies of $\sim$ 70 MeV are reached.

In the case of ^{58}Ni beams, ΔN is nearly independent of the proton number of the transfer products. For example, for the beam energy 5.0×A MeV, ΔN=1 for Rn, Fr, and Ra and isotopes which correspond to evaporations up to 4 neutrons were detected.

In the following sections, a more detailed description of the isotopic distributions is provided for each reaction.

3.4.1 Isotopic Distributions in ^{64}Ni Reactions

Fig 3.13, (a) shows the cross-sections of the isotopes of Rn produced in transfer reactions for different beam energies using ^{64}Ni beams. The arrows indicate a one event cross-section limit. The contributions of the isotopes ^{207}Rn and ^{208}Rn could not be separated, mainly because of the similar α-decay characteristics; the same occurs for ^{209}Rn and ^{210}Rn. In the following for such cases, the production cross-sections of the isotopes are summed and divided by a factor of 2. As it can be seen, for increasing beam energy the maxima of the distributions move to more neutron deficient isotopes. The isotopic distributions are strongly dependent on the beam energy.

The same analysis can be done for Fr isotopes. Fig 3.13, (b) represents the isotopic distributions for different beam energies. The contributions of the α-decays of ^{208}Fr and ^{209}Fr could not be resolved as in the case of ^{210}Fr and ^{211}Fr. In these cases, the convention described before for the Rn isotopes was used. The distributions also shift

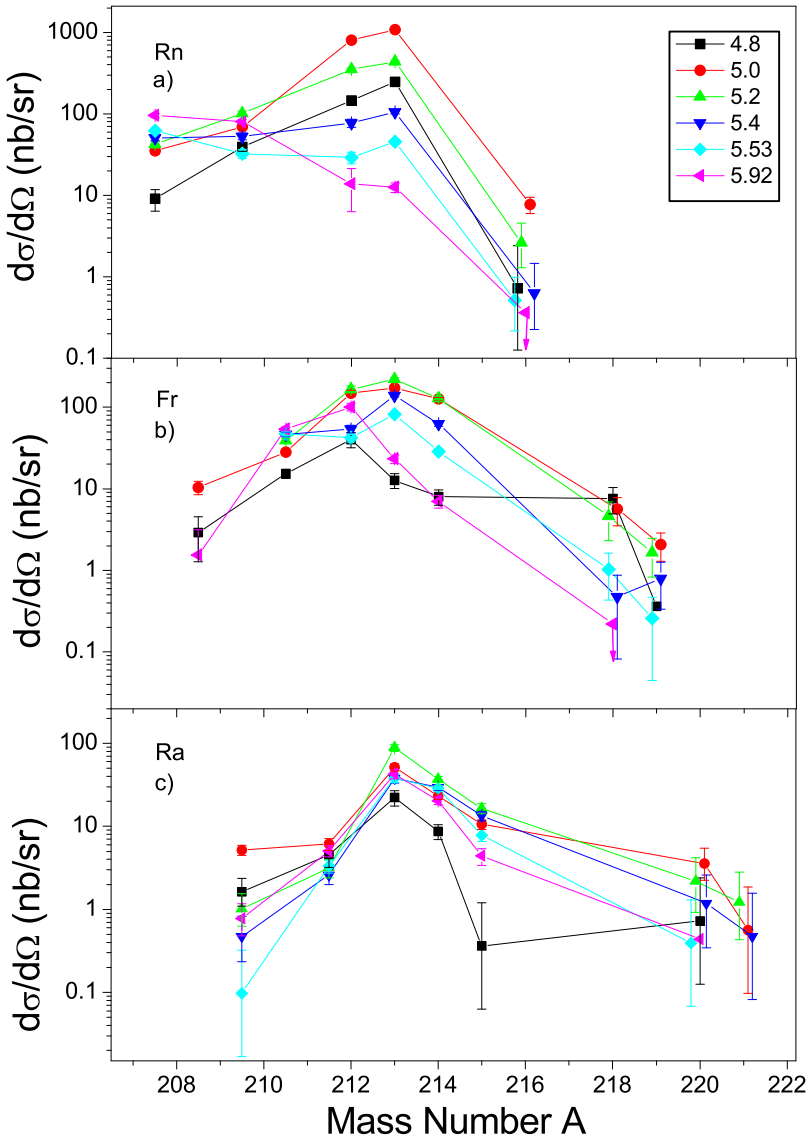

Figure 3.13: Measured production cross-section of Rn (a), Fr (b) and Ra (c) isotopes as a function of the mass number for different beam energies (given in the legend in A MeV) in the reaction ^{64}Ni + ^{207}Pb. A small offset was introduced for A=216, 218, 219 for a better visualization of the points and error bars.

to more neutron deficient isotopes for increasing beam energy but in a less pronounced way as in the case of the Rn isotopes. The shift is better noticeable for the higher beam energy of 5.92×A MeV where the maximum is located three neutrons (ΔN=3) more to the neutron deficient side as compared with the maxima of the Q-value distribution. For lower beam energies the maxima are located at ΔN=2 with respect to the Q-value maximum. In the case of the more neutron rich Fr isotopes the production cross-sections decrease for increasing beam energy.

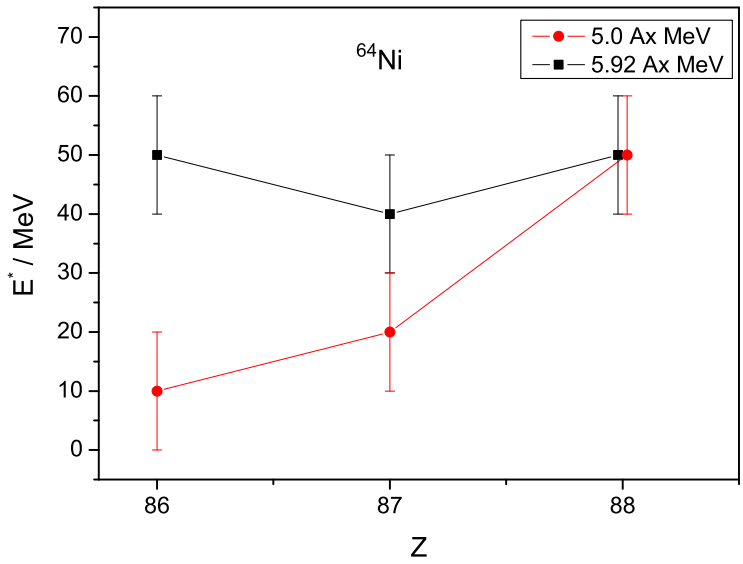

Figure 3.14: Excitation energies extracted from the number of evaporated neutrons (ΔN) as a function of the proton number Z of the target-like products in the reactions using ^{64}Ni beams at two beam energies 5.0 and 5.92×A MeV. ΔN corresponds to the shift between measured isotopic distributions and Q-value distributions.

Fig 3.13, (c) shows the isotopic distributions of the Ra isotopes for different beam energies. The contributions of the α-decays of the isotopes ^{209}Ra and ^{210}Ra could not be separated as in the case of ^{210}Ra and ^{211}Ra. The same convention was used as before for Rn and Fr isotopes. The isotopic distributions show a very similar behavior for all beam energies with all maxima located at the same mass number A=213 which is five neutrons less than the maximum of the Q-value distribution (Fig 3.12, c) located at A=218. Only the production cross-sections of the neutron rich isotopes with A=220 and A=221 are dependent on the beam energy, with increasing cross-sections for decreasing beam energy. For example, in the case of ^{220}Ra, the production cross-section drops

approximately one order of magnitude from 5.0×A MeV to 5.53×A MeV.

In general, the isotopic distributions broaden towards the neutron rich side with increasing number of transferred protons. This broadening can be explained from the Q-value distributions (Fig 3.12, c) which are flatter towards the neutron rich side for increasing proton number of the reaction products.

The excitation energies of the primary target-like products can be estimated from the number of evaporated neutrons as it was described in the previous section. An average excitation energy was determined comparing the neutron number where the maximum of the Q-value distribution is located with the neutron number where the maximum of the measured isotopic distribution is located (ΔN). For the evaporation of one neutron about 10 MeV excitation energy is needed which is given by the neutron separation energy (7-8 MeV) and by the kinetic energy of the neutron (1.7 MeV). Fig 3.14 shows the resulting average excitation energies for the transfer products of Rn, Fr and Ra for a beam energy located close to the barrier (5.0×A MeV) and another beam energy which is ∼20% above the barrier (5.92×A MeV). For the error bars an uncertainty of ± 10 MeV was assumed. For the beam energy close to the barrier the excitation energy is increasing with increasing number of transferred protons with the Rn isotopes being produced at a very low excitation energy ∼ 10 MeV. For the higher beam energy this dependence disappears.

In another approach, the excitation energies of the primary transfer products were estimated from the measured TKE and the reaction Q-value as:

$$E^* = E_{cm} - TKE + Q \tag{3.9}$$

where E^* is the total excitation energy of the DNS and E_{cm} is the incident energy in the center of mass system.

The total excitation energies estimated using the measured TKE did not differ considerably for different number of transferred protons in the cases of Rn, Fr and Ra for a certain beam energy. Values of E^*∼60 and 110 MeV could be extracted for the beam energies 5.0 and 5.92×A MeV, respectively.

In the case when thermodynamical equilibrium is reached in the system, the total excitation energy is expected to be divided between the reaction products according to the level densities [64] as:

$$E_3^*/E_4^* = a_3/a_4.$$

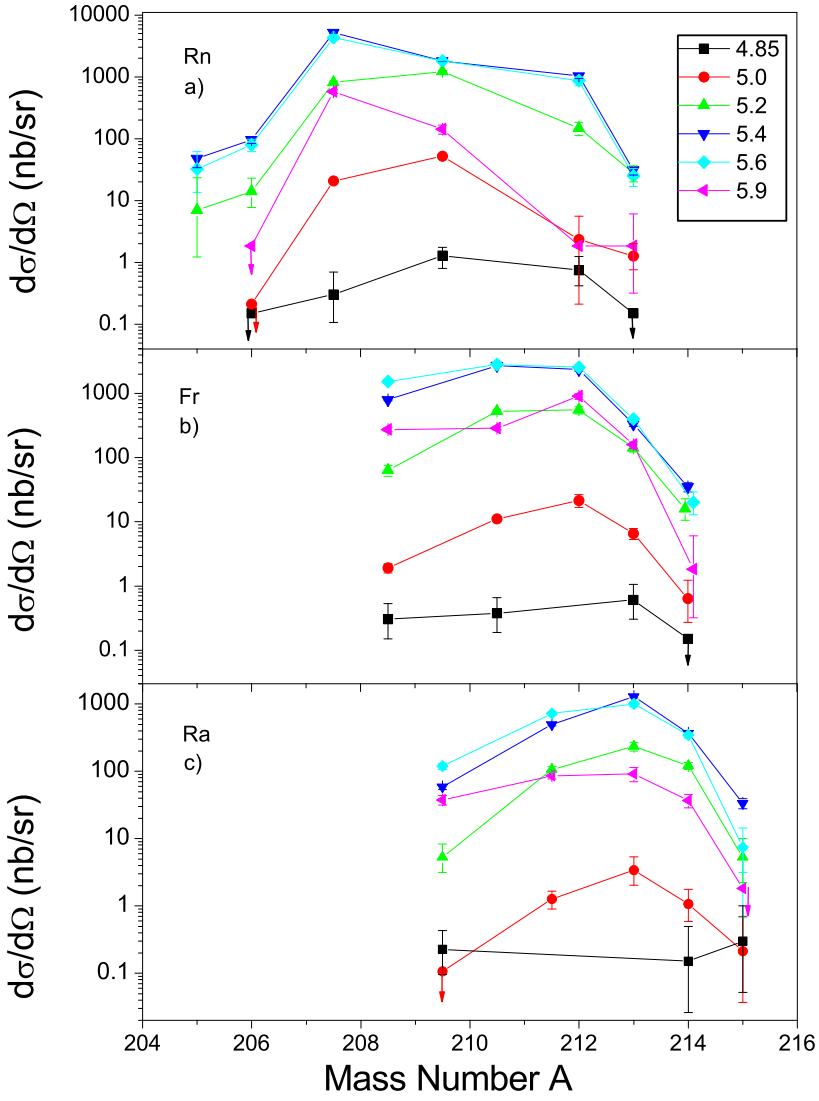

Figure 3.15: Measured production cross-section of Rn (a), Fr (b), Ra (c) isotopes as a function of the mass number for different beam energies in the reaction ^{58}Ni + ^{207}Pb. The arrows indicate one-event cross-section limits.

where a_3, a_4, E^*_3 and E^*_4 are the level density parameters and the excitation energies of the light and heavy fragment, respectively, where $E^* = E^*_3 + E^*_4$. In the cases where thermodynamical equilibrium is not yet reached, equipartition of the total excitation energy between the projectile-like and target-like products can be expected.

The values of the level density parameters are strongly influenced by the shell effects as it can be qualitatively followed in [65]. The effects are better noticeable for small excitation energies. The shell effects result in much smaller level density parameter values and consequently smaller excitation energies. The primary products of Rn and Fr are created closer to the closed neutron shell at N=126 as compared to the case of Ra isotopes, where the maximum of the Q-value distribution is located at N∼130. In the case of ^{64}Ni reactions at low beam energies close to the barrier like 5.0×A MeV, the influence of shell effects results in less excitation energy for the Rn and Fr isotopes than in the case of Ra isotopes, as was also concluded from the number of evaporated neutrons. The influence of the shell effects is less pronounced for increasing total excitation energy as in the case of the beam energy 5.92×A MeV, resulting in almost the same excitation energies for Rn, Fr, and Ra isotopes (Fig 3.14, red curve) with values (E^*_4∼50-60 MeV) close to the ones expected from equipartition of the total excitation energy E^*∼110 MeV. The equipartition of the excitation energy can be expected when thermal equilibrium is not yet established before the re-separation of the DNS occurs.

3.4.2 Isotopic Distributions in ^{58}Ni Reactions

Isotopic distributions were also measured for ^{58}Ni beams. Fig 3.15, (a) shows the distributions of Rn isotopes for different beam energies. It is important to stress that the Coulomb barrier for this reaction is at ∼ 5.4× A MeV which means that the beam energies of 4.85, 5.0 and 5.2×A MeV are all located below the barrier. Generally, the isotopic distributions are shifted to more neutron deficient isotopes as compared with the same distributions using ^{64}Ni beams. The maximum cross-sections are located close to the Coulomb barrier. Below the barrier, the cross-sections decrease with decreasing beam energy due to a decrease of the nuclear overlap. At the higher beam energy (5.9×A MeV) the isotopic distributions show a shift to the more neutron deficient side with a steep decrease in the cross-sections of the isotopes with A=212, and A=213.

The same general behavior is observed for Fr (Fig 3.15, b) and for Ra (Fig 3.15, c) isotopes. Even in the case of energies well below the barrier, isotopes up to Ra were still produced. The distributions are less dependent on the beam energy than in the

case of Rn isotopes. Only at the higher beam energy (5.9×A MeV), the distributions show a noticeable shift to the more neutron deficient side.

The maxima of the measured isotopic distributions in ^{58}Ni reactions are generally closer to the corresponding Q-value maximum as in the case of ^{64}Ni reactions with ΔN=0 or 1 for Rn, Fr and Ra indicating very low excitation energies ≤ 10 MeV. In this case, the maxima of the Q-value distributions are located rather close to the closed shell N=126 for Rn, Fr and Ra leading to very small level density parameters and consequently to low excitation energies. However a total excitation energy of ∼60 MeV of the DNS can be extracted from the measured TKE for the beam energy 5.0×A MeV. This excitation energy is expected to go mainly to the projectile-like reaction product.

3.5 Excitation Functions

In this section, the excitation functions of some isotopes for both reactions are presented. The excitation functions of neutron-deficient, neutron-rich and intermediate isotopes are compared.

3.5.1 Excitation Functions in ^{64}Ni Reactions

Fig 3.16, (a) shows the excitation functions of the isotopes ^{207,208}Rn, ^{213}Rn and ^{216}Rn from reactions with ^{64}Ni beams. The more neutron rich isotopes ^{213}Rn and ^{216}Rn show a maximum in the excitation function at 5.0×A MeV which is close to the Coulomb barrier energy while in the case of the more neutron deficient ^{207,208}Rn isotopes the cross-section increases continuously with the beam energy as expected since more excitation energy of the primary products is required.

The same behavior is seen for Fr isotopes in Fig 3.16, (b). The cross-sections of the more neutron rich ^{218}Fr decreases for increasing beam energy while the more neutron deficient ^{210,211}Fr isotopes show the opposite trend with increasing cross-section for increasing beam energy. The isotope ^{213}Fr, which is located at the maximum of the isotopic distribution for almost all beam energies (Fig 3.13), has a maximum in the excitation function at 5.2×A MeV slightly above the Coulomb barrier but with a distribution which is much broader (FWHM=25 MeV) compared to the case of ^{213}Rn (FWHM=15 MeV).

In the case of Ra isotopes, the excitation functions are presented in Fig 3.16, (c). In this case the neutron deficient isotopes do not show increasing cross-sections for increas-

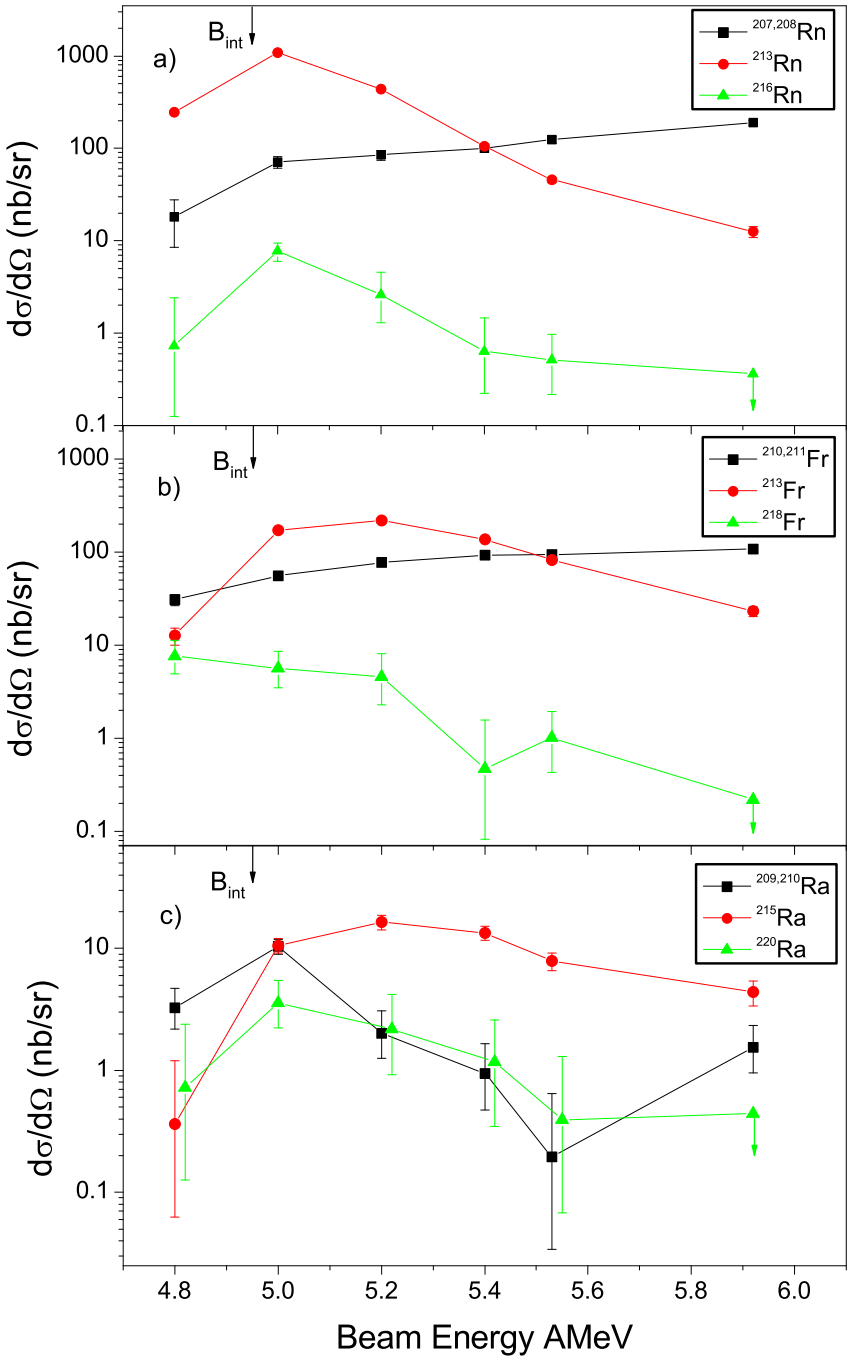

Figure 3.16: Measured excitation functions of the transfer products: a) ^{207,208}Rn, ^{213}Rn and ^{216}Rn; b) ^{210,211}Fr, ^{213}Fr and ^{218}Fr; c) ^{209,210}Ra, ^{215}Ra and ^{220}Ra. The isotopes were produced in the reaction ^{64}Ni + ^{207}Pb.

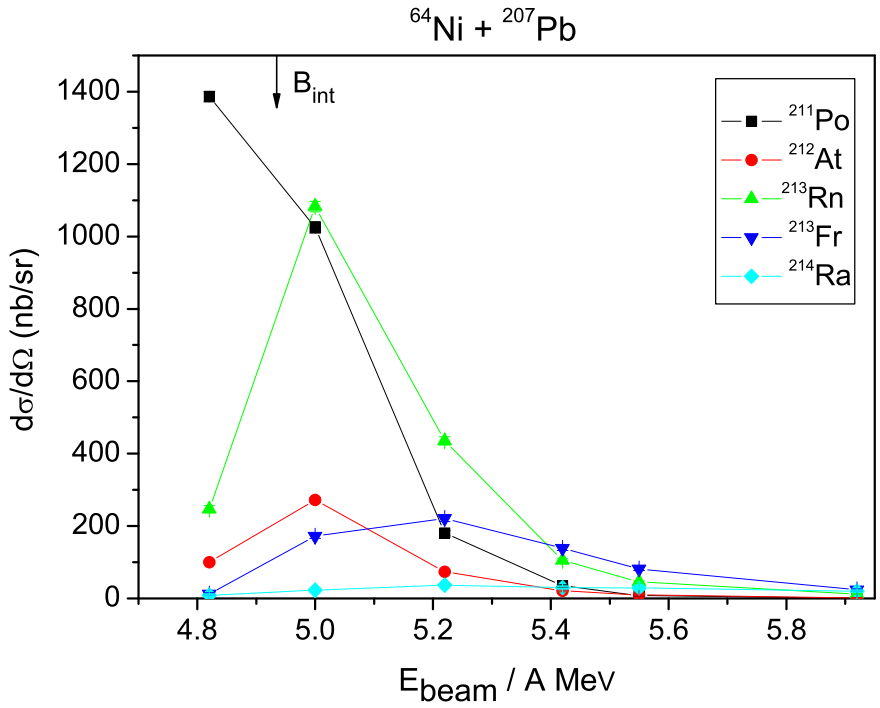

Figure 3.17: Measured excitation functions of the transfer products ^{211}Po, ^{212}At, ^{213}Rn, ^{213}Fr and ^{214}Ra produced in the reaction ^{64}Ni + ^{207}Pb.

ing beam energies like in the cases of Rn and Fr isotopes. Nevertheless, a broadening in the distribution of ^{215}Ra is seen compared with the ^{220}Ra and ^{209,210}Ra cases. The cross-section of the more neutron rich ^{220}Ra isotope drops faster for increasing beam energy in comparison to the rest of the isotopes. The isotope ^{215}Ra is located closer to the maximum of the isotopic distributions, and a value of FWHM=42 MeV can be extracted from the excitation function.

Fig 3.17 shows the excitation functions of ^{211}Po, ^{212}At, ^{213}Rn, ^{213}Fr and ^{214}Ra. These isotopes were selected because they are close to the maximum cross-section of the corresponding isotopic distribution. The location of the maxima of the excitation functions shifts to higher energies for increasing number of transferred protons. A continuous broadening of the excitation functions is seen for increasing proton number of the transfer product, FWHM=15 MeV (Z=85 and 86), FWHM=25 MeV (Z=87) and FWHM=42 MeV (Z=88). The broadening was explained in [66] as a result of the increasing excitation energy of the primary products for increasing number of transferred protons. The maxima of the Q-value distributions for Ra and Fr isotopes are located at A=216 and A=218, respectively, and the detected isotopes result after the evaporation of 3 to 4 neutrons. In the case of Po, At and Rn the maxima of the Q-value distributions coincide with the detected isotopes, which is an indication of the smaller number of evaporated neutrons and less excitation energy of the primary products. The higher excitation energy in the case of ^{213}Fr and ^{214}Ra is consistent with the shift of the excitation function maxima to higher beam energies and also results in broader distributions.

3.5.2 Excitation Functions in ^{58}Ni Reactions

The excitation functions for different isotopes were also studied in the reactions using ^{58}Ni beams. As examples, the excitation functions of ^{207,208}Rn and ^{213}Rn are shown in Fig 3.18, (a). The differences in the excitation functions for these isotopes are less pronounced than in the case of ^{64}Ni beams. The same occurs for the excitation functions of Fr and Ra isotopes presented in Fig 3.18, (b) and Fig 3.18, (c), respectively. It can be noticed that the production cross-sections of the more neutron-rich isotopes decrease more steeply towards higher beam energies as a result of the higher excitation energies of the primary products.

Fig 3.19 shows together the excitation functions of ^{211}Po, ^{212}At, ^{207,208}Rn, ^{212}Fr and ^{213}Ra. The same characteristics of broader excitation functions were observed for the Rn, Fr, Ra with FWHM$\sim$16-20 MeV while much smaller widths are obtained for Po

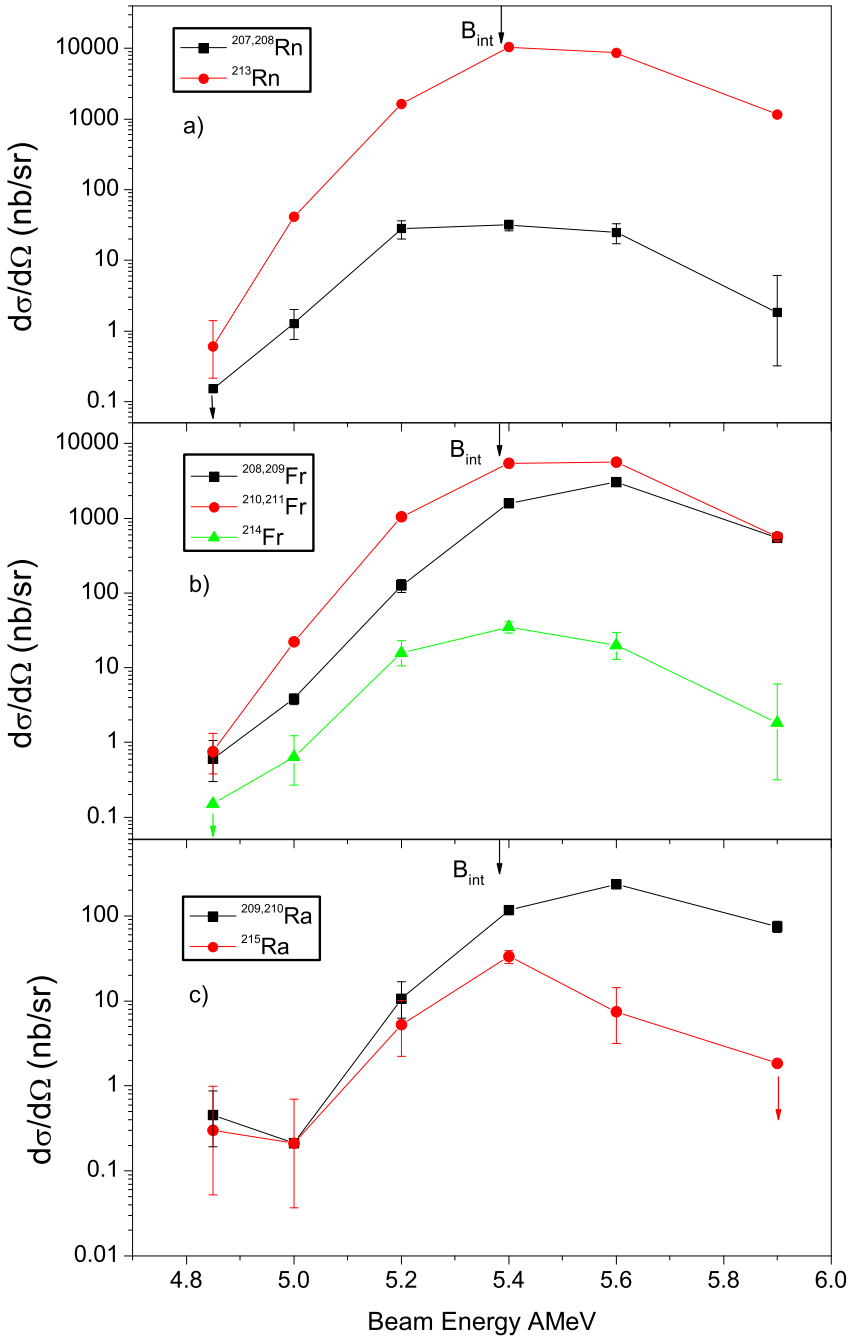

Figure 3.18: Measured excitation functions of the transfer products: a) ^{207,208}Rn and ^{213}Rn; b) ^{207,208}Fr, ^{210,211}Fr and ^{214}Fr; c) ^{209,210}Ra and ^{215}Ra. produced in the reaction ^{58}Ni + ^{207}Pb. The isotopes were produced in the reaction ^{58}Ni + ^{207}Pb.

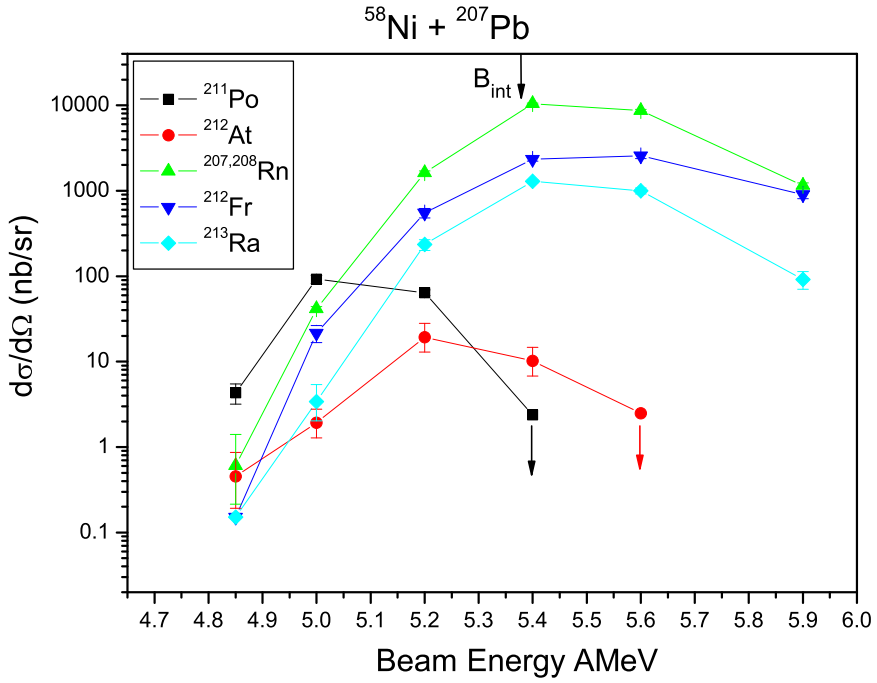

Figure 3.19: Measured excitation functions of the transfer products ^{211}Po, ^{212}At, ^{207,208}Rn, ^{212}Fr and ^{213}Ra produced in the reaction ^{58}Ni + ^{207}Pb.

and At with FWHM=10 MeV and FWHM=12 MeV, respectively. The isotopes of Rn, Fr and Ra presented in these excitation functions are relatively close to the maximum of the Q-value distributions with ΔN=1 to 3 which would correspond to excitation energies up to 30 MeV. In the case of Po and At, the observed isotopes are located even 4 neutrons above the maximum of the Q-value.

3.6 Fusion Initiated by Transfer Reactions

Transfer reactions can be considered as re-separations of the nuclei on the path to fusion. In this sense, the measured energy dissipation, the isotopic distributions and excitation functions presented in previous sections, can be used to study the characteristics of the capture stages and early nucleon transfers in the fusion process. Particularly, the capture process is common for both reactions. The cross-section for the formation of a transfer product can be written as:

$$\sigma_{TP}(E_{cm}, J) = \sigma_{cap} \times P_{PTP} \times P_{sur} \tag{3.10}$$

where E_{cm} is the beam energy in the center of mass, J is the total angular momentum, σ_{cap} is the capture cross-section, P_{PTP} is the probability to form a certain primary transfer product and P_{sur} is the survival probability due to de-excitation of the primary product. This is similar to the formation of ER in fusion reactions:

$$\sigma_{ER}(E_{cm}, J) = \sigma_{cap} \times P_{CN} \times P_{sur} \tag{3.11}$$

where P_{CN} is the probability of compound nucleus formation and P_{sur} is the survival probability of the compound nucleus.

The excitation functions of superheavy nuclei produced in cold fusion reactions (Fig 3.20) [67] show peaks at energies located below the Bass barrier. For small beam energies the Coulomb repulsion prevents the formation of a DNS. For larger beam energies the excitation energy of the formed CN is larger and the fission probability also increases, decreasing the survival probability. The same general analysis can be done for transfer reactions. The fact that the maxima of the cold fusion excitation functions are located below the barrier, indicates that it proceeds with small overlap between the parent nuclei where only the outer nucleons interact in touching configurations. This result is in contradiction with the Macroscopical Dynamical Model (MDM) of Swiatecki [68, 69] which described the fusion as a purely dynamical process with classical

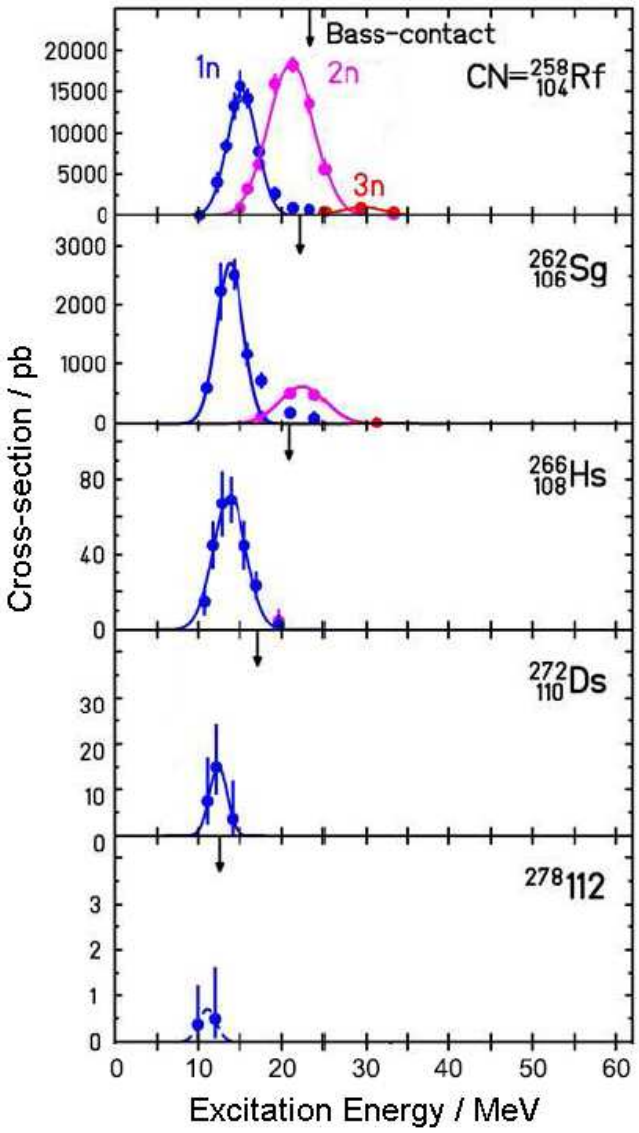

Figure 3.20: Excitation functions for different evaporation residues produced in cold fusion reactions using ^{208}Pb targets [67].

equations of motion. The nuclei were considered as liquid drops and microscopic effects were not taken into account. The model predicted the fusion process to take place at energies larger than the Bass barrier, where a so-called "extra-push" was necessary to overcome the fusion barrier.

The theoretical models widely used nowadays explain the fusion process in the two-center shell model [43–45] where in the contact configuration nucleons can flow from one nucleus to the other following the potential generated by the two nuclei. The flow of protons from the projectile to the target contributes to a reduction in the Coulomb repulsion between the nuclei and eventually a CN can be formed. Within this picture transfer reactions initiate the fusion process and they can be used to get information on the early stages of the process.

Fig 3.21 shows a comparison of excitation functions for certain transfer products with the one of the ER ^{271}Ds. The shown transfer products correspond to the expected primary transfer products and have therefore low excitation energies. The maxima of the excitation functions for transfer and fusion reactions are all located slightly below the Bass barrier. The excitation function of ^{271}Ds drops faster for higher excitation energies compared to the transfer reactions. This difference is a clear signature of the influence of the survival probability (P_{sur}) which in the case of the CN ^{272}Ds is strongly reduced due to the high fission probability. For transfer reaction products, the fission probabilities are much smaller which leads to a flatter decrease in the excitation functions.

On the other hand, the excitation functions of fusion reactions using ^{208}Pb targets, move to higher energies for the 2n and 3n channels become broader as it can be seen in Fig 3.20 in the cases of the production of the ER ^{258}Rf and ^{262}Sg. The same general behavior was observed in our present study on transfer products where the excitation functions broaden and shift to higher energies for increasing excitation energies.

The experimental results are in agreement with the assumptions of the two-center shell model.

Generally, in fusion reactions different projectile-target combinations can be used to produce heavy or superheavy nuclei. The determination of the optimum combination, where the maximum cross-sections are expected, is of great importance for fusion reactions due to the extremely low production cross-sections. In our experiment, the influence of different neutron numbers of the beam particles on the production cross-sections of transfer products was studied. The differences in the capture process and early nucleon transfers are commonly interesting for both, transfer and fusion processes.

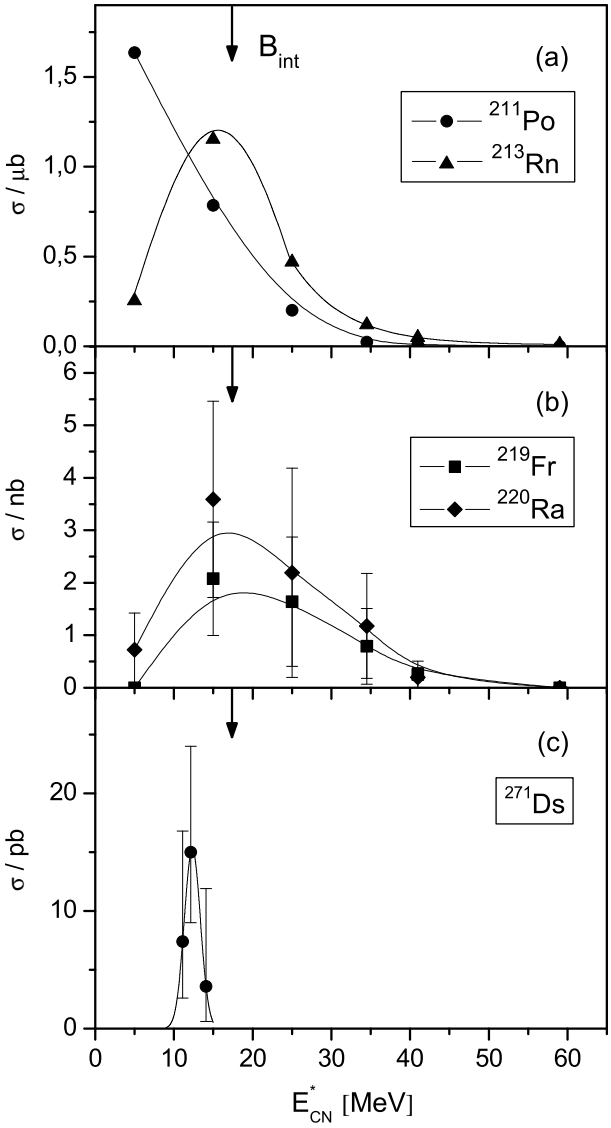

Figure 3.21: Measured excitation functions for the transfer products ^{211}Po and ^{213}Rn (a) and ^{219}Fr and ^{220}Ra (b), produced in the reaction ^{64}Ni + ^{207}Pb. (c) Excitation function of ^{271}Ds produced in the cold fusion reaction ^{64}Ni + ^{208}Pb [67]. For a direct comparison of transfer and fusion reactions all cross-section are plotted as a function of the excitation energy of the (hypothetical) nucleus Ds.

The reactions with ^{58}Ni beams showed larger values of the overlap parameter compared to the ^{64}Ni reactions, indicating more distant collisions as it was shown in the previous sections. Nevertheless, the measured transfer reaction cross-sections were larger in the ^{58}Ni case with smaller overlap.

The survival probability term P_{sur} in Eq 3.10 should not be the dominant factor to explain the differences in the transfer cross-sections between ^{58}Ni and ^{64}Ni reactions considering the similar fission barriers expected for the produced isotopes. Generally, it is difficult to disentangle the contributions of the two other factors, the capture cross-section (σ_{cap}) and the transfer probabilities (P_{PTP}). Nevertheless, it is possible to extract some conclusions from the data. The capture cross-sections for these two reactions were calculated in [70] and are shown in Fig 3.22. For beam energies close and below the barrier, the capture cross-sections in ^{64}Ni reactions (solid curve) are up to several orders of magnitude larger than in the case of ^{58}Ni reactions (doted curve), and only a factor of two larger for higher beam energies. However, the experimental data show ten times higher cross-sections for ^{58}Ni reactions at energies below as well as above the barrier. A possible explanation to this contradiction can be obtained considering the effect of the two-neutron transfer from the target to the projectile as it was predicted (details in [70]) for double magic or semi-magic spherical projectile and target combinations where a positive Q-value is obtained for the process. For example, the effect takes place in the systems ^{40}Ca + ^{208}Pb (Q_{2n}=5.7 MeV) and ^{40}Ca + ^{96}Zr (Q_{2n}=5.5 MeV) as it was concluded in [70] using the experimental data of the reactions studied in [71–74]. It is assumed [75], that the two-neutron transfer takes place before capture of the projectile by the target at large distances which can lead to the population of the first 2^+ state of the recipient nucleus. After the transfer, the potentials are eventually different since different mass numbers, Coulomb barriers, and deformations might be present leading to enhancement or hindrance of the capture cross-section. In the case of Ni + Pb reactions the Q-value for the two-neutron transfer is Q_{2n}=5.5 MeV for ^{58}Ni and Q_{2n}=0.2 MeV for ^{64}Ni. Therefore the two-neutron transfer is more likely in ^{58}Ni reactions. The two-neutron transfer would lead to the population of the 2^+ state in ^{60}Ni which leads to rather different quadrupole deformation parameters, $\beta_2(^{58}\text{Ni})$=0.05, $\beta_2(^{60}\text{Ni})$=0.207, $\beta_2(^{205,207}\text{Pb})$=0, resulting in a lowering of the Coulomb barrier and an enhancement in the capture cross-sections. The enhancement leads to similar capture cross-sections for ^{58}Ni (Fig 3.22 dashed curve) and ^{64}Ni (solid curve) reactions for the energy range covered in the experiment (E_{cm} >235 MeV) where the cross-section for ^{58}Ni is still lower than the one of ^{64}Ni. In general, the consideration of a two-neutron transfer before the capture process can

not explain the ten times larger cross-sections with ^{58}Ni reactions observed in the experiment. If the two-neutron transfer mechanism took place in the reactions can not be finally decided by the available data because the very low energy region where the effect should become most pronounced was not covered in the experiment.

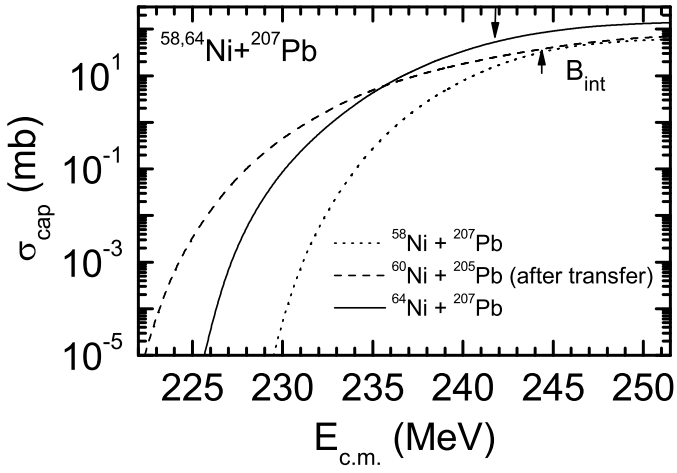

Figure 3.22: Capture cross-sections for the reactions ^{58}Ni + ^{207}Pb (doted curve), ^{64}Ni + ^{207}Pb (solid curve) and ^{60}Ni + ^{205}Pb (dashed curve) calculated in [70]. The arrows represent the Bass barrier energy for the reactions with ^{58}Ni and ^{64}Ni.

Since approximately the same capture cross-section values are expected for both beams in the energy interval covered in the experiment, one can conclude that the differences in the transfer reaction cross-sections between ^{58}Ni and ^{64}Ni beams can be attributed to the influence of the transfer probability term (P_{PTP}). Obviously, for ^{58}Ni reactions nucleons flow in a easier way from the projectile to the target. Such a behavior can be seen in Fig 3.23 which shows the sum of the cross-sections of all transfer products with a certain proton number Z. The selected beam energies correspond to the Coulomb barrier for each system. Apart from the larger cross-sections for ^{58}Ni reactions, a flatter behavior towards higher proton number of the transfer products indicates that nucleons are in general easier transferred in ^{58}Ni reactions compared to the ^{64}Ni case.

As it was pointed out before in previous sections, a striking difference was observed in the production of the isotopes of ^{211}Po and ^{212}At for both reactions. They resulted from quasi-elastic reactions with ^{58}Ni beams and from DITR with ^{64}Ni. In

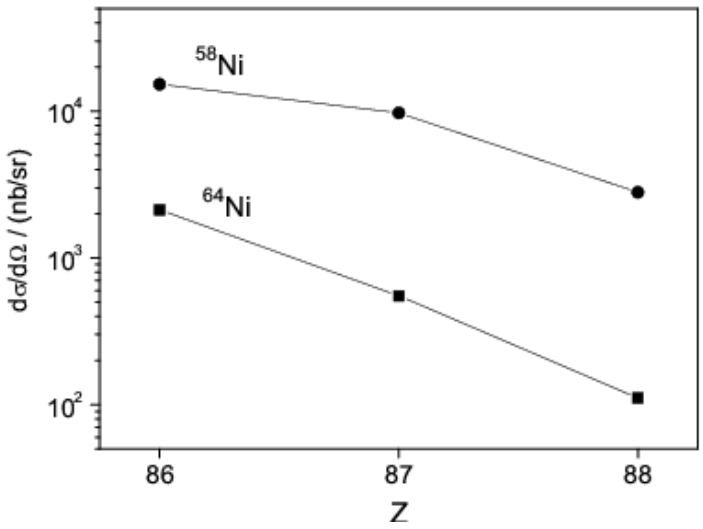

Figure 3.23: Measured cross-sections of the transfer reaction products produced with ^{58}Ni (5.4×A MeV) and ^{64}Ni (5.0×A MeV) as a function of the proton number Z. For a given Z, the production cross-sections of all observed isotopes were added.

the particular case of ^{211}Po, a possible explanation of the measured TKE in the ^{58}Ni reactions is the quasi-elastic transfer of an α-particle from the projectile to the target. The transfer of an α-particle was the mechanism assumed to take place in the reaction ^{208}Pb (^{18}O,^{14}C)^{212}Po [76] where states of "α-^{208}Pb" configurations where reported. In our case, the transfer product ^{211}Po was produced in quasi-elastic reactions, and the largest cross-sections were measured for beam energies below the barrier, where only the outer orbits of the nuclei are in touch. The latter suggests the presence of a direct reaction where a pre-formed α-particle is transferred in a one step reaction with small amount of energy dissipation. Another possible explanation is the influence of the transfer probability factor which is larger in the case of ^{58}Ni reactions. The nucleons are transferred in an "easier" way from the projectile to the target with smaller nuclear overlap needed which result in less energy dissipation in the case of the produced isotopes ^{211}Po and ^{212}At. For larger number of transferred protons, the deep inelastic component dominates.

Such effects, like the two-neutron or heavy cluster transfers like an α-particle, in the very early stages of a nuclear reaction even before the capture process takes place, are of extreme interest for fusion reaction studies, particularly in the production of superheavy nuclei. In these cases, where extremely low production cross-sections are expected, the

determination of the cross-sections for a given combination of projectile and target play a major role in the experiments. The early transfers could result in smaller Coulomb barriers and consequently, larger fusion probabilities. It also contributes significantly to our understanding of the fusion process as a whole.

Taking into account the observations discussed above one can conclude that larger transfer cross-sections were found for the neutron deficient beams, suggesting the use of such projectiles in fusion reactions which should lead to larger CN formation probabilities. Nevertheless, neutron deficient superheavy evaporation residues have very small lifetimes and the survival probabilities against fission of the CN become small due to low fission barriers. In order to explore more neutron rich nuclei, neutron rich projectiles must be used.

3.7 Production of Neutron Rich Isotopes in Transfer Reactions

Due to the inclination of the stability line with respect to N=Z, towards higher neutron numbers for heavy nuclei (Fig 3.24), fusion reactions using stable isotopes produce mainly neutron-deficient heavy and superheavy nuclei. Transfer reactions have been predicted to be a possible tool to reach unknown regions of the isotopic chart [3, 4].

In recent times, extensive calculations have been performed applying the two-center shell model with diabatic or adiabatic potentials to predict the cross-sections of new neutron rich heavy and superheavy nuclei in transfer reactions. The main difference is that in the diabatic model, multi-nucleon transfer reactions are only obtained for intermediate heavy projectiles. An example is the production of nuclei with Z=102-108 in the reactions ^{48}Ca + ^{248}Cm [4]. In the case of heavier systems like U+U or U+Cm, only direct reactions are predicted by this model, with small nuclear interaction times of $\sim 10^{-22}$ s which does not allow the occurrence of transfers of a large number of nucleons. On the other hand, the adiabatic model predicts longer interaction times of several times 10^{-21} s in the reactions of U+U and U+Cm with large transfer probabilities influenced by the shell effects of the double magic ^{208}Pb nucleus. Within this model, the influence of the shells on the transfer reaction cross-sections for superheavy nuclei are of essential importance. So far, no experimental data exists for this region to probe the model predictions and the optimum projectile-target combination is still an open question.

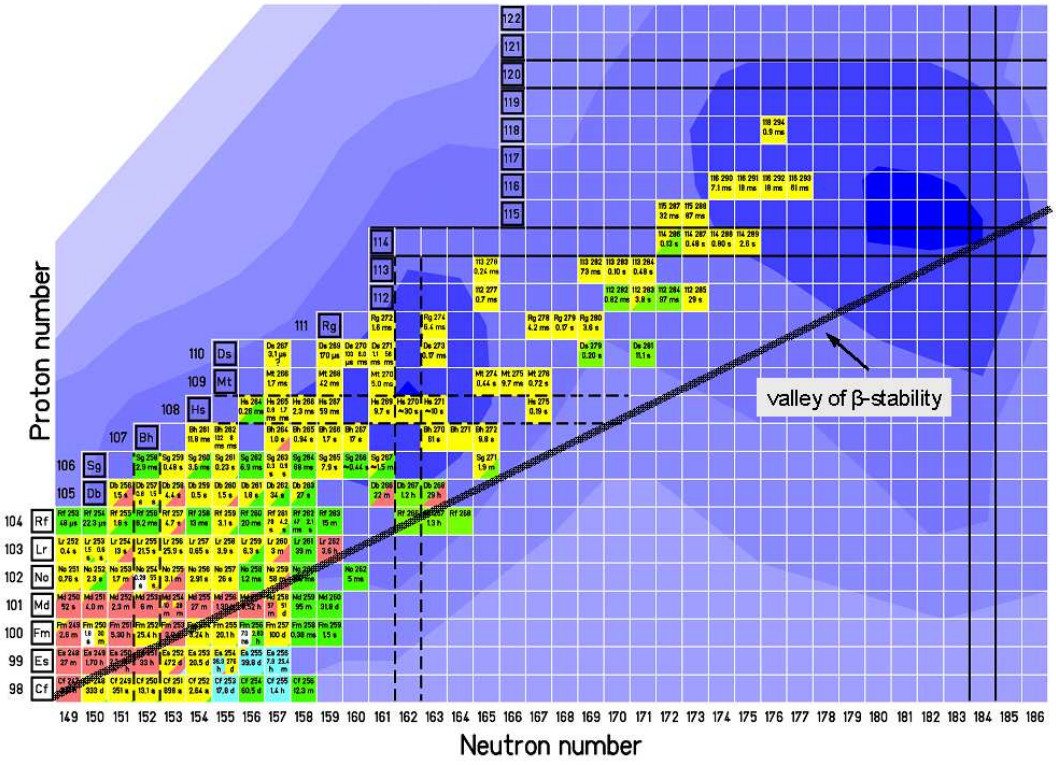

Figure 3.24: Chart of isotopes for elements with proton numbers Z≥98. The line indicates the beta stability line roughly extrapolated to the superheavy region considering it passes through Z=114, N=184. The blue background represents the calculated shell correction energies according to the macroscopic-microscopic model.

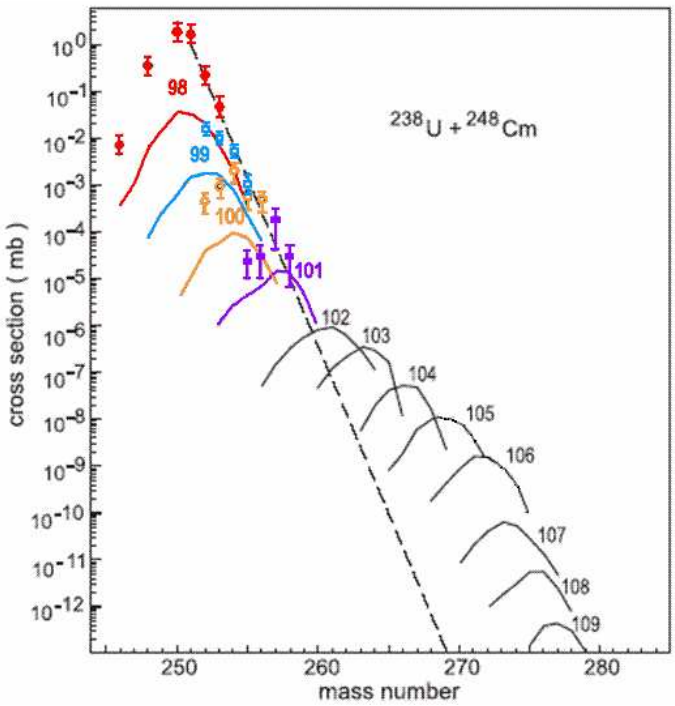

Figure 3.25: Calculated (solid lines) [3] and measured (symbols) [26] cross-sections for the survived transfer products in ^{238}U + ^{248}Cm reactions at the beam energy E_{cm}=800 MeV. The dashed line represents the cross-section trend in the absence of shell effects.

Fig 3.25 shows an adiabatic model calculation for the reaction ^{238}U + ^{248}Cm at the center of mass energy E$_{cm}$=800 MeV [3]. The symbols represent the data from an experiment performed in 1982 [26], where nuclei up to Z=101, N=157 could be identified using radiochemical methods. These methods have as a main limitation the relatively long half-lives (t > 10 s) needed for the proper identification of the reaction products. A pronounced shoulder is predicted by the model around Z=106 for this reaction. The shoulder appears as a result of the shell effects in the break-up of the system formed by U + Cm. A deep valley in the potential energy surface is expected due to the double shell closure at Z=82, N=126 of ^{208}Pb. Nuclei within this valley are then preferentially produced as transfer products. As a result, the heavier transfer reaction products, complementary produced in the reactions, are expected to be located in the region close to Z=106, N=172. For nuclei with Z<82 and Z>106 a steep drop in the production cross-section is expected due to the increasing potential and the smaller influence of the shell effects. The dashed line (Fig 3.25) assumes no shell effect in the calculations. In this case the cross-section drops exponentially with increasing number of transferred protons. It can be seen that the experimental data points are still far from the region where shell effects are expected.

The same model calculations have been performed for the reactions ^{232}Th + ^{250}Cf and ^{238}U + ^{238}U [77]. Fig 3.26 shows a comparison with the ^{238}U + ^{248}Cm reaction. In the upper right corner the distribution of the primary fragments is shown for the ^{232}Th + ^{250}Cf reaction. The primary fragments are first produced in the reaction but they are generally excited and de-excitate by fission or emitting nucleons and gamma rays, giving rise to secondary reaction products. The distribution of secondary products are represented by the solid curves for the ^{232}Th + ^{250}Cf reaction, dotted for ^{238}U + ^{248}Cm and dashed for the ^{238}U + ^{238}U reactions. The production cross-sections are generally smaller for the ^{238}U + ^{238}U reaction, where also more neutron deficient isotopes are produced. In the case of ^{238}U + ^{248}Cm and ^{232}Th + ^{250}Cf reactions comparable production cross-sections are obtained but slightly more neutron-rich distributions for the Th + Cf reaction.

Massive transfers have been experimentally seen for example in the reaction ^{238}U + ^{238}U [78] at the beam energy 7.42×A MeV studied in 1979. In the experiment, increasing nucleon transfers were seen with increasing energy damping. In 2006, an experiment using the reaction ^{238}U + ^{238}U [79] was performed at the mass spectrometer VAMOS [80] at GANIL at relatively low beam energies. The data revealed a massive transfer of nucleons correlated with a large energy dissipation of up to several hundreds MeV. The latter means that a time delay must occur in such heavy systems. Nevertheless,

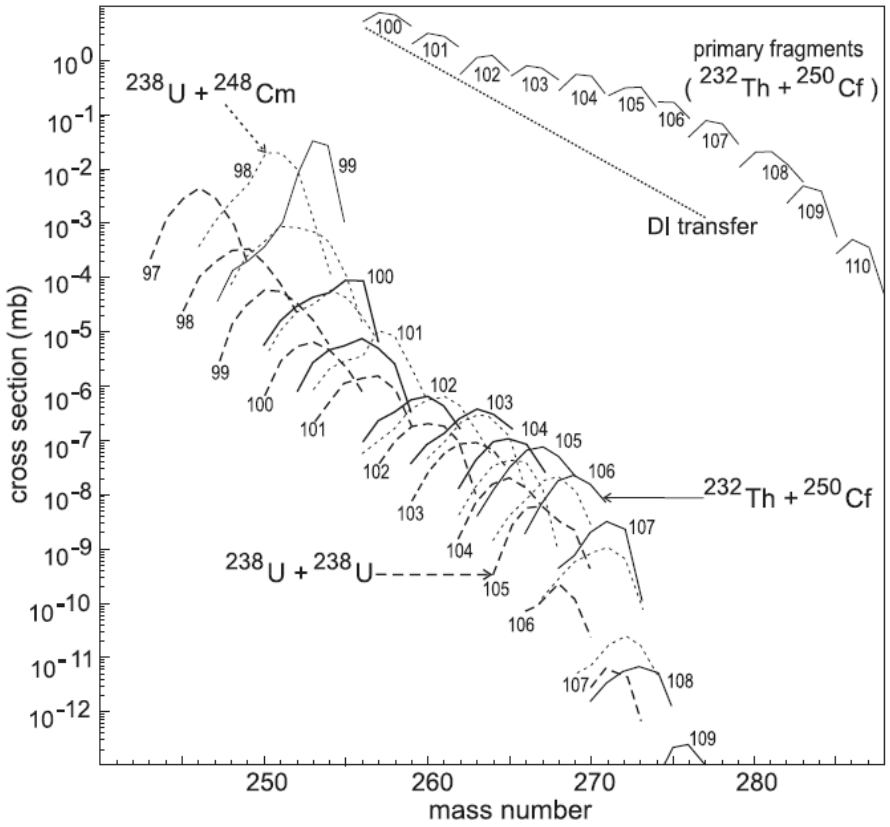

Figure 3.26: Calculated cross-sections for different projectile and target combinations. The reaction ^{232}Th + ^{250}Cf is represented by solid curves; ^{238}U + ^{248}Cu reactions by the dotted curves and the ^{238}U + ^{238}U reactions by the dashed curves [77]. In the up right corner the distribution of the primary products in the reaction ^{232}Th + ^{250}Cf is shown.

no reaction products heavier than uranium were observed in both experiments.

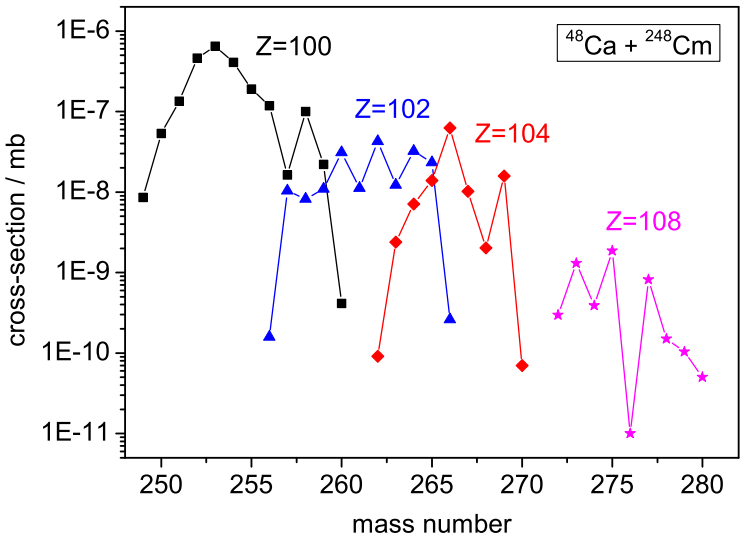

Figure 3.27: Calculated production cross-sections of neutron rich isotopes of elements with Z=100, 102, 104, and 108 produced as transfer products in the reaction ^{48}Ca + ^{248}Cm from [46].

Experiments using medium heavy projectiles plus heavy targets in the reactions ^{40,44,48}Ca + ^{248}Cm were also studied in 1992 [27] and nuclei up to Z=100, N=156 were identified using radiochemical identification methods. Similar cross-sections were measured for the isotopes up to Z=101 using medium heavy and heavy projectiles. For example cross-sections of 1 μb where measured for Z=100 and N=156 in the reaction with Ca+Cm and U+Cm. Also theoretical calculations show similar cross-sections for the application of medium heavy projectiles and heavy projectiles [4]. As an example, Fig 3.27 shows the calculated production cross-sections of neutron rich isotopes of elements with Z=100, 102, 104 and 108 produced as transfer products in the reaction ^{48}Ca + ^{248}Cm [46].

In our experiments a large amount of transferred nucleons were observed. Particularly, in the reactions with ^{64}Ni beams, secondary products with up to 7 protons and 8 neutrons beyond the proton and neutron numbers of the target nucleus were detected. The Q-value plays a major role in the measured isotopic distributions. In the case of ^{58}Ni reactions a drop in the Q-value distribution for N>127 prevents the production of

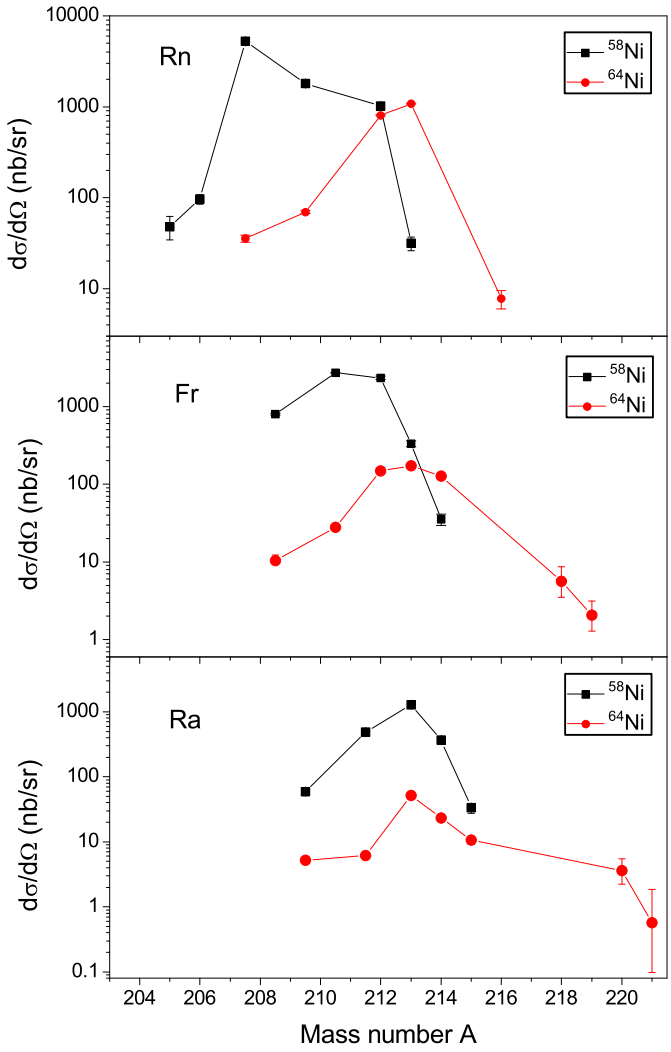

Figure 3.28: Measured isotopic distributions for the neutron rich isotopes of Rn, Fr and Ra as functions of the mass number A of the transfer product for the reactions with ^{58}Ni (black) and ^{64}Ni (red) at the beam energies 5.4 and 5.0 $\times$A MeV, respectively.

neutron-rich isotopes. In the case of ^{64}Ni reactions, the Q-value distributions are flatter towards neutron-rich isotopes and nuclei up to ^{221}Ac (transfer of 7p7n) and ^{221}Ra (transfer of 6p8n) were detected. Fig 3.28 shows the isotopic distributions for both reactions for energies close to the respective Coulomb barriers. Selecting the points from the maxima of the distribution towards the neutron-rich side and performing linear fits it is possible to compare the slopes of the distributions for both reactions. The relative values of the slopes for ^{64}Ni and ^{58}Ni reaction are 2.4 (Rn), 29.3 (Fr) and 135 (Ra). It is possible to notice that faster drop takes place in the case of ^{58}Ni reactions. The slope differences become larger for larger proton number of the transfer products. In the case of ^{64}Ni reactions the cross-sections drop by a factor of 350 for every additional neutron for Rn, by a factor of 30 for Fr and 7 for Ra.

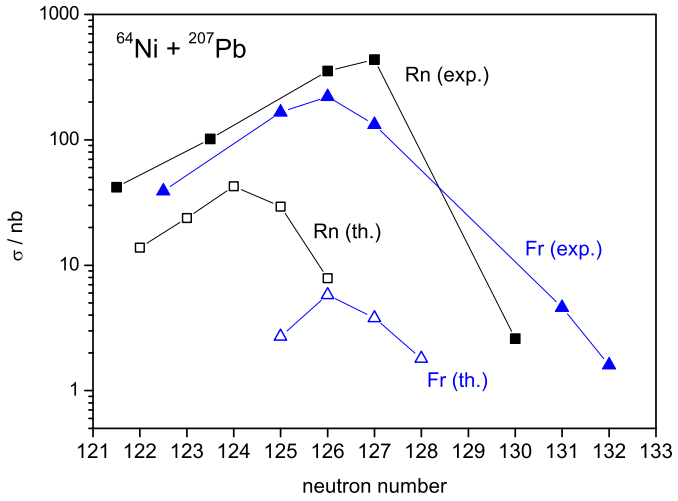

Figure 3.29: Calculated [81] and measured isotopic distributions for Rn and Fr as functions of the neutron number N of the transfer product for the reactions ^{64}Ni + ^{207}Pb at the beam energy 5.0 ×A MeV.

The maxima of the excitation functions were found for low beam energies even below the Coulomb barrier which is an indication of the low excitation energy needed to survive the fission and nucleon evaporation process in such cases. Higher beam energies lead to higher excitation energies of the primary transfer products and to larger fission probabilities and neutron evaporation, decreasing the survival probability (P_{sur}). In this context, the excitation functions of the neutron-rich isotopes show the same general behavior as the ones of the fusion reactions.

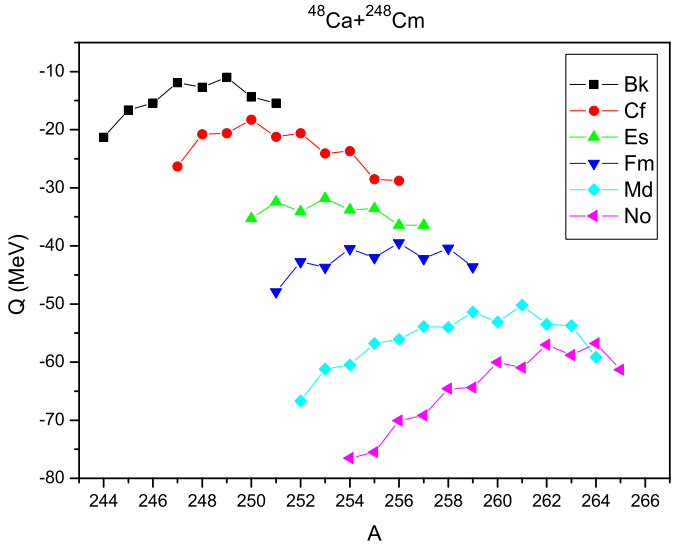

Figure 3.30: Q-values of the reactions where the isotopes of Bk, Cf, Es, Fm, Md and No were produced in ^{48}Ca + ^{248}Cm collisions. The values were taken from the Audi and Wapstra table [63].

A comparison of the adiabatic model calculations [81] with the measured transfer reaction cross-sections of the secondary products is shown in Fig 3.29 for the reaction ^{64}Ni + ^{207}Pb at the beam energy of 5.0 ×A MeV which is located close to the Coulomb barrier. In the theoretical calculations the same shift is obtained between the primary and the secondary products in the cases of Rn and Fr isotopes. The influence of the shell effects observed in the experiments resulting in rather cold Rn isotopes compared to the Fr isotopes was not seen in the calculations. The calculated cross-section values are approximately one order of magnitude smaller than the experimental results and the difference becomes larger for increasing number of transferred protons. A limit of 1 nb was set for statistical reasons for the calculations and this is why the more neutron-rich isotopes do not appear in the calculated isotopic distributions. It is possible to conclude that for the present studies in the Pb region, the adiabatic model underestimates the transfer reaction cross-sections. In the case of heavier systems an underestimation could also take place. In this sense, it is of essential importance to obtain experimental data using such reactions. Model calculations for ^{58}Ni reactions within the adiabatic model were not performed.

Diabatic model calculations for the studied reactions in the present thesis work were not found in the literature. In this sense, a direct comparison of the two models (diabatic and adiabatic) with experimental data could not be done for the measured data.

From our experiments, the Q-value distributions seem to be a good approach for selecting the optimum projectile-target combinations to produce certain unknown neutron-rich isotopes. A further step using the velocity filter SHIP is the study of heavier regions populated in transfer reactions like ^{48}Ca + ^{248}Cm. Fig 3.30 shows the Q-value distributions for the isotopes ranging from Bk to No produced as transfer products in this reaction. The Q-values for the heavier isotopes increase towards the neutron-rich isotopes; for example, in the case of No, the maximum of the Q-value distribution (primary transfer products) is found for the isotope ^{266}No which is already located in the region of unknown isotopes.

Chapter 4

Nuclear Interaction Times

As it was mentioned before in Chapter 1, different nuclear reaction processes can be characterized by their time scales. Direct reactions are fast processes with time scales on the order of $\sim 10^{-22}$ s. The characteristic times of the reactions involving the formation of a DNS are considered to be up to 10^{-20} s, which is long enough to establish a quasi-equilibrated system. In the case of reactions with CN formation the time scale of the process is on the order of 10^{-20} s to $\sim 10^{-18}$ s where complete statistical equilibrium is reached. In the present Chapter, general experimental methods used to determine the nuclear interaction times will be presented and the determination method and results using our experimental set up SHIP.

4.1 Experimental Methods to Determine Nuclear Interaction Times

There are several experimental approaches to determine the interaction times of nuclear reactions. The information about the DNS is obtained in an indirect way since only the resulting reaction products are detected and the complex DNS interactions are generally difficult to reconstruct. Also a proper separation between DITR and other reaction mechanisms is required. Several methods have been already applied in the past to determine the interaction times:

(i) Investigation of the energy spectra of the δ-electrons emitted in nuclear reactions [82–84]. A time delay in the nuclear reaction leads to oscillations in the energy spectra of the δ-electrons. Interaction times can be deduced from the widths of the oscillations.

The method has been called an *Atomic Clock* for nuclear contact times on the order of 10^{-21} - 10^{-19} s. For example, it was used to estimate the interaction times in the reaction Au + U [85] at bombarding energies of 8.65 ×A MeV. Times on the order from 10^{-21} s to 10^{-20} were deduced for total kinetic energy losses (TKEL) in the range of 100 MeV to $\sim$ 400 MeV respectively.

(ii) The neutron clock method [86, 87] measures the number of pre-scission neutrons emitted from a DNS or CN before the re-separation in two fragments occurs. The typical lifetime for the emission of the first neutrons is (10^{-22} - 10^{-20} s) which is small compared with the characteristic times for fission events (>10^{-20} s). The neutron emission is the dominant process allowing to use the neutrons as a clock, each additional neutron would correspond to an increase in the time from the formation of the DNS. The method is suitable for time scales in the range from 10^{-21} s to $\sim$ 10^{-16} s. To estimate the time scales it is important to know the neutron evaporation lifetimes and the dynamics of the process.

(iii) Methods using the deflection function, which is in general the deflection produced due to nuclear interactions from the Rutherford trajectories. These methods use the mass and/or charge distributions of the reaction products together with angular distributions to estimate the interaction times [88, 89]. For example the mass angular distribution MAD was used [90] in the reactions of ^{48}Ti and ^{64}Ni projectiles using W targets. The projectile energies were 220-260 MeV for Ti and 310-341 MeV for Ni. The interaction time scales obtained were $\leq 10^{-20}$ s. The time scales are obtained through a Monte Carlo simulation of the MAD which are compared with the measured distributions. Within this approach the systematic uncertainties are considered to be considerably less than 50%. In a much heavier collision system, U + U at 7.35 ×A MeV [79], interaction times of $\sim 8\times10^{-21}$ s for TKEL of 300-350 MeV were extracted applying the diffusion model and the linear dependence of the interaction times τ on the variance of the primary mass distribution σ_A^2. Another experiment using cold reactions of ^{86}Kr + ^{54}Fe (E_{Lab}=310 MeV) and ^{82}Se + ^{56}Fe (E_{Lab}=267 MeV) was done measuring in an angle interval of $\Delta\theta = 30°$ [61]. The reported interaction times were τ=8^{+3}_{-4} × 10^{-22}s and τ=6^{+5}_{-2} × 10^{-22}s respectively which are comparable to the direct reaction times.

(iv) The crystal blocking method which is a time of flight technique where the charged decay products are blocked by a row of atoms resulting in a dip in the yield in the direction of a crystal axis unless the di-nuclear system or the CN formed recoils more than a certain distance ($\gtrsim$5 pm) from the row of atoms [91]. The widths of

the dips can be used to determine how far from the row the composite system moved before the separation in two nuclei takes place and taking the beam energy into account the interaction times can be estimated. As an example, this method was used in the reactions 180 MeV ^{36}S, 240-255 MeV ^{48}Ti, 330-375 MeV ^{58}Ni and 390 MeV ^{74}Ge projectiles using W targets [92, 93]. The lifetimes of the fission events obtained were on the order of 10^{-18} s with almost no dependence on the atomic number of the composite system. This result is inconsistent with the Bohr-Wheeler model of the fission from a statistically equilibrated CN. It was suggested that the events were produced in very slow quasi-fission processes, also in contradiction with the present understanding of the process.

In general the experimental determination of the interaction times are strongly attached to different models or simulations. Also, the results of the crystal blocking and the deflection function methods are in clear contradiction.

4.2 Determination of Nuclear Interaction Times at SHIP

The properties of SHIP can be used to perform a rather direct measurement of the interaction times in DITR. Particularly, from the measured velocity distributions one can compare the production rates of the isotopes at two different rotation angles 0° and 180° (details in Chapter 2) and use this result to estimate the nuclear contact times.

Velocity distributions covering the low velocity region with sufficient statistics were measured in the ^{64}Ni + ^{207}Pb reaction at the beam energy of 5.92×A MeV. Fig 4.1 shows the velocity distributions of the isotopes ^{212m}At, ^{213}Rn, ^{213}Fr and ^{215}Ra produced in DITR. The isotopes of Po were excluded from the analysis due to low statistics. The yields of the low velocity peak become smaller for less number of transferred protons. Therefore, the velocity distribution for the isotope ^{212m}At is presented for a better understanding of the general trends of the distributions, but it was not used further to calculate the interaction times.

In order to compare directly the intensities of the two peaks, some factors affecting these values must be taken into account:

1. Differences coming from the scattering in the target. The transfer products with low velocities will result in larger dispersion and scattering angles inside the target compared to the products with higher velocities. Scattering angles larger than the acceptance angle of SHIP (2°) result in the loss of the reaction product.

The simulations were performed using the TRIM code based on Monte Carlo calculations [94]. A factor of ∼10 could be extracted as the difference in intensity due to scattering between the two peaks.

2. Different detector efficiencies for the different implantation depths inside the detector. For example, for the ^{213}Fr isotopes the kinetic energy in the laboratory system for the low velocity peak is ∼6.6 MeV and for the high velocity peak it is ∼178 MeV which result in quite different implantation depths inside the detector of 1.35 μm and 19 μm respectively. Considering the α energy of the ^{213}Fr and its range in the detector material (Si) one can estimate the relation between the efficiencies of the detector using equation 2.2 presented in Chapter 2. A value of ε(d=19μm)/ε(d=1.32μm)=1.47 can be obtained where ε is the efficiency value for a given implantation depth.

As mentioned previously in Chapter 3.2, after considering these effects, there is still

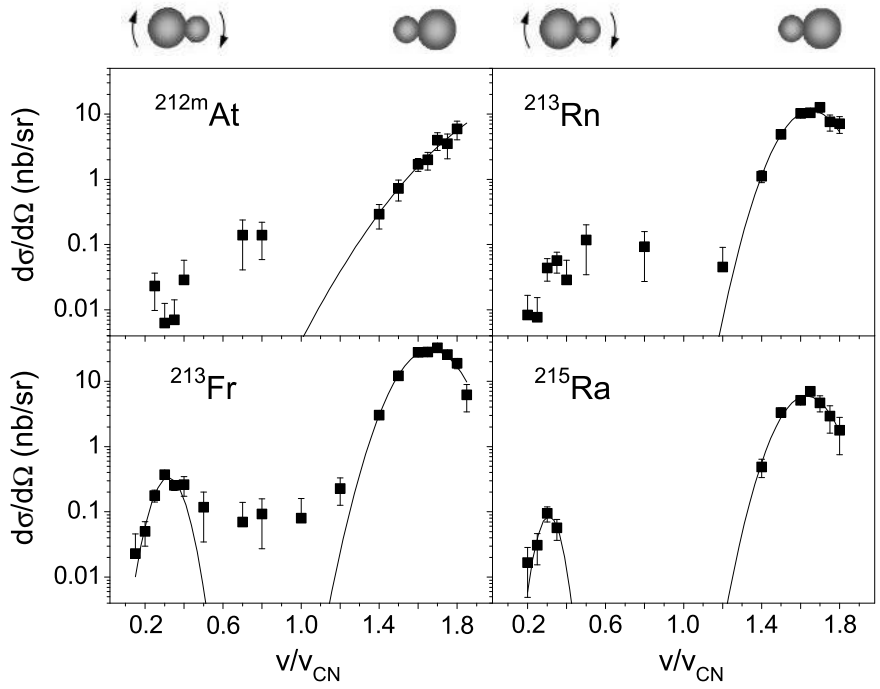

Figure 4.1: Velocity distributions for the reaction products ^{212m}At, ^{213}Rn, ^{213}Fr, ^{215}Ra.

a difference of a factor of approximately 10 between the corrected intensities of the two peaks which indicates that the isotopes were produced in a non isotropic process. The contribution to the peaks from fusion-fission decays can be neglected as it will be shown in the following. The capture cross-section is $\sigma_{cap} \simeq 10$ mb and the CN formation probability is $P_{CN}=\simeq 10^{-2}$ [46] resulting in a CN formation cross-section of 100 μb. Taking into account the angular acceptance of SHIP for the detection of isotropically emitted fission fragments and the estimated probability for very asymmetric CN fission leading to the observed isotopes, one would expect at least three orders of magnitude lower cross-sections than observed in the experiment. Finally, also the measured isotopic distributions of the reaction products shown in the previous Chapter can not be explained by CN fission but are typical for quasi-fission products. As an example, in the study performed with lighter systems like ^{48}Ti and ^{64}Ni + ^{nat}W [90], it was concluded that the contribution of fusion fission events to the measured cross-sections was expected to be much less than 10%.

The lifetimes of the DNS are strongly influenced by the proton numbers of the projectile and target nucleus, the beam energy and the angular momentum which determine the depth of the potential minimum. In the following the parameter of the DNS model are used for the extraction of the lifetimes. The DNS critical and average angular momenta can be calculated using the quasi-fission barrier of B_{qf}=1 MeV [6, 46]. The critical angular momentum for the formation of the DNS is $L_{crit} = 22\hbar$ and the average angular momentum is <L>=16$\hbar$. The angular momenta larger than the critical value do not contribute to DNS formation since no potential pocket is expected to occur.

In the following it is assumed that the largest contribution to the DNS formation cross-section comes from collisions with the average angular momentum <L> and that the moment of inertia, I_{DNS}, of the system does not change noticeable during the rotation. In this case one can estimate the angular velocity of the composite system as

$$\omega_{DNS} = \frac{2\pi}{T} = \frac{< L >}{I_{DNS}} \tag{4.1}$$

where T is the time for a full rotation. We calculated the moment of inertia by assuming spheres separated by a distance of $R = R_1 + R_2$ between the centers where R_1 and R_2 are the radii of the projectile and target nuclei, respectively. With this one obtains $T = 6.76 \times 10^{-20}$ s. Further we assume that the decay of the DNS follows the decay law:

$$\frac{dN}{dt} = -\lambda N \tag{4.2}$$

where λ is the decay constant of the DNS. One can then estimate the mean lifetime $\tau = 1/\lambda$ from the number of decays registered at two different angles. In our case, the number of events in the high velocity peak, N_1, corresponds to the number of decays at the angle of 0° and the number of events in the low velocity peak, N_2, corresponds to the decays at 180°. Finally, the ratio of the yields in the low and high velocity peaks is given by

$$\frac{N_2}{N_1} = exp(-\lambda \Delta T_{180}) \tag{4.3}$$

ΔT_{180} is the time for a 180° rotation.

The Table 4.1 shows the obtained experimental mean lifetimes. The experimental values are in agreement with the non-isotropic DNS decay signature. A full rotation of the DNS takes $6.76\times\ 10^{-20}$ s which corresponds to approximately 6 times the measured half-lives. Only 1.5% of the total decays are expected to occur after this time. In this sense the contributions to the high-velocity peak resulting from DNS decays after $\sim 360°$ rotations are very unlikely. The values of τ increase for increasing number of transferred protons. This result is expected since larger number of nucleon transfers result from larger interaction times. It is also in accordance with the expected differences in the potentials of the exit channels, which are stronger repulsive for more symmetric systems and lead to faster DNS decays compared to the more asymmetric ones.

Theoretically, the decay of the DNS in the relative distance between the nuclei R is commonly treated with the one-dimensional Kramers rate $\Lambda^{qf}_{Z,N}(\Theta)$ [95–99]:

$$\begin{aligned} \Lambda^{qf}_{Z,N}(\Theta) &= \frac{\omega}{2\pi\omega^{B_{qf}}} \left(\sqrt{\left(\frac{\Gamma}{2\hbar}\right)^2 + \left(\omega^{B_{qf}}\right)^2} - \frac{\Gamma}{2\hbar} \right) \\ &\quad \times exp\left(-\frac{B_{qf}(Z,N)}{\Theta_{qf}(Z,N)} \right) \end{aligned}$$

In the last equation B_{qf} is the quasi-fission barrier height, Θ_{qf} is the temperature calculated using the Fermi-gas equation $\Theta_{qf} = \sqrt{(E^*/a)}$ where E^* is the DNS excitation energy and a is the level density parameter $a=A_{tot}/12$ MeV^{-1}. The frequencies $\omega^{B_{qf}}$ and ω are the harmonic oscillator frequencies approximating the potential in R from the top of the quasi-fission barrier and the bottom of the potential pocket respectively. In the reaction considered in the present study, ^{64}Ni + ^{207}Pb, the values are $\Gamma = 2.8$ MeV, $\hbar\omega$=2.0 MeV and $\hbar\omega^{B_{qf}}$=1.0 MeV. For the quasi-fission barrier we used different values for the different exit channel: $B_{qf} = 1.9MeV$ for Rn, $B_{qf} = 2.4MeV$ for Fr and

Produced Isotopes	$\tau_{exp}\times10^{-20}$ s	$\tau_{theo}\times10^{-20}$ s
^{213}Rn	1.1±0.1	1.5
^{213}Fr	1.9±0.2	1.9
^{215}Ra	2.0±0.3	2.3

Table 4.1: Experimental and theoretical mean lifetimes for the isotopes: ^{213}Rn, ^{213}Fr and ^{215}Ra produced in the reaction ^{64}Ni + ^{207}Pb at the beam energy of 5.92×A MeV. Only uncertainties due to statistical errors are shown.

B_{qf}=2.9 MeV for Ra in accordance with [6, 46].

Using the measured TKE, it is possible to estimate the excitation energy of the nuclear complex system resulting in the theoretical lifetimes presented in the 3rd column of the Table 4.1.

The theoretical values, τ_{theo}, are well in agreement with the experimental results. The time scales on the order of 10^{-20}s are comparable with those obtained using the MAD results [90] of $\leq 10^{-20}$s for similar systems. Nevertheless, our results show a slightly slower decaying system. Apart from the relatively large error bars, the difference may come due to the fact that in our experiments, reactions proceeding with transfers from the projectile to the target nuclei were analyzed and the reactions using the MAD method considered reactions with transfers in the opposite direction, from the heavier target nuclei to the projectile. The Coulomb repulsion increases for more symmetric systems which results in faster decaying DNS.

The extracted lifetimes are also influenced by the parameters used in the respective model. An estimation of the lifetimes is presented in the following if another type of model which uses adiabatic internuclear potentials [100] is applied for the interpretation of the data. In this model a strong neck develops between the nuclei and all angular momenta up to the grazing angular momentum contribute to the formation of the composite nuclear system. The grazing angular momentum for Ni + Pb collisions at 5.92×A MeV is 157 $\hbar$ resulting in an average angular momentum of 111 $\hbar$. In this case the time for a full rotation is T = 0.97×10^{-20} s which is seven times shorter than the time obtained within the DNS model. As a consequence, also the resulting mean lifetimes are seven times shorter and have values of less than 5×10^{-21} s.

As mentioned above, it was assumed for these calculations that the moment of inertia I_{DNS} is given by two rigid spheres and does not change during the rotation. However, a more realistic approach is that I_{DNS} increases during the lifetime of the DNS

because the deformation of the nuclei increases which is reflected by the low measured TKE values. If the deduced quadrupole deformations of $\beta_2 = 0.4$ are considered, a value of $I_{DNS} = 12.3 \times 10^6$ MeVfm^2 can be obtained which is 1.9 times larger than the value for spherical nuclei leading to an increase of the DNS lifetimes by the same factor.

Chapter 5

Summary and Outlook

The present work was motivated by recent theoretical predictions of the possibilities to use multi-nucleon transfer reactions to produce neutron rich unknown isotopes in the heavy and superheavy region of the nuclear chart. New experimental data on multi-nucleon transfer reactions in such heavy collision systems are needed to improve our knowledge of the process in order to proceed with the application of this method. Additionally, multi-nucleon transfer reactions can be used as a tool to study the early stages of the fusion reaction. With this aim, the present thesis work investigated multi-nucleon transfer reactions in the collision systems ^{58,64}Ni + ^{207}Pb at relatively low beam energies around the Coulomb barriers, using the velocity filter SHIP. A region of known α-emitting isotopes was populated above the target nucleus (Z>82) with relatively high cross-sections. The present detection system of SHIP allows the identification of the reaction products via their decay characteristics, particularly via α-decays. The measurements of the velocity spectra is used as a means to identify the reaction channel (fusion, transfer reactions, etc). The total kinetic energy of the reaction products and the dissipated energy can also be obtained from the velocity spectra.

The influence of the different neutron numbers of the projectiles was studied in the isotopic distributions and excitation functions measured for both reactions. The main results are summarize in the following:

- In the reactions with both beams a transfer of up to 7 protons from the projectile to the target nucleus was observed. The most neutron rich transfer products (8 neutrons more than the target) were seen with ^{64}Ni beams.
- About ten times larger production cross-sections were measured for ^{58}Ni reactions

but the isotopic distributions were considerably shifted to the neutron rich side in reactions with ^{64}Ni.

- The measured total kinetic energies indicated that the transfer products were produced in deep inelastic collisions with full dissipation of energy in the entrance channel. The only exception are the isotopes Po and At produced in ^{58}Ni reactions. The measured total kinetic energies correspond to a re-separation of the nuclei according to the Coulomb barriers in the exit channels of a rather elongated di-nuclear system with quadrupole deformations for the projectile-like and target-like products of β_2=0.4.

- The reactions with ^{58}Ni beams proceed generally "colder" than for ^{64}Ni, which is reflected in the isotopic distributions as a function of the beam energy. The nuclear overlap in ^{58}Ni reactions is smaller than in the case of ^{64}Ni. A strong influence of shell effects, particularly of the closed neutron shell at N=126, on the excitation energy of the transfer products was seen at the lowest beam energies.

- Strong similarities in the excitation functions between transfer products and superheavy cold fusion evaporation residues were observed. This is consistent with the picture assumed by the two center shell model of fusion initiated by transfer reactions.

- A comparison of the measured cross-sections with calculations in the two-center shell model with adiabatic potentials in the case of ^{64}Ni reactions showed that the model underestimates the production cross-sections by at least one order of magnitude. The same model is used to predict the production cross-sections of heavier nuclei and a possible underestimation can also take place here. In this sense, the present experimental results can be used to improve the model predictions for superheavy nuclei.

- Nuclear interaction times where measured using the velocity spectra of the isotopes ^{213}Rn, ^{213}Fr and ^{215}Ra produced in ^{64}Ni reactions at 5.92×A MeV. The measured velocity spectra revealed a 180° rotation of the di-nuclear system and provide rather direct measurement of the nuclear interaction times. The deduced interaction times were on the order of 10^{-20} s for the system Ni + Pb. The interaction times increase with the number of transferred protons reflecting mainly the correlation between the lifetime of the di-nuclear system and the number of transferred nucleons.

Further experiments on multi-nucleon transfer reactions using heavier projectile and target combinations would contribute considerably to the present discussion concerning the production of new neutron rich isotopes in the heavy and superheavy region, for example using the reaction ^{48}Ca + ^{248}Cm. However, the nuclei in the region around Z=100 are mainly fissioning nuclei or β-emitters. The presently applied detection techniques do not allow the unambiguous identification of these nuclei. Other identification methods must be considered like high precision mass measurements using a Penning trap or a time of flight spectrometer.

Versicherung

Ich erkläre: Ich habe die vorgelegte Dissertation selbständig und ohne unerlaubte fremde Hilfe und nur mit den Hilfen angefertigt, die ich in der Dissertation angegeben habe. Alle Textstellen, die wörtlich oder sinngemäß aus veröffentlichten Schriften entnommen sind, und alle Angaben, die auf mündlichen Auskünften beruhen, sind als solche kenntlich gemacht. Bei den von mir durchgeführten und in der Dissertation erwähnten Untersuchungen habe ich die Grundsätze guter wissenschaftlicher Praxis, wie sie in der "Satzung der Justus-Liebig-Universität Gießen zur Sicherung guter wissenschaftlicher Praxis" niedergelegt sind, eingehalten.

Gießen, XV Juni, 2012

Victor Fernandovich Comas Lijachev

Bibliography

[1] V.M. Strutinsky. Nucl. Phys. A **95**, 420 (1967).

[2] R. Smolanczuk et al. Phys. Rev. C **52**, 1871 (1995).

[3] V. I. Zagrebaev, M. G. Itkis, Yu. Ts. Oganessian, and W. Greiner. Phys. Rev. C **73**, 031602 (2006).

[4] G. G. Adamian, N. V. Antonenko, and A. S. Zubov. Phys. Rev. C **71**, 034603 (2005).

[5] V. I. Zagrebaev and W. Greiner. Phys. Rev. Lett **101**, 122701 (2008).

[6] G. G. Adamian, N. V. Antonenko, and W. Scheid. Phys. Rev. C **68**, 034601 (2003).

[7] V. V. Volkov. Proc. Int. Conf on Reactions between complex nuclei, Nashville **2**, 363 (1974).

[8] F. Plasil. Proc. Int. Conf on Reactions between complex nuclei, Nashville. **2**, 107 (1974).

[9] L. G. Moretto and J. S. Sventek. Phys. Lett. **58B**, 26 (1976).

[10] F. Hanappe, M. Lefort, C. Ngô, J. Péter, and B. Tamain. Phys. Rev. Lett. **32**, 738 (1974).

[11] A. G. Artukh, G. F. Gridnev, V. L. Mikheev, V. V. Volkov, and J. Wilczýnski. Nucl. Phys. A **215**, 91 (1973).

[12] K. L. Wolf, J. P. Unik, J. R. Hiuzenga, J. R. Birkelund, H. Freiesleben, and V. E. Viola. Phys. Rev. Lett. **33**, 1105 (1974).

[13] L. G. Moretto, D. Heunemann, R. C. Jared, R. C. Gatti, and S. G. Thompson. Physics and chemistry of fission, Intern. Atomic Energy Agency, Vienna **2**, 351 (1973).

[14] R. Bock, B. Fischer, A. Gobbi, K. Hildenbrand, W. Kohl, U. Lynen, I. Rode, H. Stelzer, G. Auger, J. Galin, J. M. Lagrange, R. Albrecht, and B. B. Back. Ninth Masurian School in Nuclear Physics, Mikolaiki (1976).

[15] A. G. Seamster, R. E. L. Green, and R. G. Korteling. Nucl. Instr. and Meth. **145**, 583 (1977).

[16] M. M. Fowler and R. C. Jared. Nucl. Instr and Meth **124**, 341 (1975).

[17] G. K. Gelbke, K. D. Hildenbrand, and R. Bock. Nucl. Instr and Meth **95**, 397 (1971).

[18] T. M. Cormier, R. S. Galik, E. R. Cosman, and A. J. Lazzarini. Nucl. Instr and Meth **119**, 145 (1974).

[19] M. Evers, D. J. Hinde, M. Dasgupta, D. H. Luong, R. Rafiei, and R. du Rietz. Phys. Rev. C **81**, 014602 (2010).

[20] L. Corradi, A. M. Vinodkumar, A. M. Stefanini, E. Fioretto, G. Prete, S. Beghini, G. Montagnoli, F. Scarlassara, G. Pollarolo, F. Cerutti, and A. Winther. Phys. Rev. C **66**, 024606 (2002).

[21] W. Grochulski, T. Kwiecinska, Lan Go-chan, E. Lozýnski, J. Maly, L. K. Tarasov, and V. V. Volkov. Proc. Third Conf. on Reactions between complex nuclei, Asilomar, (1963).

[22] Yu. Ts. Oganesyan, Yu. E. Penionzkevich, So ki Khvan, A. O. Shamsutdinov, N. S Maltseva, and I. I. Chuburkova. Yad. Fiz. **11**, 492 (1970).

[23] J. V. Kratz, A. E. Norris, and G. T. Seaborg. Phys. Rev. Lett. **33**, 502 (1974).

[24] J. V. Kratz, J. O. Liljenzin, A. E. Norris, and G. T. Seaborg. Phys. Rev. C **13**, 2347 (1974).

[25] R. Bimbot, D. Gardes, R. L. Hahn, Y. De Moras, and M. F. Rivet. Nucl. Phys. A **188**, 85 (1974).

[26] M. Schädel et al. Phys. Rev. Lett **48**, 852 (1982).

[27] A. Türler et al. Phys. Rev. C **46**, 1364 (1992).

[28] J. Wilczýnski. Phys. Lett **47B**, 484 (1973).

[29] W. U. Shröder and J. R. Huizenga. Ann. Rev. Nucl. Sci **27**, 465 (1977).

[30] P. Bonche, S. E. Koonin, and J. W. Negele. Phys. Rev. C **13**, 1226 (1976).

[31] P. Bonche. J. Phys **37**, C5-213 (1976).

[32] R. Y. Cusson and J. Maruhn. Phys. Lett. B **62**, 134 (1976).

[33] R. Y. Cusson, R. K. Smith, and J. Maruhn. Phys. Rev. Lett **36**, 1166 (1976).

[34] W. Nörenberg. Z. Phys. A **274**, 241 (1975).

[35] W. Nörenberg. Z. Phys. A **276**, 84 (1976).

[36] W. Nörenberg. J. Phys **37**, C5-141 (1976).

[37] L. G. Moretto and R. Schmitt. J. Phys **37**, C5-109 (1976).

[38] J. S. Sventek and L. G. Moretto. Phys. Lett. B **65**, 326 (1976).

[39] J. Blocki el al. Ann. Phys **105**, 427 (1977).

[40] J. Blocki el al. Ann. Phys **113**, 330 (1978).

[41] J. Randrup. Ann. Phys **112**, 356 (1978).

[42] J. Randrup. Nucl. Phys. A **307**, 319 (1978).

[43] H. J. Fink et al. N. A **2**, 21 (1974).

[44] O. Zhoni et al. Z. Phys. A **275**, 235 (1975).

[45] s. Yamaji et al. Z. Phys. A **278**, 69 (1976).

[46] G. G. Adamian and N. V. Antonenko. Personal Communication.

[47] J. Maruhn and W. Greiner. Z. Phys **251**, 431 (1972).

[48] G. G. Adamian, N. V. Antonenko, A. Diaz. Torres, and W. Scheid. Nucl. Phys. A **671**, 233 (2000).

[49] G. G. Adamian, N. V. Antonenko, , W. Scheid, and V. V. Volkov. Nucl. Phys. A **627**, 361(1997).

[50] G. Münzenberg, S. Hofmann, F. P. Hessberger, W. Reisdorf, K. H Schmidt, J. H. R Schneider, P. Ambruster, C. C. Sahm, and B. Thuma. Nucl. Instrum. and Methods **161**, 65 (1979).

[51] A. V. Yeremin, D. D. Bogdanov, V. I. Chepigin, V. A. Gorshkov, A. P. Kabachenko, O. N. Malyshev, A. G. Popeko, R. N. Sagaidak, G. M. Terakopian, and A. Yu. Lavrentjev. Nucl. Inst. and Meth. B **126**, 329 (1997).

[52] Yu. A. Lazarev et al. Proceedings of the International School Seminar on Heavy Ions Physics, Dubna, Russia, II, 497 (1993).

[53] H. Miyatake, T. Nomura, H. Kawakami, J. Tanaka, M. Oyaizu, K. Morita, T. Shinozuka, H. Kudo, K. Sueki, and Y. Iwata. Nucl. Instrum. Methods Phys. Res. B **26**, 309 (1987).

[54] M. Leino et al. Z. Phys. A **348**, 151 (1994).

[55] A. Semchenkov et al. Nucl. Instr. and Meth. in Phys. Res. B **266**, 4153 (2008).

[56] B. Lommel et al. Nucl. Instr. Meth. A **480**, 16 (2002).

[57] R. Mann et al. GSI Scientific Report, 224 (2004).

[58] Š. Šaro et al. Nucl. Instr. and Meth. in Phys. Res. A **381**, 520 (1996).

[59] S. Heinz, V. Comas, F. P. Hessberger, S. Hofmann, D. Ackermann, H. G. Bukhard, Z. Gan, J. Heredia, J. Khuyagbaatar, B. Kindler, B. Lommel, R. Mann, J. Maurer, K. Nishio, and B. Sulignano. Eur. Phys. J. A **8**, 227 (2008).

[60] R. Bass. Nucl. Phys. A **231**, 45 (1974).

[61] M. Wilpert, B. Gebauer, Th. Wilpert, W. von Oersten, H. G. Bohlen, and J. Speer. Phys. Rev. C **51**, 680 (1995).

[62] W. von Oersten, H. G. Bohlen, B. Gebauer, R. Künkel, F. Pühlhofer, and D. Schüll. Z. Phys. A **326**, 463 (1987).

[63] A. H. Wapstra, G. Audi, and C. Thibault. Nucl. Phys. A **729**, 129 (2003).

[64] G. G. Adamian, R. V. Jolos, and A. K. Nasirov. Z. Phys. A **347**, 203 (1994).

[65] A. S. Iljinov, M. V. Mebel, N. Bianchi, E. De Sanctis, C. Guaraldo, V. Lucherini, V. Muccifora, E. Polli, A. R. Reolon, and P. Rossi. Nucl. Phys. A **543**, 517 (1992).

[66] S. Heinz, V. Comas, S. Hofmann, D. Ackermann, J. Heredia, F. P. Hessberger, J. Khuyagbaatar, B. Kindler, B. Lommel, and R. Mann. Eur. Phys. J. A **43**, 181 (2010).

[67] S. Hofmann and G. Münzenberg. Rev. Mod. Phys. **72**, 733 (2000).

[68] W. J. Swiatecki. Prog. Part. Nucl. Phys. **4**, 383 (1980).

[69] S. Bjornholm and W. J. Swiatecki. Nucl. Phys. A **391**, 471 (1982).

[70] V. V. Sargsyan, G. G. Adamian, N. V. Antonenko, and W. Scheid H. Q. Zhang. Phys. Rev. C **84**, 064614 (2011).

[71] A. J. Pacheco et al. Phys. Rev. C **45**, 2861 (1992).

[72] R. Bock et al. Nucl. Phys. A **388**, 334 (1982).

[73] E. Prokhorova et al. Nucl. Phys. A **802**, 45 (2008).

[74] H. Timmers et al. Nucl. Phys. A **633**, 421 (1998).

[75] R. A. Broglia, C. H. Dasso, S. Landowne, and A. Winther. Phys. Rev. C **27**, 2433 (1983).

[76] A. Astier, P. Petkov, M. G. Porquet, D. S. Delion, and P. Schuck. Phys. Rev. lett **104**, 042701 (2010).

[77] V. I. Zagrebaev and W. Greiner. J. Phys. G: Nucl. Part. Phys **34**, 1-25 (2007).

[78] H. Freiesleben, K. D. Hildenbrand, F. Pühlhofer, W. F. W. Schneider, and R. Bock. Z. Phys. A. **292**, 171 (1979).

[79] C. Golabek, S. Heinz, W. Mittig, F. Rejmund, A. C. C. Villari, S. Bhattacharyva, D. Boilley, G. De France, A. Drouart, L. Gaudefroy, L. Giot, V. Maslov, M. Morjean, G. Mukherjee, Yu. Penionzkevich, P. Roussel-Chomaz, and C. Stodel. Eu. Phys. J A **43**, 251 (2010).

[80] H. Savajols. Nucl. Inst. Meth. B **204**, 146 (2003).

[81] V. I. Zagrebaev. Personal Communication.

[82] G. Soff, J. Reinhard, B. Müller, and W. Greiner. Phys. Rev. Lett **43**, 1981 (1979).

[83] E. Kankeleit. 12th Sommer School in Nuclear Physics **25**, 252 (1980).

[84] H. Backe. New Trends in Atomic Physics, North Holland Publishing Corp.,(Amsterdam, Oxford, New York, Tokyo 697, (1984).

[85] J. Stroth, H. Backe, M. Begemann-Blaich, K. Bethge, H. Bokemeyer, M. Dahlinger, W. Konen, P. Kosmadakis, S. Mojumder, P. Senger, and K. Stiebing. Z. Phys. A **357**, 441 (1997).

[86] D. J. Hinde, D. Hilsher, and H. Rossner. Nucl. Phys. A **502**, 497c (1989).

[87] D. J. Hinde, D. Hilsher, H. Rossner, B. Gebauer, M. Lehmann, and W. Wilpert. Phys. Rev. C **45**, 1229 (1992).

[88] J. Töke et al. Nucl. Phys. A **440**, 327 (1985).

[89] W. Q. Shen et al. Phys. Rev. C **36**, 115 (1987).

[90] R. du Rietz, D. J. Hinde, M. Dasgupta, R. G. Thomas, L. R. Gasques, M. Evers, N. Lobanov, and A. Wakhle. Phys. Rev. Lett **106**, 052701 (2011).

[91] D. S. Gemmell. Rev. Mod. Phys. **46**, No1 (1974).

[92] J. U. Andersen, J. Chevallier, J. S. Forster, S. A. Karamian, C. Broude, F. Malaguti, and A. Ugozzini. Phys. Rev. Lett **99**, 162502 (2007).

[93] J. U. Andersen, J. Chevallier, J. S. Forster, S. A. Karamian, C. Broude, F. Malaguti, and A. Ugozzini. Phys. Rev. C **78**, 064609 (2008).

[94] J. F. Ziegler. Nucl. Instr. Meth. B **1027**, 219 (2004).

[95] H.A. Kramers. Physica **7**, 284 (1940).

[96] V.M. Strutinsky. Phys. Lett. B **47**, 121 (1973).

[97] P. Grangé, Li Jun-Qing, and H. A. Weidenmüller. Phys. Rev. C **27**, 2063 (1983).

[98] P. Grangé. Nucl. Phys. A **428**, 37c (1984).

[99] P. Fröbrich and G. R. Tillack. Nucl. Phys. A **540**, 353 (1992).

[100] V. I. Zagrebaev. Phys. Rev. C **64**, 034606 (2001).